Title

Hierarchically Structured Hydrogels with High Strength, Toughness and Fatigue Resistance

Permalink

https://escholarship.org/uc/item/51h8g0fd

Author

Hua, Mutian

Publication Date

2021

Peer reviewed|Thesis/dissertation

UNIVERSITY OF CALIFORNIA

Los Angeles

Hierarchically Structured Hydrogels with

High Strength, Toughness and Fatigue Resistance

A dissertation submitted in partial satisfaction of the

requirements for the degree Doctor of Philosophy

in Materials Science and Engineering

by

Mutian Hua

2021

ABSTRACT OF THE DISSERTATION

Hierarchically Structured Hydrogels with

High Strength, Toughness and Fatigue Resistance

By

Mutian Hua

Doctor of Philosophy in Materials Science and Engineering

University of California, Los Angeles, 2021

Professor Ximin He, Chair

A hydrogel can be viewed as a unique combination of liquid and solid, the liquid side properties

endow it with generally good biocompatibility and high porosity for fast diffusion, yet they are

shape fixable as a solid material, by applying knowledge of molecular and structural engineering,

they can also be made to bear moderate external loads. These unique combinations of physical and

chemical properties make them promising materials for various applications.

However, fragileness and low durability are major obstacles that hindered broad application of

hydrogels in practice. We developed a class of strong and tough hydrogels by tailoring hydrogel

structure across several hierarchical length-scales via modulation of polymer aggregation. The series of hydrogels were prepared by combining freeze-casting and salting out in sequential steps, which could realize simultaneously high strength, toughness, stretchability and fatigue resistance.

In Chapter 1, the fundamentals and fracture mechanics of hydrogel were discussion. The design principals for improving hydrogel mechanical properties include extending chain length, increasing chain fracture energy, promoting stress distribution and adopting anisotropic design.

In Chapter 2 and 3, the mechanism of preparing tough hydrogels via freeze-casting and salting out step was discussed and hydrogels with simultaneous high toughness, fatigue resistance was realized.

In Chapter 4 and 5, utilizing the developed tough hydrogel, the applications of hydrogel reinforcement coating and 3D printing were explored. These applications show that the developed tough hydrogels have significant versatility for various applications.

The dissertation of Mutian Hua is approved.

Yu Huang

Qibing Pei

Hsian-Rong Tseng

Ximin He, Committee Chair

University of California, Los Angeles

2021

Dedicated to my parents Yanan Xi, Tianmiao Hua,

and my wife Yuhan Long

For their unconditional love and support

TABLE OF CONTENTS

List of Figures

ACRYNYMS

PVA   Poly(vinyl alcohol)

DSC   Differential scanning calorimetry

DMA   Dynamic mechanical analysis

XRD   X-ray diffraction

SEM   Scanning Electron Microscopy

SAXS   Small Angle X-ray Diffraction

WAXS   Wide Angle X-ray Diffraction

AgNWs   Silver nanowires

PPy   Poly(pyrrole)

GCD   Galvanostatic Charge-Discharge

PNIPAM   Poly(N-isopropylacrylamide)

LCST   Lower critical solution temperature

DN   Double Network

ACKNOWLEDGEMENTS

As I come close to the end of my Ph.D study, I cannot help looking back at the five years' journey at UCLA. I came to UCLA as a young man with ambition, passion, and naiveness. Now I am leaving with more, as I have gained perseverance, devotion, wisdom and hope.

First and foremost, I should acknowledge my advisor Prof.Ximin He for her unwavering support and guidance during my entire Ph.D study, without which I couldn't have gained so much. I am also deeply grateful to Prof. Yu Huang, Qibing Pei and Hsian-Rong Tseng for severing as my committee members and providing their expertise and advice in my research.

Second, I would like to acknowledge my project collaborators, Prof. Zhigang Suo, Prof. Brigitte Gomperts, Prof. Xuanhe Zhao, Dr. Shaoting Lin for their supportive discussion and guidance, without which many projects would not have been possible.

Third, I would like to express my sincere gratitude to my lab mates, Dr. Shuwang Wu, Dr. Yanfei Ma, Dr. Xiaoshi Qian, Dr. Cheolgyu Kim, Dong Wu for their friendship and collaboration. I will certainly miss the days we worked together in the He lab.

Lastly, I must thank my parents Yanan Xi and Tianmiao Hua, for their unconditional love and support, from half-way across the world. Their care and encouragement gave me strength to finish this "marathon". My beloved wife, who had my back through all the hard times, showed me her vow of love, patience, and trust. Her understanding and companionship gave me reason to succeed in this journey. My family was the brightest torch in my dark times and lead me to dawn, I couldn't have done this without them.

VITA

2016   B.S., Materials Science and Engineering, Beijing Institute of Technology, Beijing, China

2016-2021   Ph.D Student, Materials Science and Engineering, University of California, Los

Angeles, CA,USA

PUBLICATIONS

[1] Strong tough hydrogels via the synergy of freeze-casting and salting out
M Hua†, S Wu†, Y Ma, Y Zhao, Z Chen, I Frenkel, J Strzalka, H Zhou, X Zhu, X He
Nature 2021, 590 (7847), 594-599

[2] Poly (vinyl alcohol) Hydrogels with Broad-Range Tunable Mechanical Properties via the Hofmeister Effect
S Wu†, **M Hua**†, Y Alsaid, Y Du, Y Ma, Y Zhao, CY Lo, C Wang, D Wu, B Yao, J Strzalka, H Zhou, X Zhu, X He
Advanced Materials 2021, 33 (11), 2007829

[3] Tough-Hydrogel Reinforced Low-Tortuosity Conductive Networks for Stretchable and High-Performance Supercapacitors
M Hua, S Wu, Y Jin, Y Zhao, B Yao, X He
Advanced Materials 2021, 2100983

[4] Swaying gel: chemo-mechanical self-oscillation based on dynamic buckling
M Hua†, C Kim†, Y Du, D Wu, R Bai, X He
Matter 2021, 4 (3), 1029-1041

[5] 4D Printable Tough and Thermoresponsive Hydrogels
M Hua†, D Wu†, S Wu, Y Ma, Y Alsaid, X He
ACS Applied Materials & Interfaces 2021, 13 (11), 12689-12697

[6] Self-Reporting Hydrogel Sensors Based on Surface Instability-Induced Optical Scattering
I Frenkel†, **M Hua**†, Y Alsaid, X He
Advanced Photonics Research 2021, 2100058

[7] Soft-fiber-reinforced tough and fatigue resistant hydrogels
M Hua, X He
Matter 2021, 4 (6), 1755-1757

[8] Bioinspired high-power-density strong contractile hydrogel by programmable elastic recoil
Y Ma†, **M Hua**†, S Wu, Y Du, X Pei, X Zhu, F Zhou, X He
Science Advances 2020, 6 (47), eabd2520

[9] Hydrocipher: Bioinspired Dynamic Structural Color-Based Cryptographic Surface
J Choi†, **M Hua**†, SY Lee, W Jo, CY Lo, SH Kim, HT Kim, X He
Advanced Optical Materials 2020,   8 (1), 1901259

[10] Surfactant-free fabrication of pNIPAAm microgels in microfluidic devices
M Hua, Y Du, J Song, M Sun, X He
Journal of Materials Research 2019, 34 (1), 206-213

" † " for co-first author

1. Introduction

1.1 Hydrogel Fundamentals

Hydrogels are a broad class of material composed of hydrophilic crosslinked networks (**Figure 1.1**)[1]. The constituent of hydrogels can range from monomers, oligomers to polymers and the crosslinks could be formed via physical (i.e., van der Waals, hydrogen bond, coordination bond, entanglement) or chemical bonds (i.e., covalent bond, Schiff base pairs). Due to the hydrophilic physical properties, these materials swell significantly in water and retain high percentage of water in their swollen state. In their swollen state, these materials exhibit a porous microstructure that allowed for mass diffusion through the material.
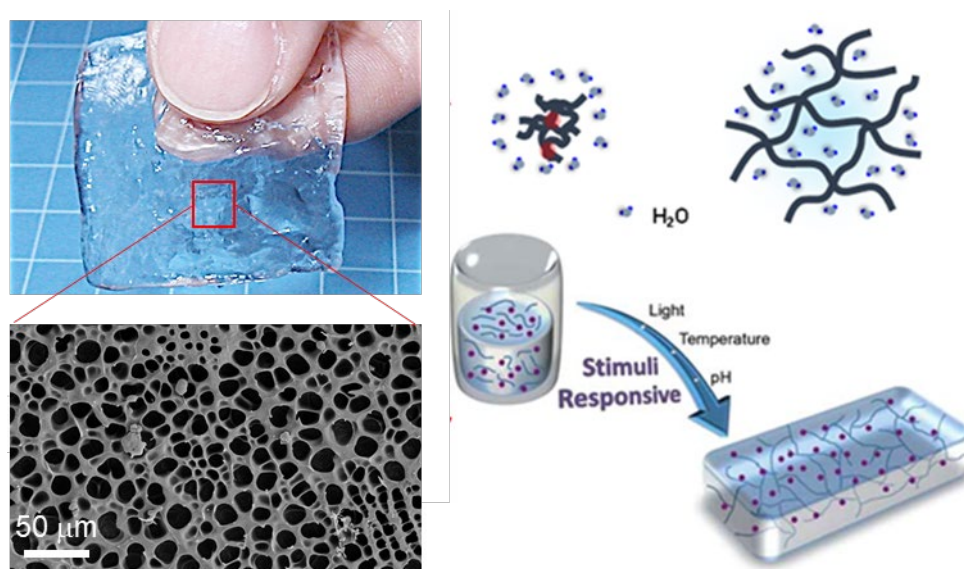
Figure 1.1 Top left shows a swollen piece of hydrogel, bottom left image shows the microstructure of the hydrogel after freeze drying in the swollen state. The right images show illustration of hydrogel volume change and shape change capabilities

Depending on the origin source, hydrogels can be classified into natural and synthetic kinds[2]. Synthetic hydrogels, due to their excellent programmability and improved stability, have surpassed natural hydrogels in many applications. Due to the broad definition of hydrogels, hydrogels can be synthesized via various approaches. Hydrogel synthesis methods include free-radical polymerization, physical crosslinking, and combined procedures involving both chemical crosslinking and physical crosslinking. As a result, hydrogels can be designed at molecular level for desired crosslink density, functionality and mechanical properties, such as biodegradability, high toughness, and response to physical or chemical stimuli[3].

Synthetic hydrogels have attracted considerable attention in the past decades due to their wide application in fields ranging from tissue engineering to soft robotics (**Figure 1.2**). This is attributed their versatility of synthesis, tunable microstructures, and controllable physical and chemical properties.
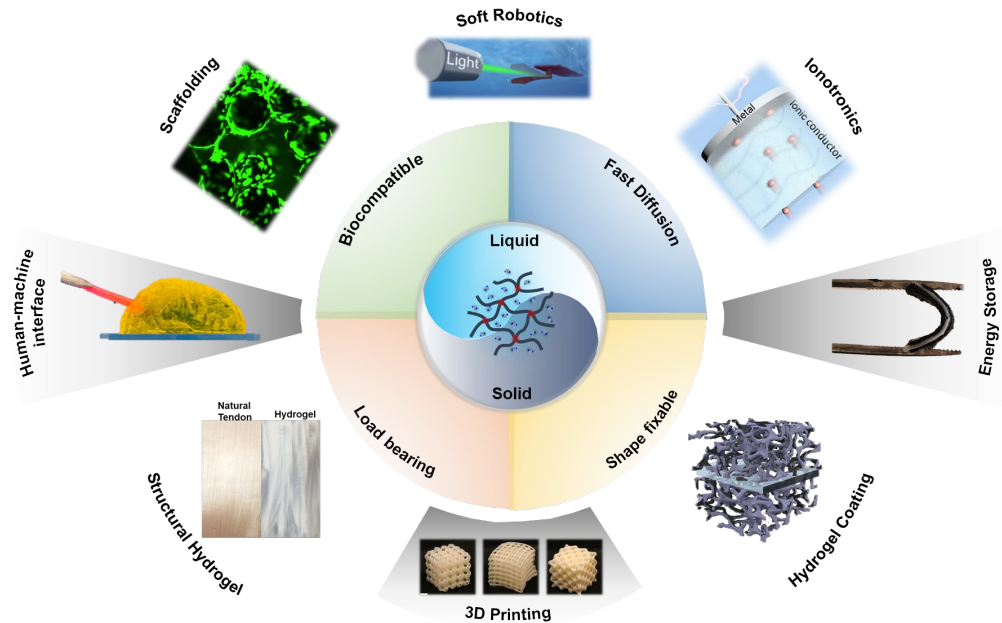
Figure 1.2 Application of hydrogels in various fields.

With different crosslinked functional groups, synthetic hydrogels can be divide into categories such as thermal responsive, pH responsive and humidity responsive hydrogels (**Figure 1.3**)[4]. By changing the functional groups, hydrogels can be tailored to respond to various stimuli. For instance, with hydroxyl side groups, hydrogels tend to respond to humidity; with carboxyl side groups, they tend to respond to pH; with methyl groups, they could be responsive to temperature; with other special side groups, they could be responsive to more complex stimuli such as glucose.
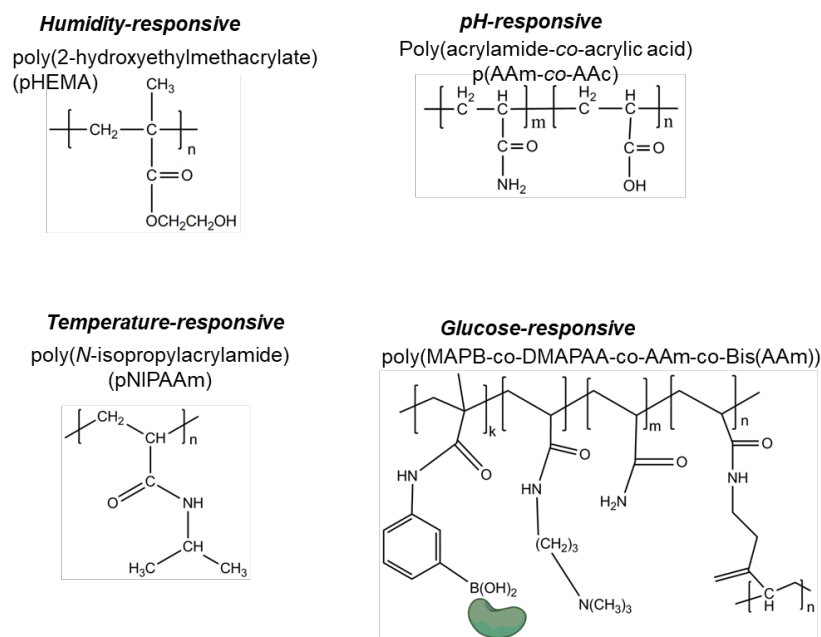
Figure 1.3 Different functional groups in hydrogel network

With different fabrication techniques, synthetic hydrogels can assume various microstructure such as aligned pore structures, open pore structures and close pore structures. For instance, by applying

directional ice templating, hydrogels can exhibit aligned pore structures[5]; by inducing phase separation via solvent exchange, hydrogels can also exhibit open pore structures where all pores are interconnected[6].

By combining different hydrogel composition and fabrication techniques, the hydrogels could attain various desired properties tailored for specific applications. For example, by constructing open / aligned porous microstructures and incorporating conductive polymers, fast diffusion and conductive properties could be achieved for energy storage and ionotronics applications; by inducing aligned microstructures and inducing crystallization of the hydrogels, high mechanical properties could be achieved for load bearing applications; by incorporating biocompatible and adhesive polymers in the hydrogel, superior biocompatibility could be achieved for cell seeding and tissue engineering applications.

1.2 Current Challenges of Hydrogel Applications

In the materials world, most raw materials possess inherent mechanical properties insufficient for direct use, and thus demand enhancement in strength for load bearing, in toughness for damage tolerance, and in fatigue resistance for prolonged service. However, strengthening and toughening treatments often face contradictions due to the deteriorated resilience / ductility of the material after most strengthening treatments[7]. This is not the case for many natural materials, where the combination of normally contradicting mechanical properties is often achieved by the formation of hierarchical microstructures. Wood is light and strong, nacres are hard and resilient, muscles

and tendons are soft and tough (**Figure 1.4**). Among them, tendons stand out with the highest combination of strength (100-150 MPa) and elongation till fracture (up to 42%), and with no deterioration even when used for over 1 million cycles per year[8]. Such excellent mechanical robustness is attributed to anisotropic structures that persist through multiple levels in tendons, ranging from macroscopic to nanoscopic scales[9]. Many wisdoms have been borrowed from these natural materials to enhance man-made materials by inducing anisotropic structures through methods such as electro-spinning[10], extrusion[11], rolling[12], twisting[13], templating[14,15], self-assembly[16], and mechanical stretching [17,18]. However, currently available techniques often fail to replicate the multiscale hierarchy (across mm to nm and even molecular level) and the complexity (*e.g.*, web-like, spiral plaits, or stacked platelets) of anisotropic structures like those observed in natural materials[19,20], or do so at a high cost by using natural components with inherent complex anisotropic structures[21,22]. With only crudely synthesized structures, many anisotropically strengthened materials suffer from low maximum strain and premature failure due to insufficient active toughening mechanisms[7,19,23]. Therefore, the grand challenge of circumventing the conflict between toughening and strengthening of synthetic materials persists.
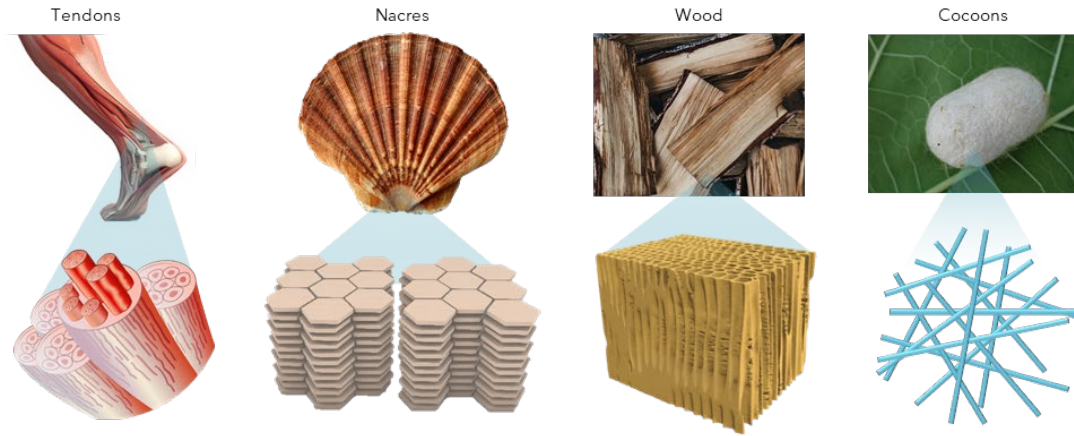
Figure 1.4. Natural materials with anisotropic / fibrous structures. From left to right: tendons exhibit aligned fibrous microstructures; nacres exhibit layered brick-and-mortar microstructure; wood exhibit aligned porous microstructure; cocoons exhibit random fibrous microstructure. The leg illustration was reproduced and adapted from illustration by Scientific Animations under CC BY-SA license.

Achieving "strengthening while toughening" presents an even greater challenge in hydrogels. Conventional hydrogels, are mechanically weak due to their low solid contents (70-98% water contents) and lack of energy dissipating mechanisms.[20,24–27] Their intrinsic softness and fragileness lead to low deliverable force[28,29] and large passive deformation upon contact when applied as actuators, which hinders their use in practical applications that involves high loads, abrupt impacts, and long-term services. Tremendous improvements have been made to strengthen or toughen hydrogels by introducing mechanisms for mechanical energy dissipation in hydrogels during loading, such as by forming double network[25,30–32], having dual crosslinking[24,33], adding

nano-fillers[34], inducing hydrophobic aggregation[35], and creating nano-crystalline domains[36,37].

However, these methods are still limited to structural changes within a narrow length scale (molecular or nanoscale) and simple structures. Recently, strong linking between anisotropically aligned individual micro/nano- reinforcement fillers to form a network has shown to be effective for both dissipating energy and maintaining elasticity[38,39], but is still lacking or insufficient in current tough gels. Forming a continuous single-material network out of strong building blocks would be an ideal approach, but challenging to realize, due to the lack of ability to control the aggregation of molecules directly into a hierarchical bulk material. Without this multiscale structure engineering, hydrogels of simultaneous high strength (>10 MPa) and large strain (>1000%) to produce giant toughness remain rather difficult to achieve.

1.3 Fracture Mechanics of Polymer Networks

To improve the mechanical properties of hydrogels and resolve the stiffness and toughness conflict in hydrogels, it is therefore important to understand the failure mechanism of hydrogels under external loading.

The failure of hydrogel originates from the fracture of polymer chains in the hydrogel network. The individual polymer strand between crosslink sites breaks when the tension in the strand exceeds a certain threshold which is dominantly determined by the bond strength in the polymer chain (usually C-C bond). From an energy perspective, work is applied to the hydrogel material

during loading and the polymer strands under tension elastically stores energy under the external loading. The individual polymer strand stays intact until a threshold energy is reached and dissipates the stored energy upon fracture of the strand. Each bond in the polymer strand stores the same amount of energy as the polymer stand is stretched, therefore, the threshold energy required to fracture a polymer strand scales with the chain length. This is generally known as the Lake Thomas Theory, which describes that the fracture energy of polymer chain is proportional to the square root of chain length. With the understanding of the chain fracture mechanism, it is therefore clear that a shorter chain between crosslinks fractures more easily than a longer chain in hydrogels.
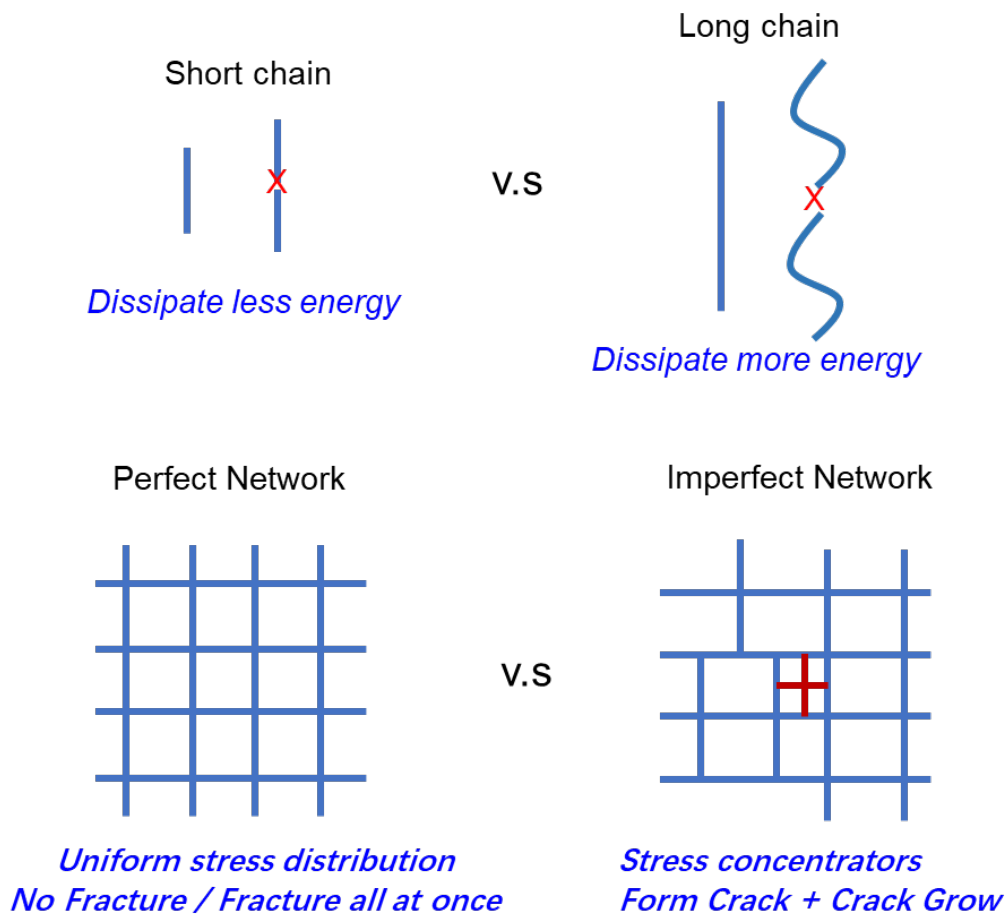
Figure 1.5 Chain fracture mechanism and network fracture mechanism.

While the failure of hydrogel originates from the fracture of polymer chains in the hydrogel network, the chain failure propagates through the network to lead to macroscopic fracture of the material. Therefore, apart from the chain length between crosslinks, the network structure plays also plays an important role is hydrogel failure. Ideally, having a uniform network lead to a uniform distribution of stress throughout the network. As a result, the polymer chains within the network synchronously stretch and breaks all at once upon reach the fracture threshold, which give rise to relatively higher strength and toughness of the hydrogel. Contrarily, a non-uniform network, which is the case for most regular hydrogels, stress is non-uniformly distributed and the shorter chains will fracture prior to their long chain counterparts. With the asynchronous fracture of polymer chains, the formed defect will serve as crack and subsequently propagate across the material.

In addition to the uniformity of the network structure, the density and anisotropy of the network structure could also play important role to change the hydrogel mechanical properties. For instance, the energy requires to fracture a polymer strand could be effectively raised by bundling multiple chains together into a single strand, as the tight molecular level bundling forbids the sequential fracture of individual polymer chains and promotes the simultaneous fracture of multiple polymer chains in the same bundle. Aligning the network in a certain direction could also effectively increase the resistance of crack propagation perpendicular to the align direction, as more polymer chains/strand lie in the way of the crack propagation direction.

With the understanding of the fracture mechanics of hydrogels, it could be concluded that extending the chain length between crosslinks in the hydrogel network, promoting uniform distribution of stress within the network, controlling the anisotropy of the network and changing the density of the network are critical design principals for improving the hydrogel's mechanical properties.

1.4 Motivation and Scope of Research

This dissertation will focus on applying molecular and structural design principals learnt form natural and practice in combination with suitable fabrication methods to address the central challenge of resolving the stiffness-toughness conflict in hydrogel materials and create hydrogels with simultaneously high ultimate strength and strain, toughness, and fatigue resistance.

The first part of the dissertation will focus on the design and development of tough hydrogels via hierarchical structural engineering. The effect of anisotropy, different length scale of structures, and effect of polymer aggregation state were investigated. An effective method combining freeze casting and salting out was developed. As a result, the toughness of hydrogel was improved for 4-10 times compared to previously reported tough hydrogels along with improved strength, elongation and fatigue threshold.

The second part of the dissertation will focus on the application of tough hydrogels with hierarchical structures prepared by adapted freezing assisted salting out method. The demonstrated applications include reinforcement coatings and 3D printing.

Based on the work completed during my Ph.D study, this dissertation is divided into six chapters: Chapter 1, the current chapter, provides a brief introduction of the fundamental of hydrogel, the current challenges, basic understanding of the material failure mechanisms.

Chapter 2 presented the method of fabricating strong and tough hydrogels by controlling the polymer aggregation via a freezing assisted salting out process. The underlying mechanism for polymer aggregation state tuning was discussed. The effect of salting type and concentration on the mechanical properties of PVA hydrogel were discussed.

Chapter 3 presented the development of a record breaking tough and fatigue resistant hydrogel by combining the developed freezing assisted salting out treatment process and structural engineering designs that introduced anisotropic structures in the hydrogel. The produced PVA hydrogel by directional freezing assisted salting out showed simultaneous high strength, elongation, toughness, and fatigue resistance. Such method could be expanded to various polymer systems. The structural-properties relationship was also discussed.

Chapter 4 demonstrated the application of tough PVA hydrogels prepared by a modified freezing assisted salting out process for hydrogel reinforcement coatings. With the thin coating of tough PVA hydrogel on a originally fragile open porous conductive electrode material, the electrode showed significantly improved mechanical property and electrochemical stability. Which can be applied for constructing thick supercapacitor with high energy density and high robustness.

Chapter 5 demonstrated the adaptation of the developed tough PVA hydrogels to a stereolithography 3D printing platform. A simple chemical modification to the PVA was carried out and enabled it photo-crosslinking capability. Utilizing the 3D printing technique, hydrogel actuators with complex designs were fabricated. Owing to the improved mechanical properties, the hydrogel actuators showed improved toughness and actuation power.

Chapter 6 summarizes the dissertation and provides an outlook for the future research and application of the tough hydrogels with hierarchical structures.

1.6 References

[1]   T. Tanaka, *Sci. Am.* **1981**, *244*, 117.

[2]   F. Ullah, M. B. H. Othman, F. Javed, Z. Ahmad, H. M. Akil, *Mater. Sci. Eng. C* **2015**, *57*, 414.

[3]   K. Y. Lee, D. J. Mooney, *Chem. Rev.* **2001**, *101*, 1869.

[4]   M. A. C. Stuart, W. T. S. Huck, J. Genzer, M. Müller, C. Ober, M. Stamm, G. B. Sukhorukov, I. Szleifer, V. V Tsukruk, M. Urban, F. Winnik, S. Zauscher, I. Luzinov, S. Minko, *Nat. Mater.* **2010**, *9*, 101.

[5]   H. Zhang, *Ice Templating and Freeze-Drying for Porous Materials and Their Applications*; Wiley-VCH Verlag GmbH & Co. KGaA: Weinheim, Germany, 2018.

[6]   Y. Alsaid, S. Wu, D. Wu, Y. Du, L. Shi, R. Khodambashi, R. Rico, M. Hua, Y. Yan, Y. Zhao, D. Aukes, X. He, *Adv. Mater.* **2021**, *33*, 2008235.

[7]   R. O. Ritchie, *Nat. Mater.* **2011**, *10*, 817.

[8]   M. Javidi, C. P. McGowan, N. R. Schiele, D. C. Lin, *Sci. Rep.* **2019**, *9*, 1.

[9]   F. H. Silver, J. W. Freeman, G. P. Seehra, *J. Biomech.* **2003**, *36*, 1529.

[10]   L. Gu, Y. Jiang, J. Hu, *Adv. Mater.* **2019**, *31*, 1904311.

[11]   S. Hong, D. Sycks, H. F. a. Chan, S. Lin, G. P. Lopez, F. Guilak, K. W. Leong, X. Zhao, *Adv. Mater.* **2015**, *27*, 4034.

[12]   B. B. He, B. Hu, H. W. Yen, G. J. Cheng, Z. K. Wang, H. W. Luo, M. X. Huang, *Science (80-.).* **2017**, *357*, 1029.

[13]   J. Mu, M. J. De Andrade, S. Fang, X. Wang, E. Gao, N. Li, S. H. Kim, H. Wang, C. Hou, Q. Zhang, M. Zhu, D. Qian, H. Lu, D. Kongahage, S. Talebian, J. Foroughi, G. Spinks, H. Kim, T. H. Ware, H. J. Sim, D. Y. Lee, Y. Jang, S. J. Kim, R. H. Baughman, *Science (80-.).* **2019**, *365*, 150.

[14]   K. Voges, C. Hübner, M. Vadalá, D. C. Lupascu, *Macromol. Mater. Eng.* **2018**, *303*, 1.

[15] L. Wen, R. Xu, Y. Mi, Y. Lei, *Nat. Nanotechnol.* **2017**, *12*, 244.

[16] H. Qin, T. Zhang, N. Li, H. P. Cong, S. H. Yu, *Nat. Commun.* **2019**, *10*, 1.

[17] M. T. I. Mredha, H. H. Le, V. T. Tran, P. Trtik, J. Cui, I. Jeon, *Mater. Horizons* **2019**, *6*, 1504.

[18] M. T. I. Mredha, Y. Z. Guo, T. Nonoyama, T. Nakajima, T. Kurokawa, J. P. Gong, *Adv. Mater.* **2018**, *30*, 1.

[19] H. Fan, J. P. Gong, *Macromolecules* **2020**, acs. macromol.0c00238.

[20] X. Zhao, *Soft Matter* **2014**, *10*, 672.

[21] A. Lazaris, S. Arcidiacono, Y. Huang, J. F. Zhou, F. Duguay, N. Chretien, E. A. Welsh, J. W. Soares, C. N. Karatzas, *Science (80-.).* **2002**, *295*, 472.

[22] F. Teulé, Y. G. Miao, B. H. Sohn, Y. S. Kim, J. J. Hull, M. J. Fraser, R. V. Lewis, D. L. Jarvis, *Proc. Natl. Acad. Sci. U. S. A.* **2012**, *109*, 923.

[23] U. G. K. Wegst, H. Bai, E. Saiz, A. P. Tomsia, R. O. Ritchie, *Nat. Mater.* **2015**, *14*, 23.

[24] X. Hu, M. Vatankhah-Varnoosfaderani, J. Zhou, Q. Li, S. S. Sheiko, *Adv. Mater.* **2015**, *27*, 6899.

[25] J.-Y. Sun, X. Zhao, W. R. K. Illeperuma, O. Chaudhuri, K. H. Oh, D. J. Mooney, J. J. Vlassak, Z. Suo, *Nature* **2012**, *489*, 133.

[26] M. Shibayama, *Soft Matter* **2012**, *8*, 8030.

[27] M. A. Haq, Y. Su, D. Wang, *Mater. Sci. Eng. C* **2017**, *70*, 842.

[28] W. R. K. Illeperuma, J. Y. Sun, Z. Suo, J. J. Vlassak, *Soft Matter* **2013**, *9*, 8504.

[29] K. Depa, A. Strachota, M. Šlouf, J. Hromádková, *Eur. Polym. J.* **2012**, *48*, 1997.

[30] G. Qu, Y. Li, Y. Yu, Y. Huang, W. Zhang, H. Zhang, Z. Liu, T. Kong, *Angew. Chemie - Int. Ed.* **2019**, *58*, 10951.

[31] J. P. Gong, Y. Katsuyama, T. Kurokawa, Y. Osada, *Adv. Mater.* **2003**, *15*, 1155.

[32] Q. Chen, L. Zhu, H. Chen, H. Yan, L. Huang, J. Yang, J. Zheng, *Adv. Funct. Mater.* **2015**, *25*, 1598.

[33] P. Lin, S. Ma, X. Wang, F. Zhou, *Adv. Mater.* **2015**, *27*, 2054.

[34] L. Han, X. Lu, K. Liu, K. Wang, L. Fang, L. T. Weng, H. Zhang, Y. Tang, F. Ren, C. Zhao, G. Sun, R. Liang, Z. Li, *ACS Nano* **2017**, *11*, 2561.

[35] Q. He, Y. Huang, S. Wang, *Adv. Funct. Mater.* **2018**, *28*, 1.

[36] S. Lin, J. Liu, X. Liu, X. Zhao, *Proc. Natl. Acad. Sci. U. S. A.* **2019**, *116*, 10244.

[37] S. Lin, X. Liu, J. Liu, H. Yuk, H.-C. Loh, G. A. Parada, C. Settens, J. Song, A. Masic, G. H. McKinley, X. Zhao, *Sci. Adv.* **2019**, *5*, eaau8528.

[38] C. Zhao, P. Zhang, J. Zhou, S. Qi, Y. Yamauchi, R. Shi, R. Fang, Y. Ishida, S. Wang, A. P. Tomsia, L. Jiang, M. Liu, *Nature* **2020**, *580*, 210.

[39] X. Liao, M. Dulle, J. M. De Souza E Silva, R. B. Wehrspohn, S. Agarwal, S. Förster, H. Hou, P. Smith, A. Greiner, *Science (80-.).* **2019**, *366*, 1376.

2. Hydrogel Structural and Mechanics Tuning via Hofmeister Effect

2.1 Introduction

Hydrogels have been widely studied because of their potential applications in various fields such as tissue engineering[1], drug delivery[2], implantable electronics[3], energy storage devices[4], coatings[5], adhesives[6], soft robotics[7], *etc*. However, mechanical and structural tunability issues persist and await solutions to bridge the gap between hydrogel research and practical applications. First for the mechanical performance of current hydrogels. The high water-content and loose crosslinking of hydrogels make them mechanically weak and often too fragile to handle practical tasks. Despite various advances in toughening hydrogels by forming double network[8], adding nano-fillers[9], and mechanical training[10], their mechanical performances are still less than satisfactory compared to waterless polymers[11,12]. Second for the tunability of hydrogel mechanics. Their resemblance to biological tissues make them the most ideal materials for tissue engineering[13]. In cell culturing, the elastic modulus of hydrogel should be on the same order of magnitude as that of the cells to promote adhesion between cells and hydrogel[14], and to better mimic physiological conditions. In stem cell studies, the modulus of hydrogels can also affect the differentiation[15], proliferation[16], mitigation[17] and spreading[18] of stem cells. Therefore, tremendous effort has been spent on tuning the hydrogel modulus via testing the combinations of various composition[19], concentration[20] or curing conditions[21]. However, these approaches suffer from a narrow range of achievable modulus[22] or require sophisticated recipes[19]. Third for the reversibility of hydrogel mechanics. In some scenarios, dynamic or in-situ tuning of the

material between stiff and soft states is highly beneficial[23,24]. For instance, a neuron probe is desired to be initially rigid for easy insertion into brain tissue, but become soft subsequently to avoid causing damage or inflammation to adjacent neuron cells[23,24]. Some elastomers based on phase transition can exhibit a large range of tunable modulus, yet they are still not soft enough to match the modulus of neurons even at their softest states[23]. Compared to elastomers, hydrogels are more biocompatible. Additionally, water, ions, nutrition, and many other biologically relevant molecules can transport freely in the porous hydrogel matrix[25]. Despite these significant advantages, little research has focused on realizing dynamic in-situ tuning of hydrogel mechanical properties, therefore limiting their applications in these important areas.

2.2 Proposed Method

Different salts exhibit distinguishable abilities to precipitate proteins from aqueous solutions, which is known as the Hofmeister effect or ion-specific effect[26]. The Hoffmeister series originated from the empirical and qualitative ranking of different ions' ability to precipitate proteins from solution, also known as the "Ion-specific effect" [27]. Such ion-specific phenomena have also been observed in other fields such as ice nucleation and recrystallization[28], colloidal assembly[29], and surface tension[30].Apart from proteins, many polymers also show similar trend of solubility in the presence of ions. For instance, PVA could strongly precipitate to form gels in the presence of some ions but dissolves quite well in other ionic solutions.

Regarding the synthetic macromolecules, plenty of researchers have studied the interactions among the ions, water molecules and polymer chains at the molecular level[31]; some works discussed how different ions affect the solubility and swelling of polymers[32]; a few papers reported improving hydrogel mechanical performance by soaking in salt solutions after the hydrogel is synthesized[33,34]. The previous studies of the ion-specific effect on hydrophilic polymers revealed that the ion-specific effects arise from the impacts of different ions on the hydration water around the hydrophilic functional groups on the hydrophobic chains[35]. However, the effects of different ions on the mechanical properties of hydrogels and utilizing the ion-specific effect to fabricate a functional hydrogel with variable mechanical properties have not yet been systematically studied[33,34,36–38].

We proposed a freeze-soak method, soaking the frozen polymer solutions in the salt solutions (**Figure 2.1**), to fabricate hydrogels with different mechanical properties by tuning the aggregation of the hydrophilic polymer chains at the molecular level via Hofmeister effect, to address the urgent demands of aforementioned various areas. Poly(vinyl alcohol) (PVA) was used as a model system here, because of the simple molecular structure of the amphiphilic macromolecule composed of a hydrophobic (CH_2-CH_2) backbone and hydrophilic (-OH) side-groups. Besides, it has many other outstanding merits such as biodegradability, biocompatibility, and nontoxicity[13] which have been well studied and made as hydrogels with various methods such as freeze-thaw, chemically crosslinking and mechanical training[10,13]. These make PVA an ideal exemplary

polymer for the systematic study of the effects of various anions and cations on hydrogel networks, and to develop hydrogels with widely tunable mechanical, structural and physical properties.

Figure 2.1 The schematic and the optical images of the freezing-soaking process.

2.3 Experimental Section

2.3.1 Materials:

Polyvinyl alcohol (PVA) (weight-average molecular weight (Mw) of 89~98 kDa; degree of hydrolysis of 99%; Sigma-Aldrich), glutaraldehyde (25 v %; Sigma-Aldrich), hydrochloric acid (36.5 to 38 wt %, Sigma-Aldrich), salts (analytical grade; Sigma-Aldrich) Rhodamine B, acrylamide (analytical grade; Sigma-Aldrich), N,N'-Methylenebisacrylamide and 2-Hydroxy-2-methylpropiophenone were used as received.

2.3.2 Preparation of PVA and salt solutions:

2, 5, and 10 wt% PVA solutions were prepared by dissolving PVA powder in deionized (DI) water under vigorous stirring and heating (95 °C). After degassing by sonication for 1 h, clear solutions were obtained. Various salt solutions of different concentrations were prepared by dissolving salts in DI water. After sonication for 10 mins, clear salt solutions were obtained.

2.3.3 Fabrication of hydrogel:

To judge if the PVA solutions can form hydrogels, 1.5 mL PVA solution of 5 wt% was injected into a vial and was frozen at -20 °C. Then the frozen samples were transferred to room temperature and different salt solutions of 1.0 M or DI water were added, where the ice melted over time. After 1 h, the vial was shaken to see if the solution became a hydrogel. To fabricate the hydrogels for measuring the mechanics, 20 mL 10 wt% PVA solution was poured into a Petri dish and freeze-thawed for 3 cycles, after which it became a hydrogel. The hydrogel was cut into strips of 5 mm × 3 cm and soaked into different salt solutions with specific concentrations for 24 h. At last, the hydrogels were washed with plenty of DI water to remove the salts.

2.3.4 Tensile testing:

Hydrogels were cut into dog-bone shaped specimens with gauge width of 2 mm for regular tensile testing. The thickness of each specimens was measured with a caliper. The force-displacement data were obtained using a Cellscale Univert mechanical tester with a 50N loading cell installed. The stress- strain curves were obtained by division of an initial gauge cross-section area and an initial

clamp distance.

2.3.5 SEM characterization:

For the characterization of the micro- and nano-structures of the hierarchically aligned hydrogels, all hydrogel samples were immersed in DI water for 24 hours before freeze drying using a Labconco FreeZone freeze drier. The freeze-dried hydrogels were cut along the aligned direction to expose the inside and sputtered with gold before carrying out the imaging using a ZEISS Supra 40VP SEM.

2.3.6 X-ray scattering characterization:

The hydrogels treated with different ions were cut into 1 cm by 4 cm rectangles and washed with plenty of DI water for before testing. The beamline station used was APS 8-ID-E (Argonne National Laboratory) equipped with Pilatus 1 M detector. A customized linear stretcher was used to hold the samples and stretch on demand for *in-situ* X-ray scattering measurements. A MATLAB toolbox "GIXSGUI" was used for further line-cut analysis and space conversion of the obtained scattering pattern[39].

2.3.7 Water content measurement:

The water contents of the PVA hydrogels were measured by comparing the weights before and after freeze-drying. Excess surface water was wiped away from the hydrogel surface before

measuring the weight (m_w). The hydrogel samples were instantly frozen in liquid nitrogen and freeze-dried with a Labconco FreeZone freeze drier. Weight before (m_w) and after freeze drying (m_d) were measured with a balance. The water content was calculated by *(m_w - m_d)/m_w*100%.*

2.3.8 Measurement of crystallinity:

The crystallinities of PVA-SO4 and PVA-NO3 were measured by DSC (DSC-Q8000). The PVA-SO4 and PVA-NO3 were first soaked in the 100 ml solution consisting 20 ml of glutaraldehyde and 1 ml of hydrochloric acid for 6 hours. During this process, the amorphous part in the hydrogels were crosslinked and fixed by glutaraldehyde. Thereafter, the samples were immersed in DI water for 24 hours to remove the unreacted glutaraldehyde and hydrochloric acid. The samples were further dried and measured with DSC[48].

2.3.9 Dynamically tune PVA hydrogel:

The PVA hydrogel freeze-thawed for three cycles was first immersed in a 1 M Na_2SO_4 solution for 24 h; then it was washed with plenty of water to remove the salts in the hydrogel. Afterwards, the hydrogel was soaked in a 3 M $CaCl_2$ solution for 48 h. During this soaking process, the images were taken with a camera.

2.3.10 Printing of brain-tissue-mimicking hydrogel:

Firstly, 100 mL precursor solution was prepared containing 5g monomer acrylamide, 400 mg

cross-linker   N,N'-methylenebisacrylamide,   and   10   µL   initiator   2-hydroxy-2-methylpropiophenone. Then the precursor was cured in a cubic mold with UV illumination or printed.

2.4 Results and Discussion

2.4.1 Gelation Diagram of PVA via Hofmeister Effect

We first evaluated the effects of various ions on the gelation of PVA in their respective sodium and chloride salt solutions with the freeze-soak assay. The 5 wt% PVA solution was first frozen at -20 °C, followed by the addition of 1.0 M salt solutions or pure water, after which the ice was allowed to melt at room temperature. With freezing, the PVA was fixed in a specific shape macroscopically (**Figure 2.2**) and the polymer chains were pre-packed microscopically to facilitate the subsequent aggregation by ions to form a bulk hydrogel. The freezing also ensured clear judgement of whether the gelation happened during the thawing process. As shown in Figure 2.3, instead of forming a dense bulk hydrogel, the aggregates of PVA (without prior freezing) dispersed in the solution, presented a cloudy dispersion, when the solution state PVA was directly added into a salt solution (1.0 M Na_2SO_4). On the contrary, with freezing, a dense bulk hydrogel was formed (Figure S2). This was attributed to the polymer chain pre-packing, as they were squeezed between the growing ice crystals during the freezing process[40]. During the subsequent melting process, the gelation occurred in 1.0 M Na_2SO_4 solution, which resulted in an opaque PVA hydrogel as shown in Figure S4; however, the PVA remained as a liquid solution when pure water or 1.0 M NaI solution was

23

used (**Figure 2.4**).

Figure 2.2 PVA hydrogels with different shapes obtained with freeze-soak method. Scale bar = 1

cm.
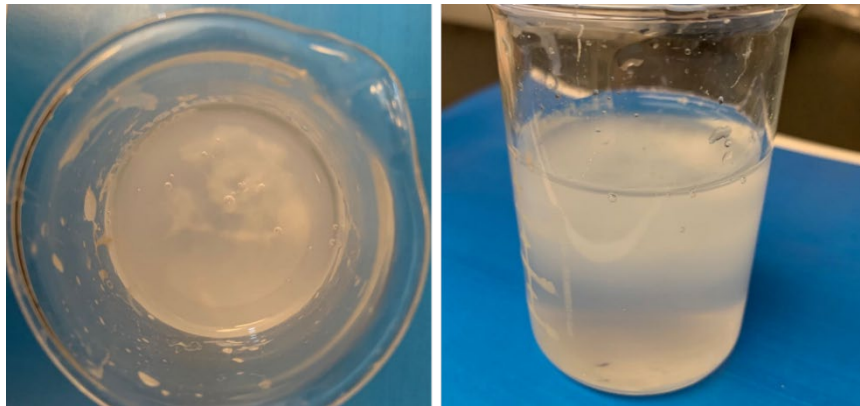
Figure 2.3 Optical images of the PVA in 1 M Na_2SO_4 without pre-freezing.
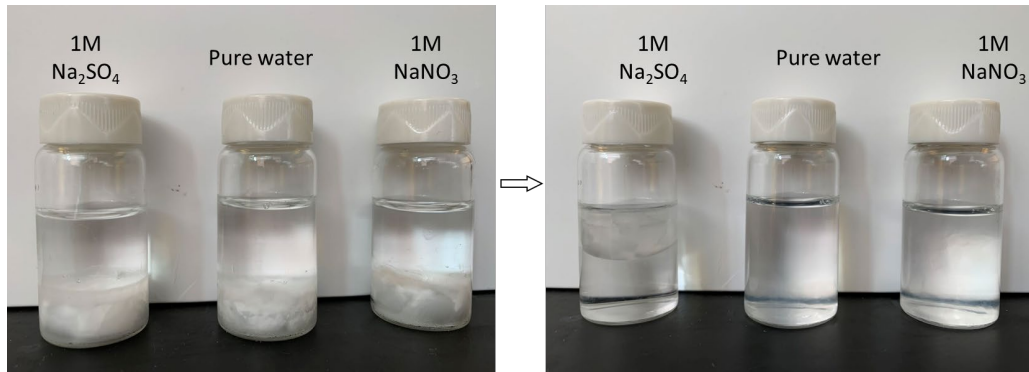
Figure 2.4 The optical images of the pre-frozen PVA soaking in different salt solutions or water, which eventually did (in 1 M Na$_2$SO$_4$) or did not (in pure water and 1 M NaNO$_3$) form hydrogels over time.

Generally, depending on the ion species, there are three kinds of possible interactions between the ions, the polymer chains, and the hydration water of polymer[35,41], as illustrated by **Figure 2.5**a. First, some anions can polarize the hydration water molecules, which destabilizes the hydrogen bonds between the polymer and its hydration water molecules (**Figure 2.5**a$_1$). Second, some ions can interfere with the hydrophobic hydration of the macromolecules by increasing the surface tension of the cavity surrounding the backbone (**Figure 2.5**a$_2$). Third, other anions can bind directly and thus add extra charges to the PVA chains, which increases the solubility of the polymer (**Figure 2.5**a$_3$). Specifically, ions such as SO$_4^{2-}$ and CO$_3^{2-}$ exhibit the first and second effects and could lead to the salting-out of polymers, thereby resulting in the collapse of polymer chains and forming small pores[41]. During the melting process of frozen samples in solutions of these ions, the water molecules were expelled from between the polymer chains, and the hydrogen bonds formed between the hydroxyl groups, which resulted in aggregation/crystallization of the polymer chains

25

(**Figure 2.5**b). By contrast, other ions like NO_3^- and I^- exhibit the third interaction and lead to the

salting-in of polymers[41]. As a result, the hydrogen bonds were dissociated, and the solubility

increased when the frozen samples were melted in solutions of these other ions (**Figure 2.5**c).
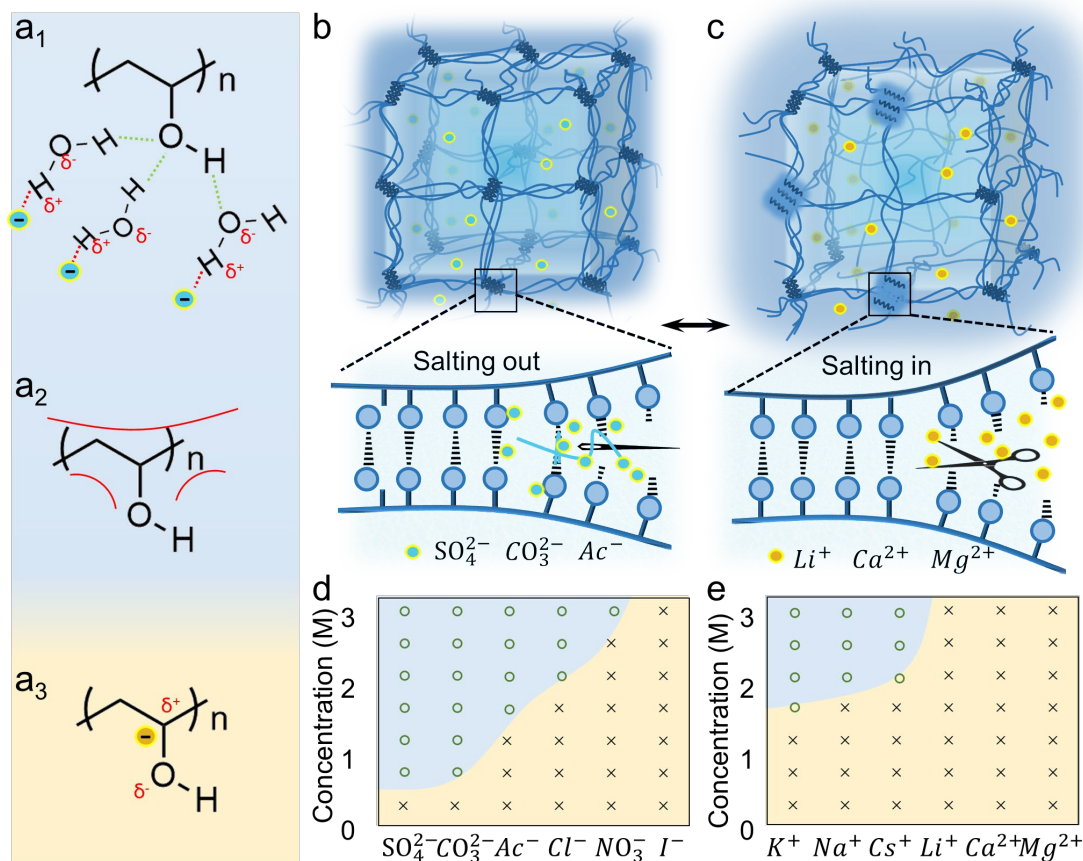
Figure 2.5 Schematics of the aggregation states of PVA polymer chains treated with different ions.

(a) The interactions among ions, polymer chains, and water molecules. (b) Hydrogen bonds form

between PVA polymer chains induced by ions due to salting-out effect. (c) Hydrogen bonds break

between PVA polymer chains induced by ions due to salting-in effect. (d, e) Summary of the status

of PVA gelation induced by different ions of different concentrations. The top-left region (blue)

and the bottom-right region (yellow), respectively, represent the gelation and non-gelation

conditions.

To systematically investigate the effect of each type of anions/cations, series of sodium salts and chloride salts were chosen according to the Hofmeister series. As depicted in **Figure 2.5**d, when frozen samples were soaked in Na_2SO_4 solution, PVA gelation occurred, as long as the ion concentration was higher than 0.5 M. However, in NaI solution, the PVA reverted to solution, even when the ion concentration was as high as 3.0 M. The critical gelation concentration of ions was also influenced by the concentration and molecular weight of PVA (**Figure 2.6**). By comparing the critical gelation concentrations of 5 wt% PVA in different anions, a typical Hofmeister series emerged following the sequence $SO_4^{2-} > CO_3^{2-} > Ac^- > Cl^- > NO_3^- > I^-$, with Na^+ as the constant counterion. The cations had similar specific effect on the gelation of PVA. However, the effect was less pronounced than that of anions, which was consistent with other phenomenon caused by Hofmeister effect[28]. When Cl^- was used as the constant counterion, the critical gelation concentration of cations was 1.5 M at a minimum, and the PVA could not be gelled by Li^+, Ca^{2+} and Mg^{2+} (**Figure 2.5**e). The cation sequence based on critical PVA gelation concentration followed $K^+ > Na^+ \approx Cs^+ > Li+ \approx Ca^{2+} \approx Mg^{2+}$. With systematic experiments, a chart of concentration versus ions was obtained as shown in **Figure 2.6** d and e, respectively for anions and cations. In the chart, the blue and yellow regions represent the corresponding ions and their concentrations for gelation or non-gelation, respectively.

5 wt% PVA Mw:89000-98000

Salt Concentration	Na_2SO_4	$NaNO_3$
1M	√	×
0.5M	√	×
0.1M	×	×

PVA Mw:89000-98000, salt concentration: 1M

PVA Concentration	Na_2SO_4	$NaNO_3$
15%	√	√
10%	√	×
5%	√	×
1%	×	×

PVA concentration 10% Salt concentration: 1M

PVA Mw	Na_2SO_4	$NaNO_3$
27K	×	×
89K-98K	√	×
195K	√	×

Figure 2.6 The influences of the salt concentration, polymer concentration and molecular weight on the gelation.

2.4.2 Tunable Mechanical Properties of PVA hydrogels via Hofmeister Effect

The gelation occurred because of the salting-out effect, during which the aggregation of PVA chains were rearranged by ions. Therefore, this effect could be applied to tune the mechanical properties of the PVA hydrogels. To confirm this, PVA hydrogels made with 3 freeze-thaw cycles, after which the PVA solution became a translucent hydrogel (**Figure 2.7**). Then the obtained hydrogels were soaked in different salt solutions for 24 hours and were washed with abundant DI water to remove the excess salts. Note that structural change of the PVA hydrogels soaked in Na_2SO_4 were irreversible with removal of the ions by washing and remained unchanged even after immersion in water for three months (**Figure 2.8**). This confirmed that during the salting-out

28

process, the ions only induced the aggregation of the polymer chains, but did not serve as components in the aggregated hydrogel[42]. Afterwards, the mechanical properties of the PVA hydrogels soaked in different salts were characterized systematically.
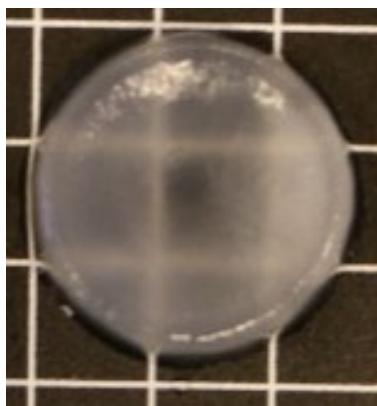
Figure 2.7 The image of the PVA hydrogel with 3 cycles of freeze-thaw processes.
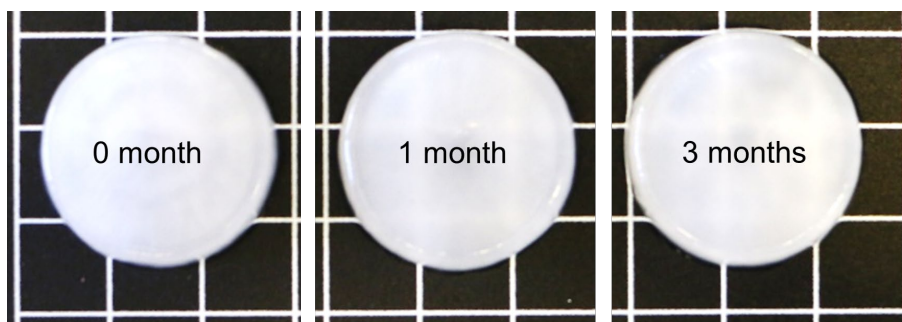
Figure 2.8 The images of the PVA-SO$_4$ soaked in pure water for 0 month, 1 month and 3 months, respectively.

Figure 2.9 a and b showed the typical stress-strain curves of PVA hydrogels treated with different sodium salts and chloride salts chosen based on the Hofmeister series. Among the anion series,

PVA hydrogel immersed in solution of Na_2SO_4 had the largest ultimate stress (2.2 MPa) and strain (1400%), while the PVA hydrogel immersed in I⁻ had the smallest ultimate stress (50 kPa) and strain (300%) (**Figure 2.9**d).
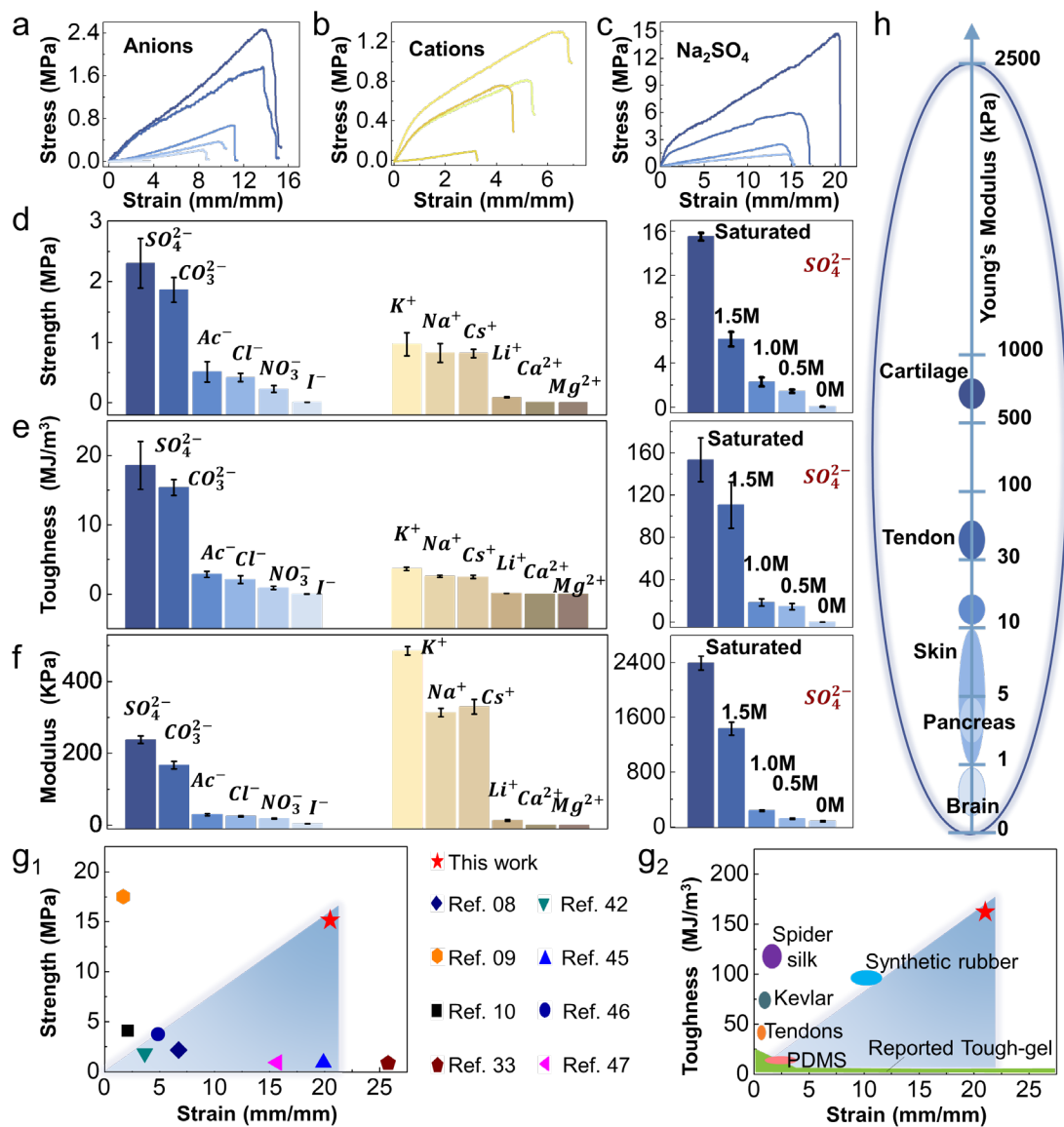
Figure 2.9 Tunable mechanical properties of PVA hydrogels by various ions. (a-c) Representative stress−strain curves of PVA hydrogels soaked in 1 M sodium salts (a), 3 M chloride salts (b), and Na_2SO_4 with concentration range from 0 M to saturated (c). (d-f) Strengths (d), toughness (e) and

moduli (f) of PVA hydrogels tuned by various anions (with Na^+ as the constant counterion); different cations (with Cl^- as the constant counterion); and Na_2SO_4 with concentrations ranging from 0 M to saturated. (g) Diagrams of ultimate strength versus ultimate strain (g_1), and toughness versus ultimate strain (g_2) of the hydrogels treated with different ions compared with other tough hydrogels and polymers reported in references. (h) The moduli ranges of soft tissues in the human body and the PVA hydrogels regulated by ions with different concentrations. The green circle refers to the moduli range of the as-prepared PVA hydrogels.

Systematically, the strength and toughness of PVA hydrogels of various anions followed the order: $SO_4^{2-} > CO_3^{2-} > Ac^- > Cl^- > NO_3^- > I^-$. Similar to the observations made with gelation process, the effects of cations were less pronounced than those of the anions. Here, the stress-strain curves of PVA hydrogels soaked in 3.0 M chloride salts were measured. As shown in Figure 2b and d, the PVA hydrogel of KCl gives the largest stress (1.1 MPa) as the hydrogel was stretched to 700%. At the same time, the stress of PVA hydrogel immersed in LiCl was only 100 kPa as the hydrogel was stretched to 300% (**Figure 2.9** b and d). Note that the stress-strain curves of gels treated by Ca^{2+} and Mg^{2+} could not be measured because the PVA hydrogel almost dissolved in these salt solutions. By comparing the strength and toughness, a cation series was obtained: $K^+ > Na^+ \approx Cs^+ > Li^+ > Ca^{2+} \approx Mg^{2+}$.

Furthermore, the specific ion effect is usually concentration sensitive. Here, Na_2SO_4 was used as an example to study the influence of concentrations. As concentration of Na_2SO_4 increased from

31

0.5 M to saturated (~1.8 M at room temperature), the ultimate stress and maximum strain of the resulted hydrogel increased significantly from 1.0 MPa to 15.0 MPa and from 1500% to 2100%, respectively (**Figure 2.9**c). Toughness and modulus exhibited similar trends, which increased from 3.1 MJ/m^3 to 153.41 MJ/m^3 and from 48 kPa to 2500 kPa, respectively (**Figure 2.9**d, e and f). Note that the hydrogel soaked with saturated Na_2SO_4 showed higher ultimate stress and strain that surpassed the values reported in previous works studying tough hydrogels (**Figure 2.9**g$_1$) by 10-10^3 fold, and the corresponding toughness was larger than the water-free polymers like PDMS, synthetic rubber and natural spider silk (**Figure 2.9**g$_2$). Furthermore, via changing the ions or concentrations, the modulus of PVA hydrogels can be easily tuned within a broad range, from near 0 kPa to 2500 kPa, which covered all the moduli of soft tissues in the human body[40,43] as shown in **Figure 2.9**h. With such a large range of moduli and biocompatibility, the PVA hydrogels can offer a very promising material platform for stem cells to differentiate into various functional cells, ranging from extremely soft brain cells to very rigid cartilage cells. Additionally, in contrast to traditional hydrogels with certain mechanical properties achieved by ionic crosslinking[44,45], the ions used here, functioned as a gelation trigger rather than the components of the hydrogels, which was washed out with of DI water and left the final hydrogel structure ion-free without altering its properties or comprising the biocompatibility.

2.4.3 Tunable Microstructure of PVA hydrogel via Hofmeister Effect

Along with the tunable mechanics with large ranges, the water contents remained high, with slight

differences among the PVA hydrogels soaked in different ions solutions. As shown in **Figure 2.10**, the water contents of PVA hydrogels treated with various sodium salts followed the order: Na_2SO_4 < Na_2CO_3 < NaAc < NaCl < $NaNO_3$ < NaI.
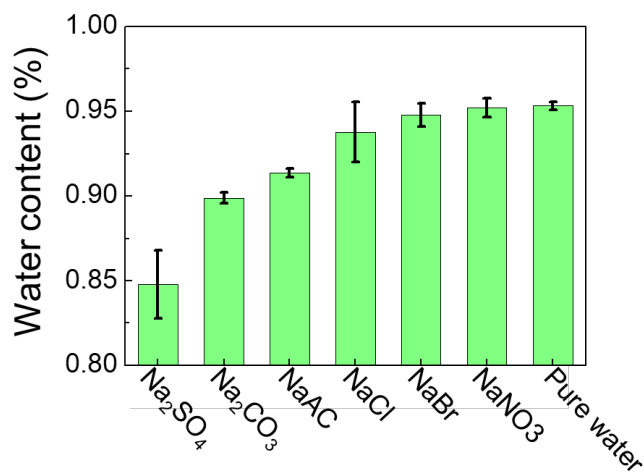
Figure 2.10 The water contents of the PVA hydrogels treated with various salts and pure water.

XRD was used to characterize the crystalline domains of the PVA hydrogels. As shown in **Figure 2.11**a, after soaking in 1 M Na_2SO_4, there were obvious crystalline aggregates in the hydrogel which yielded the opaque appearance of the hydrogel via scattering of light. PVA hydrogel soaked in $NaNO_3$ (termed as PVA-NO_3) had no apparent crystalline peaks (**Figure 2.11**b), therefore was translucent. Hence, judging from the XRD diffraction and the opacity of PVA hydrogel soaked with Na_2SO_4 (termed as PVA-SO_4), there were crystalline domains dispersed between random coil chains in the PVA hydrogel as shown in the schematic in **Figure 2.5**a. However, there were few crystalline aggregates in the PVA-$NaNO_3$ (**Figure 2.5**c). The difference between the crystallinities of PVA-SO_4 and PVA-$NaNO_3$ were further confirmed with DSC as shown in **Figure 2.12**. **Figure**

2.11c, d and **Figure 2.13** showed the morphologies of PVA-SO$_4$ and PVA-NO$_3$. The PVA-SO$_4$ hydrogel had the highest pore density and the smallest pore size of around 200 nm among all tested ions of the same concentration (**Figure 2.11**c and **Figure 2.13**). Its structure presented continuous networks of nano-fibrils. By contrast, in PVA-NO$_3$ hydrogel, most pores were around 2 μm in size, with a few smaller pores on the walls of the larger pores (**Figure 2.11**d). Such a significant difference in morphology between PVA-SO$_4$ and PVA-NO$_3$ was believed to originate from the aforementioned specific ion effect. Ions such as SO$_4^{2-}$ and CO$_3^{2+}$ triggered the salting-out of the polymers, thereby resulting in the spontaneous collapse of polymer chains and formation of the small pores. Ions like NO$_3^-$ and I$^-$ led to the salting-in of the polymer, which resulted in partial dissolution of the polymer, and has led to larger pores (**Figure 2.13** and **Figure 2.14**).
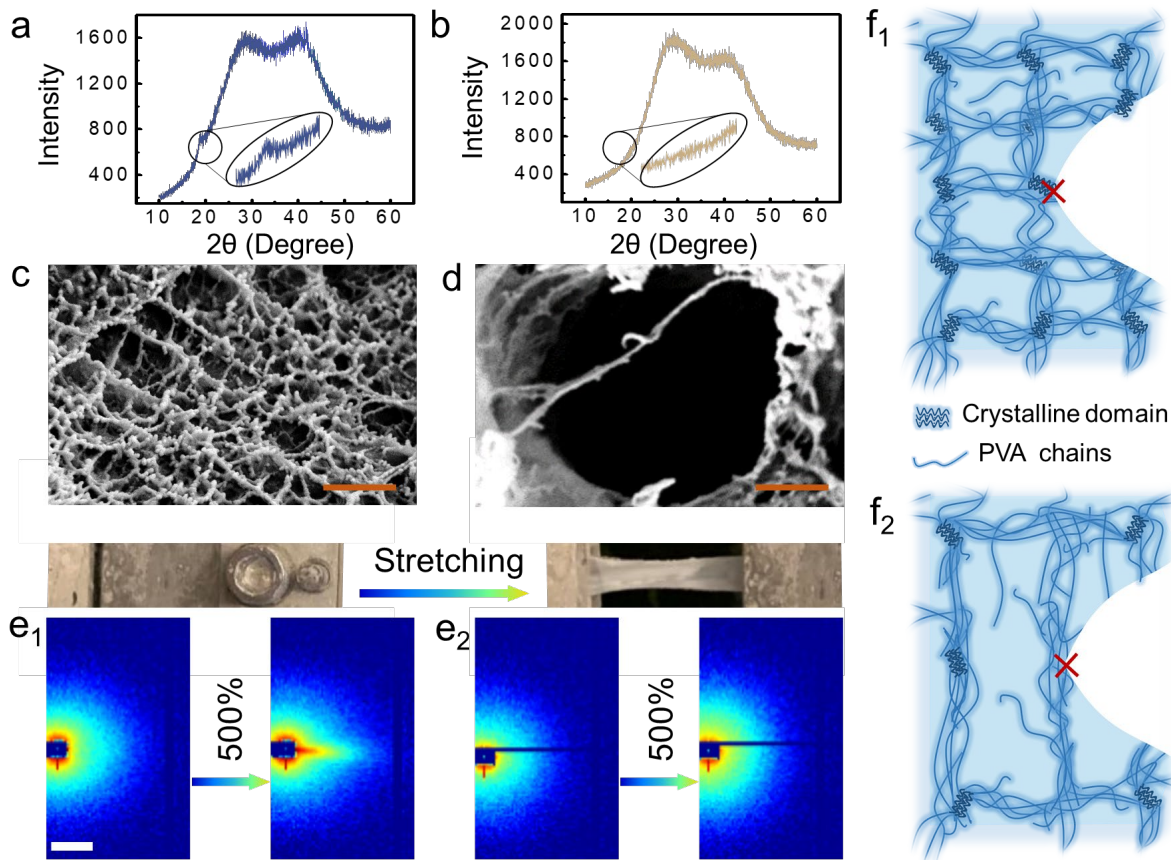
Figure 2.11 Characterizations of PVA hydrogels soaked in 1 M Na_2SO_4 and $NaNO_3$. (a, b) XRD spectra of PVA hydrogels soaked with 1.0 M Na_2SO_4 and $NaNO_3$. The inset shows the enlarged spectra to compere the crystalline information. (c and d) SEM images of PVA-SO_4 and PVA-NO_3. SEM scale bars 500 nm, (e) SAXS patterns of PVA-SO_4 and PVA-NO_3 during tensile loading. SAXS scale bar 0.025 $Å^{-1}$. (f) The schematic structures of PVA-SO_4 and PVA-NO_3, with different densities of nano-fibrils and crystalline domains and thus different crack blunting and pinning effects.
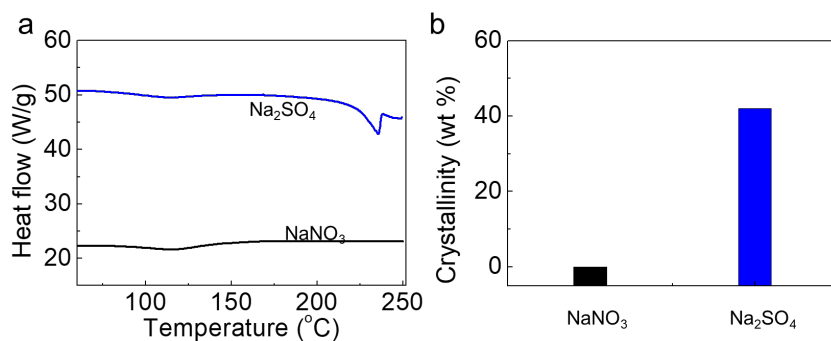
Figure 2.12 Characterization of crystallinities of PVA hydrogels. (a) Representative DSC curves of PVA-SO$_4$ and PVA-NO$_3$. (b) Crystallinities of PVA-SO$_4$ and PVA-NO$_3$ in the dried gels.
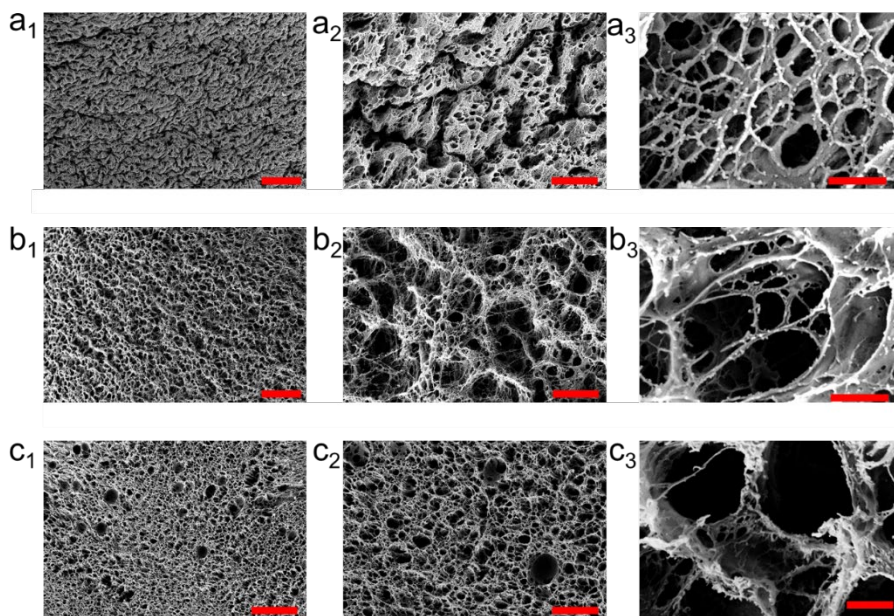
Figure 2.13 SEM images of the PVA hydrogels treated with (a) 1 M Na$_2$SO$_4$, (b) 1 M NaAc and (c) 1 M NaNO$_3$. 10 wt% PVA solutions were freeze-thawed for 3 cycles to make hydrogels, and the hydrogels was soaked in the salts solutions at room temperature. Scale bars of a$_1$ and b$_1$ = 200 μm, scale bar of c$_1$ = 100 μm, scale bars of a$_2$, b$_2$ and a$_3$ = 40 μm, scale bars of a$_3$, b$_3$ = 400 nm, scale bar of c$_3$ = 2 μm.
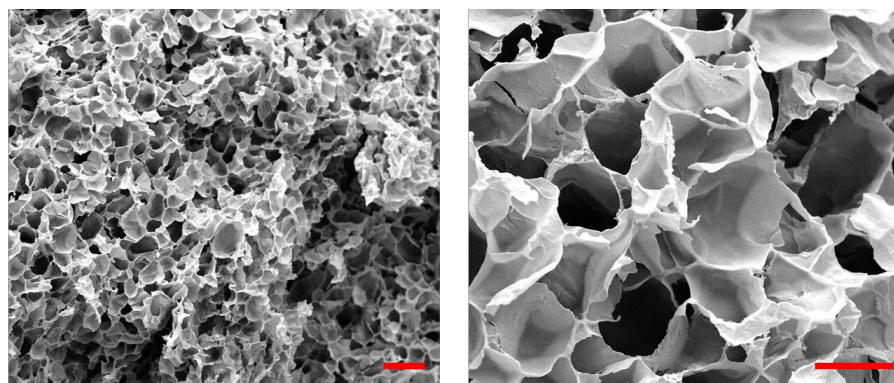
Figure 2.14 SEM images of the PVA hydrogel (10 wt% PVA, freeze-thawed for 3 cycles) without soaking in salts solutions. Scale bars are 20 and 10 μm respectively.

For PVA-SO_4 during stretching, the nano-fibril spacing decreased significantly as the network became partially aligned, as indicated by the stretch of SAXS pattern perpendicular to the stretching direction (**Figure 2.11**e_1). The average nano-fibril spacing decreased from ~90 nm to ~30 nm (**Figure 2.15**) when the strain increased from 0% to 500%. Such scattering difference was not observed for PVA-NO_3, which had no structural features of the same length scale (**Figure 2.11**e_2). From a fracture mechanics perspective, there were three reasons why the PVA-SO_4 was much tougher than the PVA-NO_3. First, because of the two opposite effects, salting-out and salting-in, the density of polymer chains in PVA-SO_4 was higher than that in PVA-NO_3 (also verified by the different water contents in these two hydrogels as shown in **Figure 2.10**). Second, during the salting-out process, abundant hydrogen bonds were formed which resulted in strong aggregation and partial crystallization of the polymer chains (**Figure 2.5**b and **Figure 2.11** a), while PVA-NO_3

went through a reverse process of salting-in (**Figure 2.5** c and **Figure 2.11**b). Therefore, the density

of crystalline domains in PVA-SO$_4$ was much higher than that in PVA-NO$_3$. The structures and

material elasticity were strengthened and improved by the crystalline domains which acted as rigid

high functionality cross-linkers[11]. Meanwhile, the crystalline domains delayed the fracture of

individual nano-fibrils by crack pinning leading to the toughness enhancement[10] (**Figure 2.11**f).

Third, compared to PVA-NO$_3$ which has no nano-fibril features, when PVA-SO$_4$ was stretched, the

decrease in inter-fibril spacing led to an increase in concentration of nano-fibrils per unit cross-

section, which in-situ strengthened the material (**Figure 2.11**e). In short, PVA-SO$_4$ obtained

extraordinary toughness and largest ranges of strength and moduli because of the densification

enhancements on three levels: polymer chains, crystalline domains, and nano-fibrils (**Figure 2.11**).
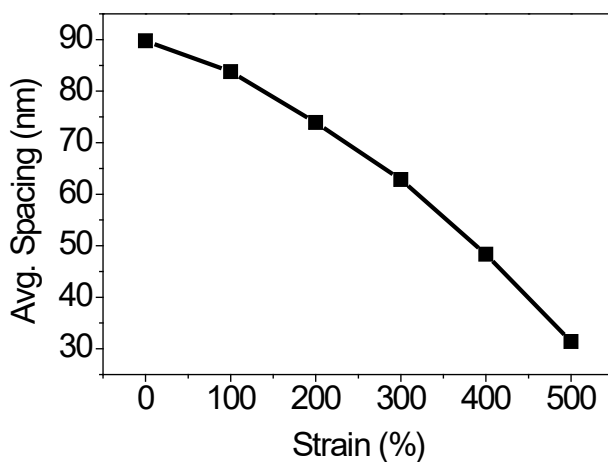
Figure 2.15 Average space between the nano-fibrils calculated from SAXS patterns during

stretching.

2.4.4 Reversible Mechanical Properties via Hofmeister Effect

The mechanical properties of PVA hydrogel can be altered by different ions dynamically. As shown in **Figure 2.16**a, after soaking in saturated Na_2SO_4 and washed with excess water, the PVA hydrogel became opaque and shrunk slightly. Subsequently, the opaque PVA hydrogel was soaked in 3 M $CaCl_2$ for 48 h, where it transformed into a translucent hydrogel that swelled back slightly. Meanwhile, the corresponding strength, toughness, and modulus were tuned dynamically from 15.53 MPa, 153.41 MJ/m^3 and 2500 kPa to 0.09 MPa, 2.48 MJ/m^3, and 34 kPa, respectively. Such hydrogel with variable mechanics can be potentially used as neuron probes, which need to be rigid initially to easily insert into brain tissue, and as soon as after insertion, become softened subsequently to match the modulus of neuron cells[3] ($\sim$ 10 kPa). Here, to mimic the brain tissue, a soft hydrogel made of polyacrylamide with a brain-tissue-matching modulus ($\sim$ 10 kPa) was utilized. When the PVA hydrogel probe was toughened by Na_2SO_4, it could penetrate the soft polyacrylamide hydrogel as shown in Figure 2.16b_1, while the soft PVA hydrogel soaked in 1 M $CaCl_2$ could not (**Figure 2.16** b_2 and **Figure 2.17**). Furthermore, to demonstrate on-site stiffness tuning, *i.e.*, the hydrogel can be softened after "implantation", the hydrogel probe inserted in the brain-mimicking hydrogel was soaked in a 3 M $CaCl_2$ solution. As shown in **Figure 2.16**c, the originally white hydrogel probe became translucent gradually over 48 h of soaking, indicating that the PVA hydrogel probe can be *in-situ* softened by ions even while constrained inside another matrix. This on-site stiffness tunability presents attractive advantages and opportunities for applications that require local tuning of material properties, unachievable with conventional materials whose properties are set once produced or can be tuned only with extreme conditions

such as high temperature[23].
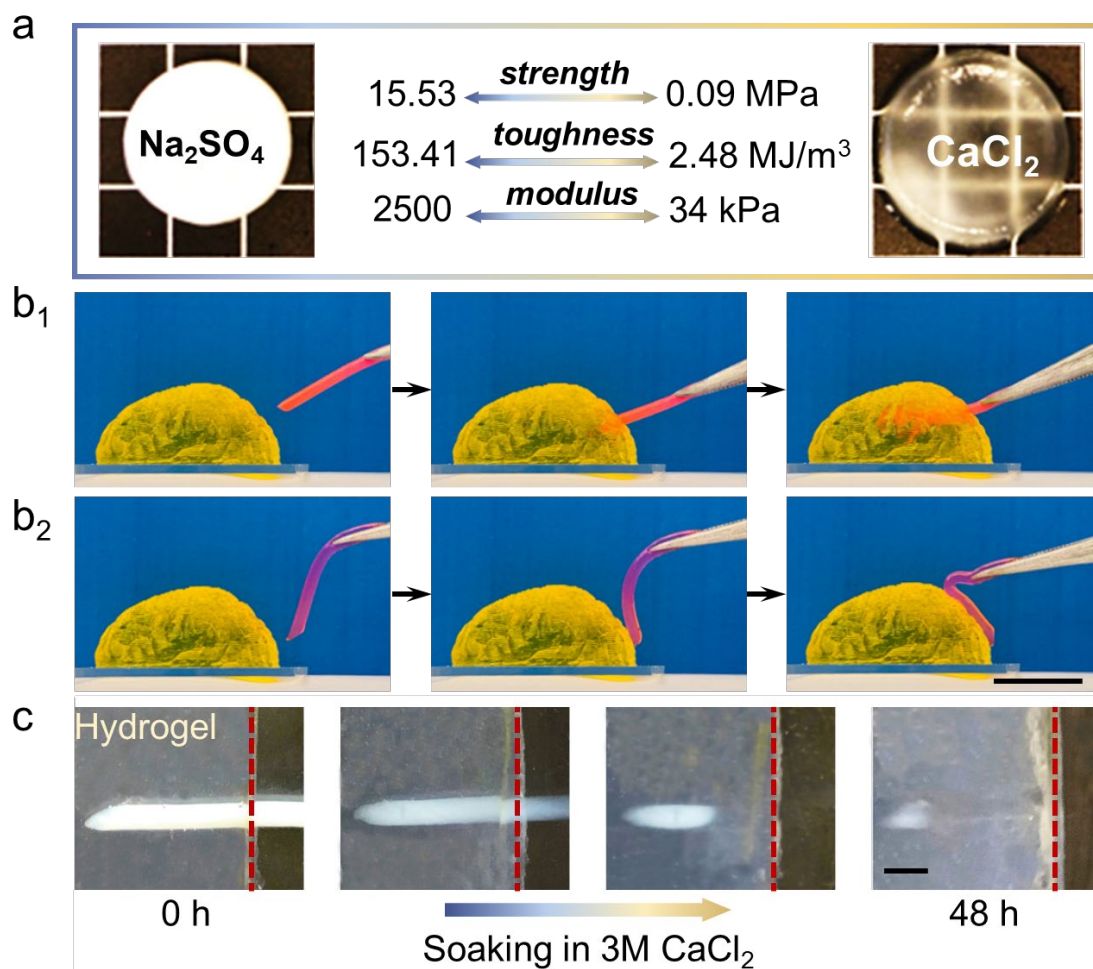
Figure 2.16 PVA hydrogel softened or toughened by Na_2SO_4 and $CaCl_2$, respectively. (a) The optical images of PVA hydrogel after soaking with solutions of saturated Na_2SO_4 and 3 M $CaCl_2$. The PVA hydrogel was toughened by Na_2SO_4 and then softened by $CaCl_2$, with the corresponding values of strength, toughness and modulus listed. (b1) A stiff PVA hydrogel toughened by 1 M Na_2SO_4 penetrating into a soft brain-tissue-mimicking hydrogel. (b2) A soft PVA hydrogel treated with 1 M $CaCl_2$ could not penetrate the same brain-tissue-mimicking hydrogel. The hydrogel probes were dyed with Rhodamine B for visualization. (c) The hydrogel probe inserted in the brain-

mimic hydrogel was soaked in a 3 M CaCl$_2$ solution. Over 48 h, the original white hydrogel probe gradually became translucent. Scale bars of b and c are 1 cm and 1 mm respectively.
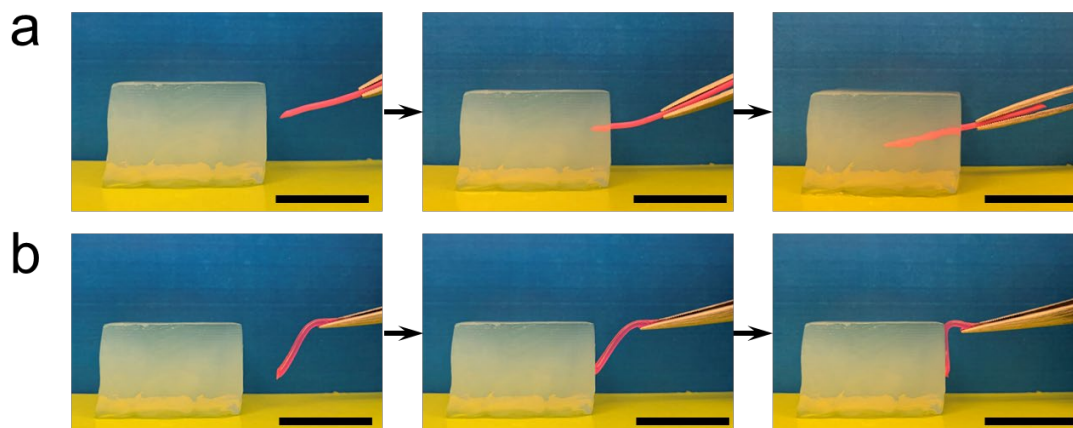
Figure 2.17 (a) A stiff PVA hydrogel toughened by 1 M Na$_2$SO$_4$ can penetrate into a soft hydrogel whose modulus is comparable with brain tissue. (b) A soft PVA hydrogel treated with 1 M CaCl$_2$ could not penetrate the hydrogel. Scale bar = 1cm.

2.5 Conclusion

In summary, with a freeze-soak method, it was discovered that ions have a specific effect on the gelation of PVA. The effects of different ions on the ion-facilitated gelation and the toughening of PVA followed such orders: SO$_4^{2-}$ > CO$_3^{2-}$ > Ac$^-$ > Cl$^-$ > NO$_3^-$ > I$^-$ for anions and K$^+$ > Na$^+$ ≈ Cs$^+$ > Li$^+$ ≈ Ca^{2+} ≈ Mg^{2+} for cations. The ion-specific gelation originated from the different interaction modes with PVA polymer chains that resulted in either salting-out or salting-in. The PVA hydrogels showed mechanical properties that followed the Hofmeister series after being treated with various salts solutions. In addition to the different types of ions used, higher salt concentration also

enhanced their influence on the mechanical properties of the produced hydrogels. Therefore, by changing the types and concentrations of salts, the mechanical properties of PVA hydrogels could be tuned with a large window. Specifically, the tensile strength was tuned from 0 kPa to 15 MPa, toughness was regulated from 0 MJ/m^3 to 150 MJ/m^3, and the elongation varied from 0 % to 2100 %. Specially, the PVA hydrogel treated with saturated Na$_2$SO$_4$ solution showed the largest strength (15 MPa), toughness (150 MJ/m^3) and elongation (2100 %), which can be considered as an ultra-tough and highly-stretchable hydrogel. The hydrogel soaked with saturated Na$_2$SO$_4$ showed higher ultimate stress and strain surpassing the values reported in previous works of tough hydrogels by 10-10^3 fold, and the toughness of hydrogels soaked with saturated Na$_2$SO$_4$ is higher than that of water-free polymers like PDMS, synthetic rubber and natural spider silk. The hydrogels treated with different salts showed significantly different mechanical properties, which resulted from the various degrees of aggregation of polymers chains because of the specific interactions among the ions, water molecules and polymer chains at the molecular level. In this study, PVA was used as an exemplary polymer to demonstrate the regulation of mechanical properties by tuning the aggregation states of polymer chains. Since the classic Hofmeister effects is universal for hydrophilic polymers, the presented strategy can be extended to many other systems composed of hydrophilic polymers.

Furthermore, the demonstration of onsite dynamically tunable stiffness presented a potentially new strategy to design hydrogel-based neuron probes with the stiffness tuned by ions. Although

currently the salt concentration used in the proof of concept here is higher than that in human body,

through optimization the hydrogel neuron probe may be further improved for practical applications.

Additionally, the ions utilized for fabricating the hydrogels only induced the aggregation of

polymer chains and the formation of structures, instead of serving as the components of hydrogels.

Hence, after soaking treatment in ions solutions and subsequently washing out the ions completely,

the final ion-free PVA hydrogels could well maintain their properties and the highly desirable

biocompatibility without interferences from potentially hazardous ions used when making the

hydrogels. With this facile method and the excellent in-situ and broad-range tunability of

mechanical properties, PVA hydrogels can be expanded to a broader-based platform to meet the

needs of a variety of areas ranging from biomedicine to robotics and wearable electronics.

2.6 References

[1] K. Y. Lee, D. J. Mooney, *Chem. Rev.* **2001**, *101*, 1869.

[2] J. Li, D. J. Mooney, *Nat. Rev. Mater.* **2016**, *1*.

[3] Y. Liu, J. Liu, S. Chen, T. Lei, Y. Kim, S. Niu, H. Wang, X. Wang, A. M. Foudeh, J. B. H. Tok, Z. Bao, *Nat. Biomed. Eng.* **2019**, *3*, 58.

[4] Y. Huang, M. Zhong, F. Shi, X. Liu, Z. Tang, Y. Wang, Y. Huang, H. Hou, X. Xie, C. Zhi, *Angew. Chemie - Int. Ed.* **2017**, *56*, 9141.

[5] X. Yao, J. Liu, C. Yang, X. Yang, J. Wei, Y. Xia, X. Gong, Z. Suo, *Adv. Mater.* **2019**, *31*, 1903062.

[6]   H. Yuk, T. Zhang, S. Lin, G. A. Parada, X. Zhao, *Nat. Mater.* **2016**, *15*, 190.

[7]   H. Yuk, S. Lin, C. Ma, M. Takaffoli, N. X. Fang, X. Zhao, *Nat. Commun.* **2017**, *8*, 14230.

[8]   J.-Y. Sun, X. Zhao, W. R. K. Illeperuma, O. Chaudhuri, K. H. Oh, D. J. Mooney, J. J. Vlassak, Z. Suo, *Nature* **2012**, *489*, 133.

[9]   L. Han, X. Lu, K. Liu, K. Wang, L. Fang, L. T. Weng, H. Zhang, Y. Tang, F. Ren, C. Zhao, G. Sun, R. Liang, Z. Li, *ACS Nano* **2017**, *11*, 2561.

[10]   S. Lin, J. Liu, X. Liu, X. Zhao, *Proc. Natl. Acad. Sci. U. S. A.* **2019**, *116*, 10244.

[11]   X. Zhao, *Soft Matter* **2014**, *10*, 672.

[12]   H. Fan, J. P. Gong, *Macromolecules* **2020**, acs. macromol.0c00238.

[13]   A. Kumar, S. S. Han, *Int. J. Polym. Mater. Polym. Biomater.* **2017**, *66*, 159.

[14]   O. Chaudhuri, L. Gu, D. Klumpers, M. Darnell, S. A. Bencherif, J. C. Weaver, N. Huebsch, H. P. Lee, E. Lippens, G. N. Duda, D. J. Mooney, *Nat. Mater.* **2016**, *15*, 326.

[15]   A. S. Mao, J. W. Shin, D. J. Mooney, *Biomaterials* **2016**, *98*, 184.

[16]   F. Trensz, F. Lucien, V. Couture, T. Söllrald, G. Drouin, A. J. Rouleau, M. Grandbois, G. Lacraz, G. Grenier, *Skelet. Muscle* **2015**, *5*, 1.

[17]   W. J. Hadden, J. L. Young, A. W. Holle, M. L. McFetridge, D. Y. Kim, P. Wijesinghe, H. Taylor-Weiner, J. H. Wen, A. R. Lee, K. Bieback, B. N. Vo, D. D. Sampson, B. F. Kennedy, J. P. Spatz, A. J. Engler, Y. S. Cho, *Proc. Natl. Acad. Sci. U. S. A.* **2017**, *114*, 5647.

[18]   J. Li, D. Han, Y. P. Zhao, *Sci. Rep.* **2014**, *4*, 1.

[19]   J. Lee, O. Jeon, M. Kong, A. A. Abdeen, J. Shin, H. N. Lee, Y. Bin Lee, W. Sun, P. Bandaru, D. S. Alt, K. Lee, H. Kim, S. J. Lee, S. Chaterji, S. R. Shin, **2020**, 1.

[20]   J. Blacklock, A. Vetter, A. Lankenau, D. Oupický, H. Möhwald, *Biomaterials* **2010**, *31*, 7167.

[21]   I. Hopp, A. Michelmore, L. E. Smith, D. E. Robinson, A. Bachhuka, A. Mierczynska, K. Vasilev, *Biomaterials* **2013**, *34*, 5070.

[22]   S. K. Seidlits, Z. Z. Khaing, R. R. Petersen, J. D. Nickels, J. E. Vanscoy, J. B. Shear, C. E. Schmidt, *Biomaterials* **2010**, *31*, 3930.

[23]   J. R. Capadona, K. Shanmuganathan, D. J. Tyler, S. J. Rowan, C. Weder, *Science (80-.).* **2008**, *319*, 1370.

[24]   Y. Qiu, E. Askounis, F. Guan, Z. Peng, W. Xiao, Q. Pei, *ACS Appl. Polym. Mater.* **2020**, *2*, 2008.

[25]   J. M. Korde, B. Kandasubramanian, *Chem. Eng. J.* **2020**, *379*, 122430.

[26]   P. Jungwirth, P. S. Cremer, *Nat. Chem.* **2014**, *6*, 261.

[27]   W. Kunz, J. Henle, B. W. Ninham, *Curr. Opin. Colloid Interface Sci.* **2004**, *9*, 19.

[28]   S. Wu, C. Zhu, Z. He, H. Xue, Q. Fan, Y. Song, J. S. Francisco, X. C. Zeng, J. Wang, *Nat. Commun.* **2017**, *8*, 1.

[29]   R. Du, Y. Hu, R. Hübner, J. O. Joswig, X. Fan, K. Schneider, A. Eychmüller, *Sci. Adv.* **2019**, *5*, 1.

[30]   L. M. Pegram, M. T. Record, *J. Phys. Chem. B* **2007**, *111*, 5411.

[31] Y. Zhang, P. S. Cremer, *Curr. Opin. Chem. Biol.* **2006**, *10*, 658.

[32] R. S. Carnegie, C. L. D. Gibb, B. C. Gibb, *Angew. Chemie - Int. Ed.* **2014**, *53*, 11498.

[33] Y. Yang, X. Wang, F. Yang, H. Shen, D. Wu, *Adv. Mater.* **2016**, *28*, 7178.

[34] Q. He, Y. Huang, S. Wang, *Adv. Funct. Mater.* **2018**, *28*, 1.

[35] Y. Zhang, S. Furyk, D. E. Bergbreiter, P. S. Cremer, *J. Am. Chem. Soc.* **2005**, *127*, 14505.

[36] J. Wei, Q. Wang, *Small Methods* **2019**, *3*, 1900558.

[37] M. Jaspers, A. E. Rowan, P. H. J. Kouwer, *Adv. Funct. Mater.* **2015**, *25*, 6503.

[38] J. Wang, M. Satoh, *Polymer (Guildf).* **2009**, *50*, 3680.

[39] Z. Jiang, *J. Appl. Crystallogr.* **2015**, *48*, 917.

[40] A. M. Handorf, Y. Zhou, M. A. Halanski, W. J. Li, *Organogenesis* **2015**, *11*, 1.

[41] H. Muta, M. Miwa, M. Satoh, *Polymer (Guildf).* **2001**, *42*, 6313.

[42] P. Lo Nostro, B. W. Ninham, *Chem. Rev.* **2012**, *112*, 2286.

[43] J. Liu, H. Zheng, P. S. P. Poh, H. G. Machens, A. F. Schilling, *Int. J. Mol. Sci.* **2015**, *16*, 15997.

[44] P. Lin, S. Ma, X. Wang, F. Zhou, *Adv. Mater.* **2015**, *27*, 2054.

[45] P. Lin, T. Zhang, X. Wang, B. Yu, F. Zhou, *Small* **2016**, *12*, 4386.

3. Hierarchical Anisotropic Hydrogels via Directional Freezing Assisted Salting Out

3.1 Introduction

Wood is light and strong; nacres are hard and resilient; muscles and tendons are soft and tough. These natural materials show a combination of normally contradicting mechanical properties, which is attributed to their hierarchical structures across multiple length scales[1]. Compared with natural load-bearing materials, the loose crosslinking, low solid content, and homogeneous structure make conventional hydrogels relatively weak and fragile for handling real-world applications, which often demand long service periods, high load or impact tolerance, and large deformation. Tremendous improvements have been made to strengthen and toughen hydrogels by introducing mechanisms for energy dissipation during loading, such as by forming double network[2–5], having dual crosslinking[6,7], self-assembly[8], inducing hydrophobic aggregation[9], and creating nano-crystalline domains[10,11]. These methods primarily focus on composition and molecular engineering, involving limited structural changes within a narrow length scale (molecular or nanoscale) and relatively simple structures compared to their complex structured natural counterparts.

Other advances take structural engineering approaches by creating anisotropic structures in hydrogels through methods of freeze casting[12–15], mechanical stretching[11,16–18], and

compositing[19,20]. For examples, directional freezing or ice templating is widely adopted due to its generic applicability to various polymers[13]. However, ice-templated hydrogels with micro-alignment have shown mechanical performance comparable to, or lower than that of homogeneous tough hydrogels made by molecular engineering methods. Mechanical stretching has also been used to create anisotropic micro/nanostructures[11,16–18]. Alternatively, instead of in-situ creating anisotropic structures within the hydrogel by ice templating and mechanical stretching, compositing method by addition of alien micro/nanoscale fiber-reinforcements into hydrogel has also been explored[20–23]. The mechanically-trained hydrogels and hydrogel composites have significantly improved strength and fracture toughness over homogeneous tough hydrogels, but also have limited stretchability or water content. These structural engineering approaches focus on optimizing the micro/nanostructures of existing hydrogels, yet it remains challenging to create simultaneously strong, tough, stretchable and fatigue-resistant hydrogels with more elaborately hierarchical structures across broader length-scales, like those observed in natural materials[24,25], while using a generic and facile approach.

Recently, anisotropic composite of modulus-contrasting fibers and matrix made of similar composition has shown effectiveness for maintaining stretchability while improving strength, fracture toughness and fatigue resistance[19,26]. Therefore, forming a hierarchically anisotropic single-composition hydrogel containing strong and stretchable fibers made of the same composition, would be promising for making water-laden hydrogels with simultaneous high

strength, toughness, stretchability and fatigue threshold.

3.2 Proposed Method

The alteration of polymer aggregation state could be realized by the simple addition of specific ions[27,28], known as the Hofmeister effect[29], where different ions have distinct abilities to precipitate polymers. With the aid of specific ions, modulus-contrasting structures could be formed out of the same polymer composition. Meanwhile, directional freezing could endow hydrogels with anisotropic structures at the larger (μm-mm) scales while promoting molecular concentrating. Herein, we propose to make hydrogels by the combination of molecular and structural engineering approaches. By combining directional freeze-casting and a subsequent salting-out treatment, which synergistically create hydrogel structures on different length scales across mm to molecular level, we have constructed strong, tough, stretchable and fatigue-resistant hydrogels with hierarchical and anisotropic structures.

3.3 Experimental and Characterization Section

3.3.1 Preparation of PVA solution

2 wt%, 5 wt%, 10 wt% and 20 wt% PVA solution was prepared by dissolving PVA powder in DI water under vigorous stirring and heating (70 °C). After degassing by sonication for 1 hr, a clear solution was obtained.

3.3.2 Preparation of salt solution

1.5 M concentration of sodium citrate solution was prepared by dissolving anhydrous sodium citrate powder in DI water. After sonication for 10 mins, a clear solution was obtained.

3.3.3 Fabrication of hydrogel

An ethanol bath of -80°C was used as the immersion bath for ice templating. The temperature was maintained using an EYELA-PSL1810 constant temperature bath. For the typical fabrication of the hierarchically aligned PVA hydrogels, 2-20% PVA aqueous precursor is poured into an acrylic container with peripheral thermal insulation, the bottom of the container is glass for good thermal conduction (**Figure 3.1**). The container is lowered into the ethanol bath at an immersion rate of 1 mm/min. The directionally frozen PVA solution is then immersed into a 1.5M sodium salt solution for gelation up to 4 days.
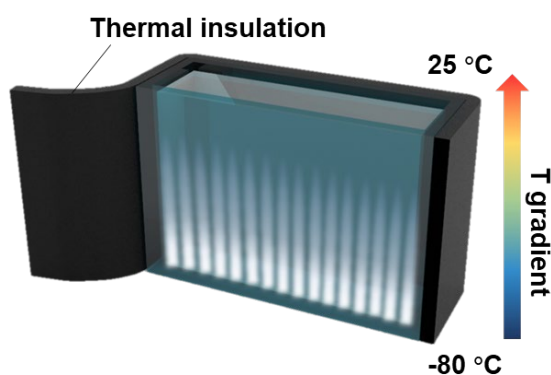
Figure 3.1 Illustration of the ice templating process

3.3.4 Tensile testing

Hydrogel were cut into dog-bone shapes specimens with gauge width of 2mm for regular tensile testing. The thickness of individual specimens was measured with a caliper, typically around 2mm. The HA-xPVA $\parallel$ specimens had microstructure parallel to the loading direction and the HA-xPVA $\perp$ specimens had microstructure perpendicular to the loading direction. The force-displacement data were obtained using a Cellscale Univert mechanical tester with 50N loading cell installed. The stress-strain curves were obtained by division of measured force by initial gauge cross-section area and division of measured displacement by initial clamp distance. Five hydrogel specimens were tested for each condition.

3.3.5 Pure shear tests

Hydrogels were cut into rectangular specimens with height of 40mm, width of 20mm for fracture tests. The thickness of individual specimens was measured with a caliper. Initial clamp distance of 1.5 mm was used for all specimens. All specimens had microstructure alignment parallel to the height direction. For pure shear tests, two identical sample (one notched, one unnotched) were loaded under the sample setup as a pair to obtain one fracture energy value[3]. Briefly, for the notched samples, an initial straight cut with length of 8mm were made from the middle of the long edge toward the center of the hydrogel and the specimen was loaded at strain rate of 10% /s. The critical strain (ε_c) for unstable propagation of the crack was obtained from the strain at maximum stress. The pairing notched specimens were subsequently loaded until $\varepsilon = \varepsilon_c$. The fracture energy value was obtained by multiplying the area under the stress-strain curve of unnotched specimens

with the initial clamp distance (H) as

$$\Gamma = H \int_0^{\varepsilon_c} \sigma d\varepsilon.$$

3.3.6 Fatigue tests

To examine the fatigue resistance of our hydrogel, we adopted the single-notch method [30]. The fatigue testing was performed in a water bath to prevent dehydration of the hydrogel. Cyclic tensile tests were conducted using notched samples with initial crack length (c_0) smaller than 1/5 of the width (L_0) of the sample. The sample width L_0 was much smaller than the sample height H_0. The cyclic force-displacement curves were obtained using the Cellscale Univert mechanical tester A digital camera was used to monitor the crack propagation of the hydrogel. All stretch cycles were conducted continuously without relaxation time. The energy release rate (G) was obtained using,

$$G = 2kcW$$

Where k is a varying function with strain and was empirically determined to be $k = 3/\sqrt{\varepsilon + 1}$, c is the crack length and W is the strain energy density of an unnotched sample with same dimension and stretched to the same strain (ε). It should be noted that when repeatedly stretching to high strains, the stress-strain curve slowly deviates from the initial loading and unloading curve as a result of plastic deformation, W is integrated from the loading part where the loading and unloading curves become stable and stopped changing.

3.3.7 SEM characterization

For characterization of the micro- and nano- structure of the hierarchically aligned hydrogels, all hydrogel samples were immersed in DI water for 24 hours before freeze drying using a Labconco FreeZone freeze drier. The freeze-dried hydrogels were cut along the aligned direction to expose the inside and sputtered with gold before carrying out imaging using a ZEISS Supra 40VP SEM.

3.3.8 Confocal characterization

Confocal microscopy carried out using a Leica DMi8 confocal microscopy. 0.1 wt% fluorescein sodium salt was added into the PVA precursor as fluorescent marker and florescent-HA-PVA hydrogels were made with the same subsequent fabrication procedures as regular HA-PVA hydrogels. The 488 nm laser channel was used to excite the fluorescent marker. The hydrogel was assigned pseudo color of green.

3.3.9 X-ray scattering characterization

The HA-PVA hydrogels were cut into 1 cm by 4cm rectangles and washed with DI water for before testing. The beamline station used was APS 8-ID-E (Argonne National Laboratory) equipped with Pilatus 1M detector. A customized linear stretcher was used to hold the samples and stretch on demand for *in-situ* X-ray scattering measurements. A MATLAB toolbox "GIXSGUI" was used for further editing and analysis of the scattering patterns[31].

3.3.10 Water content measurement

We measured the water content of the HA-PVA hydrogels by comparing weight before and after freeze-drying. Excess surface water was wiped away from the hydrogel surface and the hydrogel specimens were instantly frozen using liquid nitrogen followed by freeze-drying. Weight before (m_w) and after freeze drying (m_d) was measured with a balance. The water content was obtained by $(m_w - m_d)/m_w * 100\%$.

3.3.11 Crystallinity content measurement

Before freeze-drying the hydrogels for DSC measurements, we first used excess chemical cross-links induced by glutaraldehyde to fix the amorphous PVA polymer chains to minimize the further formation of crystalline domains during the air-drying process. The water content of the hydrogel f_{water} could be obtained by comparing the weight before and after freeze-drying. In a typical DSC measurement, we first weighed the total mass of the freeze-dried sample m. The sample was thereafter placed in a Tzero pan and heated up from 50 °C to 250 °C at the rate of 20 °C/min under a nitrogen atmosphere with flow rate of 30 mL/min. The curve of heat flow shows another narrow peak ranging from 200 °C to 250 °C, which correspond to the melting of the crystalline domains. The integration of the endothermic transition ranging from 200 °C to 250 °C gives the enthalpy for melting the crystalline domains per unit mass of the dry. Therefore, the mass of the crystalline domains $m_{crystalline}$ can be calculated as $m_{crystalline} = m * H_{crystalline}/H^0_{crystalline}$, where $H^0_{crystalline} = 138.6$ J/g is the enthalpy of fusion of 100 wt.% crystalline PVA measured at the equilibrium melting point T^0_m [32]. Therefore, the crystallinity in the dry sample X_{dry} can be calculated as $X_{dry} = m_{crystalline}/m$.

With measured water content from freeze drying, the crystallinity in the swollen state can be calculated as $X_{swollen} = X_{dry} * (1 - f_{water})$.

3.4 Result and Discussion

3.4.1 Formation of hierarchical structures

Using PVA as a model system, the PVA solution was first directionally frozen and then directly immersed in a kosmotropic salt solution (**Figure 3.2**a). A honeycomb-like micro-network with aligned pore walls was created during the directional-freezing process (**Figure 3.2**a & b)[12,13]. Importantly, the concentration and closer packing of polymer during freezing prepared the polymer chains for subsequent strong aggregation and crystallization induced by salting-out. For the choice of kosmotropic ions, we tested various species which allowed for a broad tunable range of the gel microstructures and mechanical properties. Among them, sodium citrate showed the best salting-out ability and the highest modulus (Supplementary Fig. S3). Under the influence of kosmotropic ions, the preconcentrated PVA chains strongly self-coalesced and phase separated from the original homogeneous phase, which in turn formed the mesh-like nanofibril network on the surface of the micron-scale aligned pore walls[33–35] (**Figure 3.2**d, e & f). The phase separation of PVA evolved over time for the elaborate structure and crystallinity to develop and mature, and the non-phase-separated portion of PVA remained in between the nanofibrils as a continuous membrane that filled the nanofibril network (**Figure 3.2**e).
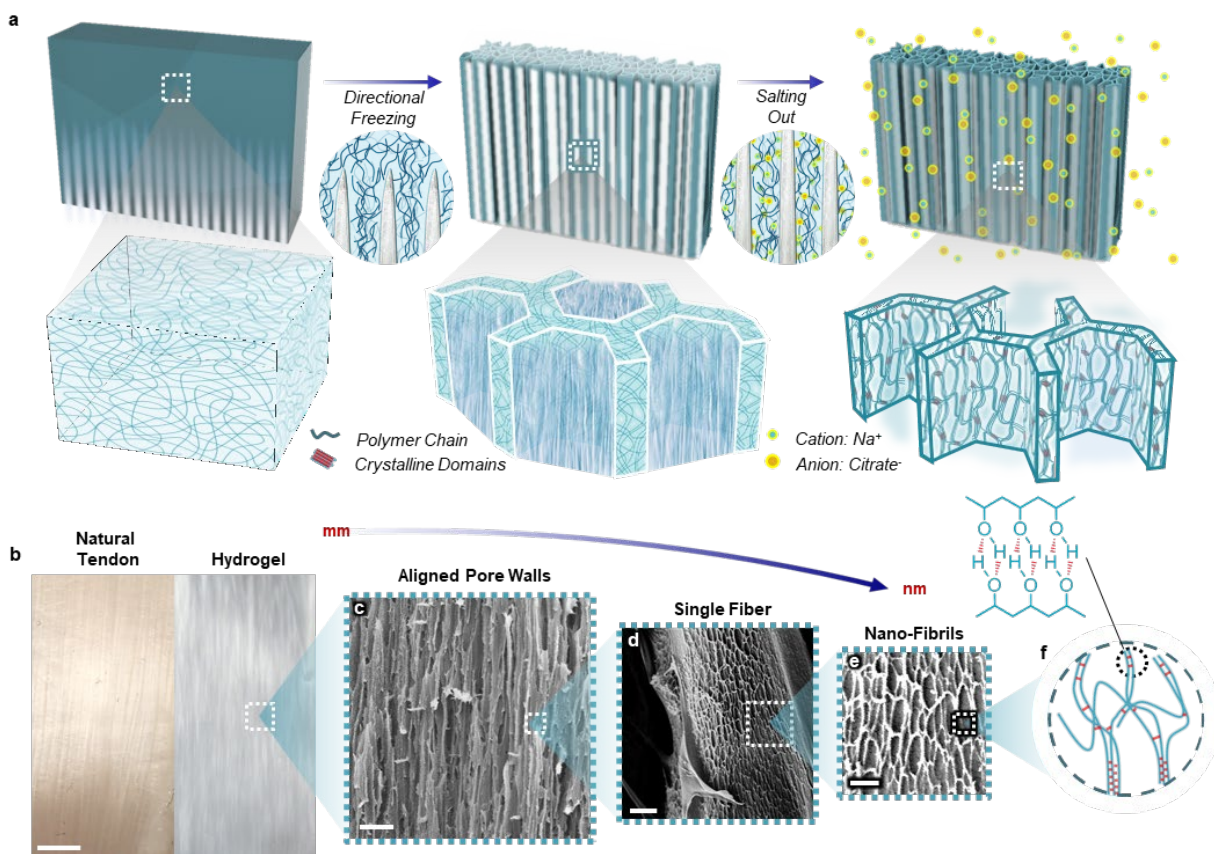
Figure 3.2 a, Freezing-assisted salting-out fabrication procedure of the HA-PVA hydrogels. Illustration of the structural formation and the polymer chain concentration, assembly and aggregation during freezing-assisted salting-out fabrication process. **b**, Macroscopic view of real tendon and the HA-5PVA hydrogel, scale bar 5mm. **c-e**, SEM images showing the microstructure (**c**, scale bar 50 µm) and nanostructure (**d**, scale bar 1 µm; **e**, scale bar 500 nm) of the HA-5PVA hydrogel. **f**, Molecular illustration of aggregated polymer chains into nanofibrils.

Mechanistically, ice templating concentrated PVA to form the aligned pore walls and increased the local concentration of PVA to higher values than the nominal concentration, while salting-out

strongly induced the aggregation and crystallization of PVA by phase separation to form the nanofibrils. To understand the synergistic effects of freezing and salting-out in this combined method, we designed a series of gel preparation methods with one or several factors missed out for direct comparisons (**Figure 3.3**). As control samples, the PVA hydrogels prepared by ice templating alone (**Figure 3.4**a) or salting-out alone (**Figure 3.3**f, **Figure 3.4**b) showed strength, toughness and stretchability all lower than those of HA-PVA hydrogels (**Figure 3.4**). Structure-wise, the ice-templated PVA hydrogel without the subsequent salting-out showed only aligned pore walls without the mesh-like nanofibrils (**Figure 3.5**), which suggested a weak aggregation of polymer chains in the absence of salting-out treatment. On the other hand, directly salting-out the PVA without prior freezing did not yield a bulk hydrogel and instead formed loosely and randomly entangled fibrils (**Figure 3.3**f), which suggested that pre-freezing the PVA solution provided necessary confinement and preconcentration of PVA chains for effective phase separation during the subsequent salting-out to form a strong bulk material. In short, such a freezing-assisted salting-out method presents a unique synergy that seamlessly integrates the advantages of the two techniques to boost the effect of aggregation, and is crucial for achieving the simultaneous high strength, toughness, stretchability and structural hierarchy in the HA-PVA hydrogels.
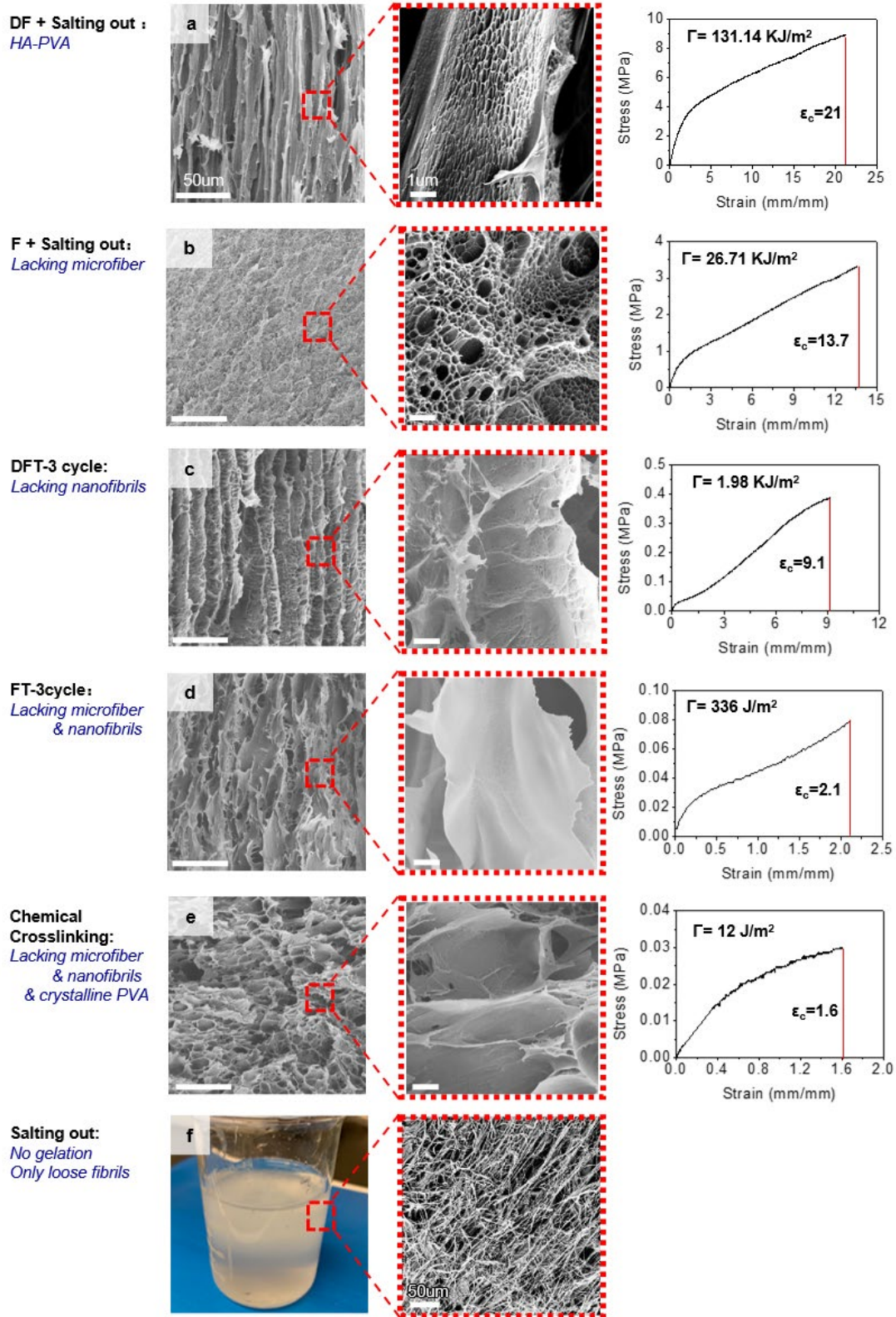
Figure 3.3. **a**, "DF + Salting out" hydrogel was prepared by directional freezing 5% PVA solution

and salting out in 1.5M sodium citrate solution for 24 hrs. **b**, "F + Salting out" hydrogel was prepared by non-directional freezing 5% PVA solution in fridge and salting out in 1.5M sodium citrate solution for 24 hrs. **c**, "DFT-3 cycle" hydrogel was prepared by directional freezing and thawing 5% PVA solution for 3 cycles. **d**, "FT-3 cycle" hydrogel was prepared by non-directional freezing in fridge and thawing 5% PVA solution for 3 cycles. **e**, "Chemical Crosslinking" hydrogel was prepared by mixing 0.5% glutaraldehyde and 0.5% hydrochloric acid into 5% PVA solution for gelation. **f**, "Salting-out" resulted in non-gelation. Only weak globules of loose and random nanofibrils made by directly adding 1.5M sodium citrate solution in 5% PVA solution.
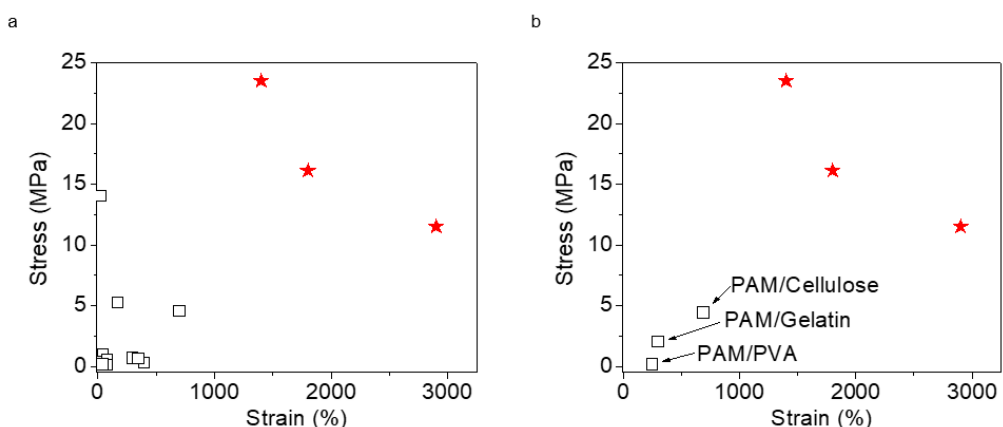
Figure 3.4 Mechanical properties of HA-PVA hydrogel compared to PVA hydrogels prepared by ice templating alone or salting-out alone. The HA-PVA hydrogels are shown with red stars, the ice-templated PVA hydrogels are shown in **a** as black squares, the salting-out PVA hydrogels are shown in **b** as black squares.
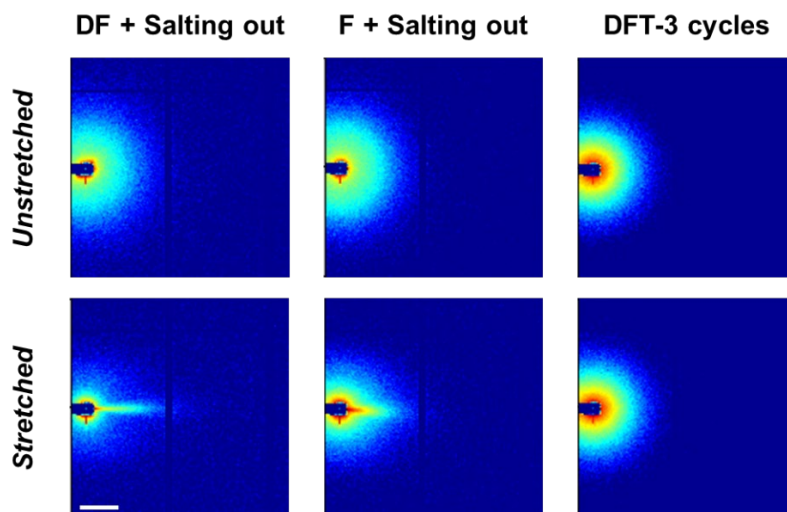
Figure 3.5 SAXS pattern of PVA hydrogel with different combination of structures during stretching. The scattering here is sensitive to structural less than 100nm.   With directional freeze-thaw (DFT-s cycles), only microfibers are formed and thus does not show scattering pattern changes before and after stretching. With the salting out treatment, nano-fibrils are formed and thus causes scattering pattern changes during stretching. The "DF+salting out" samples showed more fibril alignment than the "F+salting out" samples with the additional microscale alignment induced by directional freezing.   Scale bar = 0.05 Å^{-1}.

3.4.2 Strengthening while toughening

The HA-PVA hydrogels showed distinct mechanical properties in the parallel and perpendicular direction relative to the alignment direction due to the induced anisotropy (denoted as HA-xPVA for x% PVA precursor). Notably, the HA-5PVA hydrogels demonstrated superior toughness of 175 $\pm$ 9 MJ/m^3 upon stretching in the direction parallel to alignment, with an ultra-high ultimate stress of 11.5 $\pm$ 1.4 MPa and ultimate strain of 2900 $\pm$ 450% after 24 h salting-out (**Figure 3.6**a). Even

when stretched in the relatively weaker perpendicular direction, the HA-5PVA hydrogel was as tough as previously reported tough hydrogels[6,9,36]. The HA-5PVA hydrogel showed a gradual failure mode featuring stepwise fracture and pull-out of fibers typical for highly anisotropic materials (**Figure 3.6**a, right). There was no observable crack propagation perpendicular to the stretch direction during tensile loading of the hydrogel. Even with pre-existing cracks, the hydrogel showed a significant crack blunting ability and the initial crack did not advance into the material at high strains, showing a flaw-insensitive property[11] (**Figure 3.6**b).

The unusual combination of high strength and high toughness was correlated with three structural aspects at micro-, nano-, and molecular levels that evolved during synthesis (**Figure 3.6**c-e), which integrated multiple strengthening and toughening mechanisms. For instance, the densification of aligned micropore walls (**Figure 3.6**c) and nanofibrils (**Figure 3.6**d) strengthened the material by increasing the material density and toughened the material by increasing the energy dissipation during fracture. Additionally, the growing crystallinity during salting out (**Figure 3.6**e, **Figure 3.7**) strengthened each nanofibril and improved material elasticity by acting as rigid high functionality crosslinkers[25] and toughened the fibrils by virtue of their ability to delay the fracture of individual fibrils by crack pinning (**Figure 3.6**g)[10]. In short, the strengthening mechanism was mainly structural densification due to H-bonds and crystalline domain formation, and the toughening mechanisms were pull-out, bridging and energy dissipation by the fibrils (**Figure 3.6**g). During the evolution of these structures, the strength, stretchability and toughness of the HA-PVA

hydrogel simultaneously increased, attributed to the structural evolution across multiple length scales (**Figure 3.6**f).
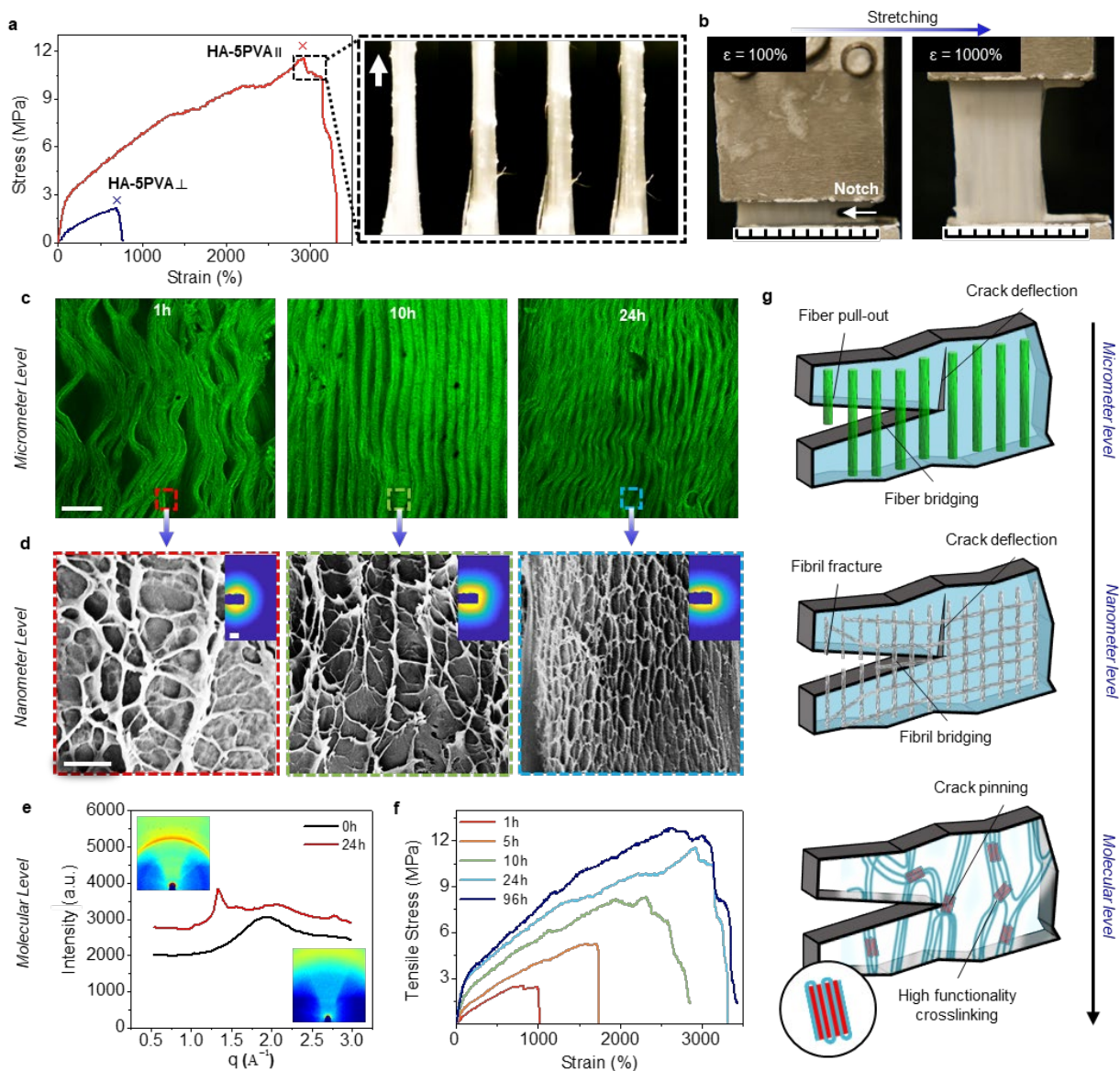
Figure 3.6 a, Tensile stress-strain curve of HA-5PVA hydrogel in the parallel (‖) and vertical (⊥) direction of alignment. The image to the right shows the fibrotic fracture of the HA-5PVA‖ hydrogel. **b**, Tensile loading of a HA-5PVA‖ hydrogel with pre-made crack. **c**, Confocal images showing the microstructures of HA-5PVA‖ hydrogels after different periods of salting-out in 1.5M

sodium citrate, scale bar 50 μm. **d**, SEM images showing the evolution of nanofibril network within the microstructure during the salting-out process, scale bar = 5 μm. The inset shows the corresponding SAXS pattern of freeze-dried HA-5PVA∥ hydrogel, scale bar 0.01 Å^{-1}. **e**, WAXS patterns of HA-5PVA∥ hydrogel (top) compared with PVA hydrogel of the same polymer content prepared by repeated freeze-thaw cycles (bottom) and the corresponding integrated scattering intensity with scattering vector q between 0.5 to 3 Å^{-1}, scale bar 0.5 Å^{-1}. The peak at q=1.35 Å^{-1} corresponds to the crystalline peak around 2Θ = 18 degrees in 8 keV XRD scattering. **f**, Stress-strain curve of HA-5PVA∥ hydrogels after different periods of salting-out in 1.5M sodium citrate. **g**, Illustration of toughening mechanisms from each length scale.
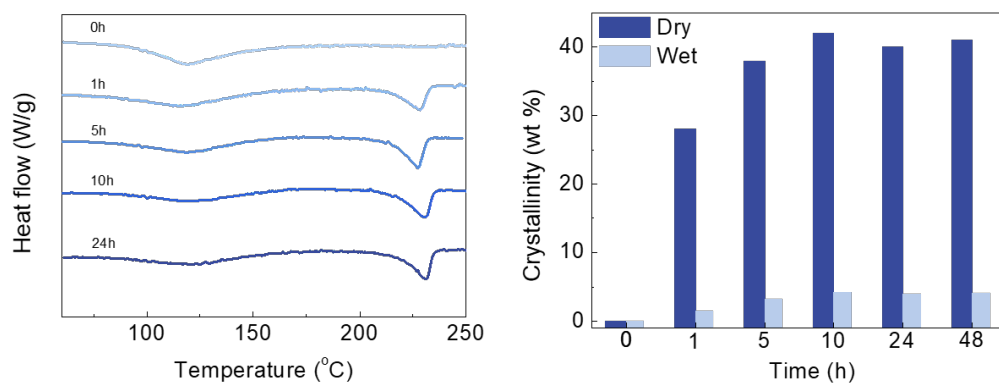
Figure 3.7 DSC measurement of crystallinity of HA-5PVA hydrogel. The 0 h sample corresponds to hydrogel prepared by ice templating with 1 freeze-thaw cycle alone.

3.4.3 Structure - property correlation

The three structural aspects from different length scales are intertwined in the present material. To

identify their roles in the synergistic strengthening and toughening, we compared the mechanical performances (critical stress σ_c, critical strain ε_c, and fracture energy Γ) of a series of PVA hydrogels with different combinations of those three structural aspects (**Figure 3.8**a-c, **Figure 3.3**) with a conventional chemically-crosslinked PVA hydrogel in which none of these structures existed (**Figure 3.3**e). Forming only low-density crystalline domains (**Figure 3.3**d) or aligned pore walls (**Figure 3.8**c) by conventional freezing-thaw method did not show tremendous enhancement in mechanical performance, while the formation of nanofibril networks (**Figure 3.8**b) led to a nearly two-order-of-magnitude increase in strength and a four-order-of-magnitude increase in toughness compared to the baseline. The addition of anisotropic microstructure (via directional freezing) further enhanced the strength and toughness, but the increase was less pronounced (**Figure 3.8**a). We can conclude that among the multiple mechanisms aforementioned that all play important roles, the effect of nanofibril network was particularly prominent for simultaneous high strength, toughness and stretchability.

The formed nanofibrils were not rigid but rather stretchable and deformed along with the hydrogel during stretching, as depicted in the SEM images of **Figure 3.8**d. The nanofibrils became increasingly aligned after stretching, as indicated by the stretch of SAXS pattern perpendicular to the loading direction (**Figure 3.8**d). The average nanofibril spacing decreased from ~350 nm to ~200 nm (**Figure 3.8**d, **Figure 3.9**) when the strain increased from 0% to 500%. These stretchable nanofibrils strengthened and toughened the hydrogel similar to rigid fiber reinforcements used in

composite hydrogels, yet they are stretchable to preserve the stretchability of the hydrogel, which
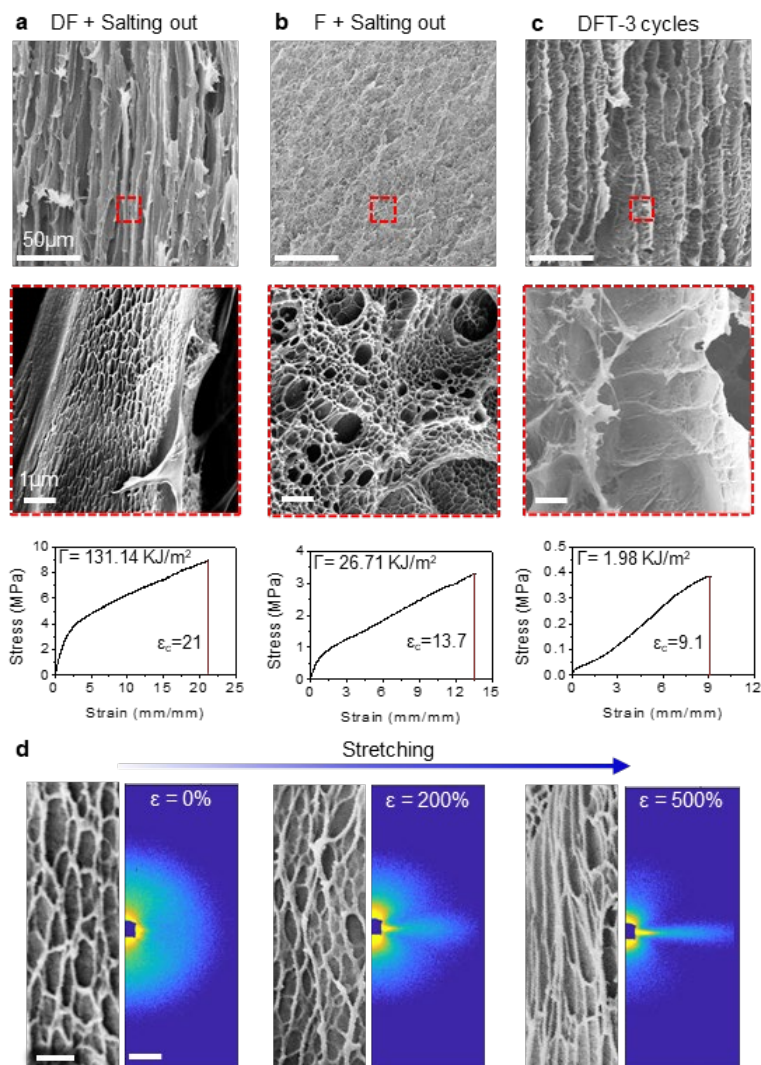
Figure 3.8 SEM images and mechanical properties of **a**, HA-5PVA hydrogel prepared by directional freezing and subsequent salting-out, **b**, F+S-5PVA hydrogel prepared by uniform freezing and subsequent salting-out (*i.e.*, non-directional compared to **a**), and **c**, DFT-5PVA hydrogel prepared by directional freezing and thawing for 3 cycles (*i.e.*, no salting-out compared to **a**). Scale bar is 50 μm for first row, and 1 μm for zoomed in SEM. **d**, Deformation of the mesh-like nanofibril network during stretching and the corresponding in-situ SAXS patterns. SEM scale

bar = 1 μm, SAXS scale bar = 0.025 Å^{-1}.
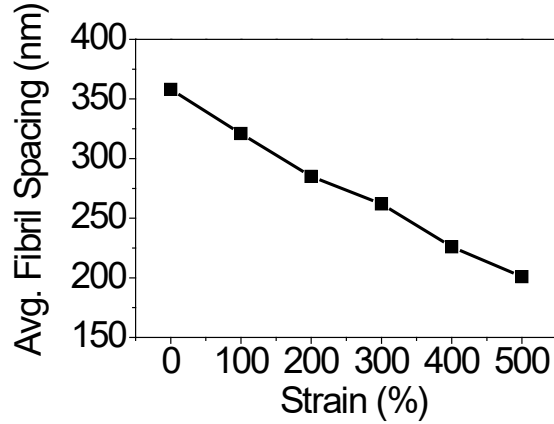
Figure 3.9 Plot of average inter-nano-fibril spacing calculated from SAXS patterns versus strain.

is the key reason for achieving simultaneous high strength, toughness and stretchability[19,26]. From a fracture mechanics perspective, first, the formation of continuously connected network facilitated the stress transfer between individual fibrils and prevented inter-fibril sliding, and thus, energy dissipation ahead of crack tip is not confined to the vicinity of the crack tip but rather the entire network (**Figure 3.10**). The connection of nanofibrils via a continuous network equivalently extend the length of these nanofibrils, and longer polymer fibers along the stress direction result in higher toughness[19]. Second, the fracture energy of amorphous hydrogel can be evaluated as[25,37]

$$\Gamma \propto U_f N_f,$$

in which the U_f is the energy to fracture a single polymer chain, and N_f is the number of polymer chains fractured. Due to the strong aggregation and crystalline domains in the nanofibrils, the energy to fracture the same number of crystalized polymer chains was much higher than that of the non-packed amorphous chains[38]. The entire bulk hydrogel is a continuous micron-scale

66

network comprising the above strong nanofibril networks, which largely accounted for its high strength, toughness, and stretchability.
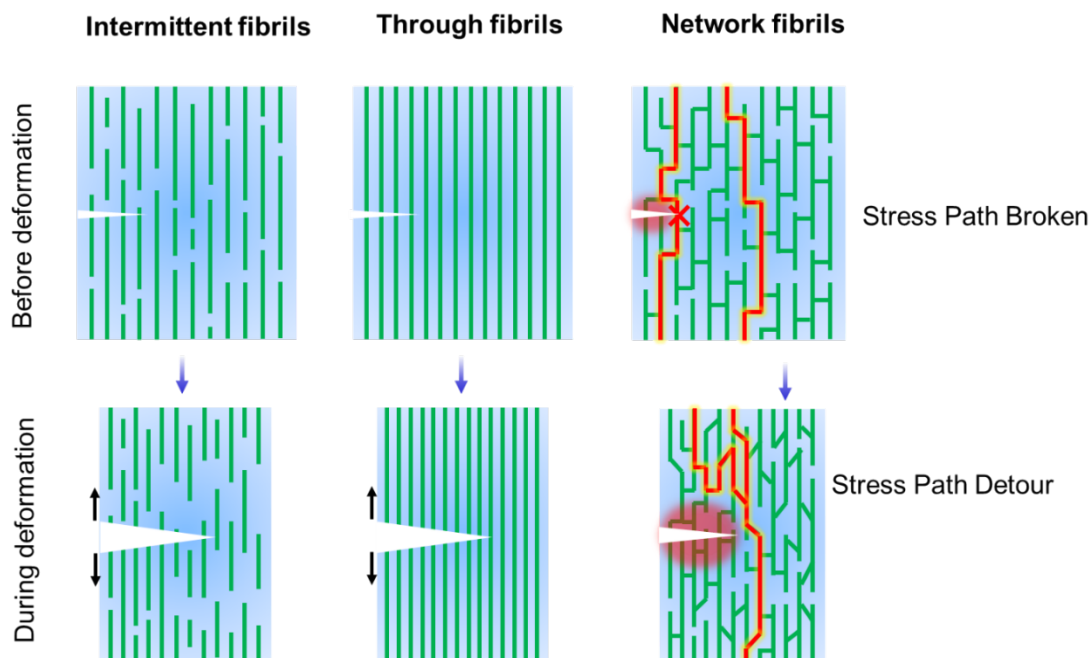
Figure 3.10 Illustration of nano-fibrils structure in anisotropic material. The nano-fibrils (green lines) have three assemblies of short fibrils (left), long fibrils (middle) and plaited networked fibrils (right) in the figure. The bottom row shows more compact fibril distance due to the reduction of free volume between fibrils after deformation.

3.4.4 Tunability and fatigue resistance

We varied the densities of the aligned micropore walls and nanofibrils by changing the initial PVA concentration from 2%-20% and reached ultimate stresses of 23.5 ± 2.7 MPa, 16.1 ± 1.8 MPa and 11.5 ± 1.4 MPa and corresponding ultimate strains of 1400 ± 210 %, 1800 ± 330 % and 2900 ± 450 % after 24 hours of coalescence process (**Figure 3.11**a, **Figure 3.12**). For hydrogels with

sufficient structural density and PVA concentration above 5%, the ultimate stress increased with PVA concentration, while the ultimate strain decreased with increasing PVA concentration, and the overall toughness increased with PVA concentration. Meanwhile, the fracture energy ranged from 131 ± 6 to 170 ± 8 KJ/m^2 as the concentration increased from 5 to 20 wt%, measured with a pre-cut crack perpendicular to the fibers. It should be noted that crack redirection was observed for the HA-5PVA and HA-10PVA hydrogels during the fracture energy measurements, where the significant blunting of crack size gives these hydrogels a flaw-insensitive property[11]. Therefore, the measured fracture energy becomes relevant to the sample size. Under the same sample size, the fracture energy of HA-5PVA was 5 and 65 times higher than the hydrogel with nanofibrils only (**Figure 3.8**b) and the hydrogel with aligned porous microstructure only (**Figure 3.8**c) respectively, in which the measured fracture energy is the true material property.

We further studied the reversibility and reusability of the HA-PVA hydrogels by conducting multiple loading-unloading tests (**Figure 3.11**b). Mechanical hysteresis was observed for all samples tested (**Figure 3.11**b), which indicated the presence of sacrificial bonds (primarily H-bonds here) that broke during deformation. The maximum stress increased with more stretching cycles due to improved alignment induced by stretching. The hysteresis area did not show obvious decrease over 10 cycles, which indicated that the sacrificial H-bonds responsible for energy dissipation were mostly reversible.
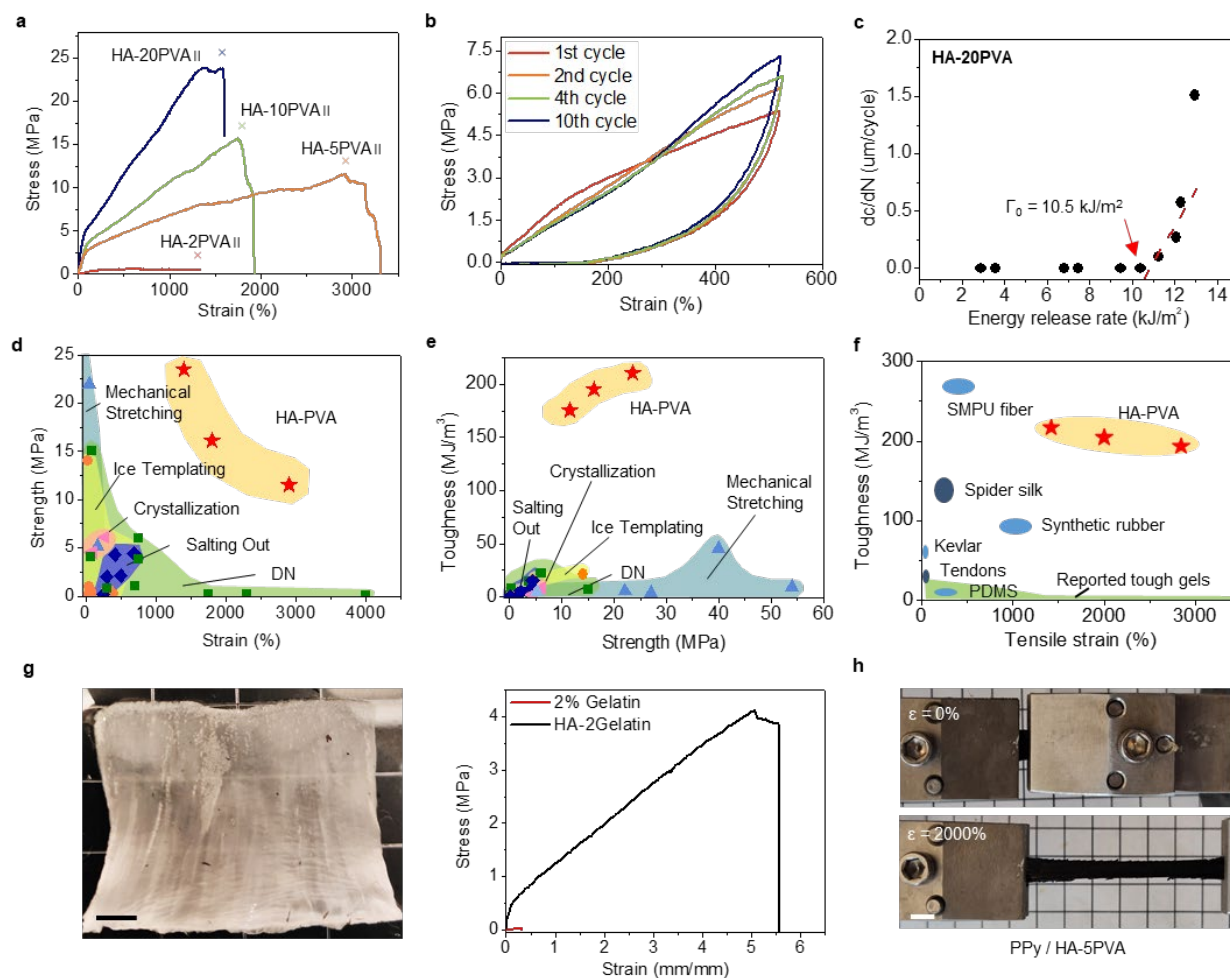
Figure 3.11 a, Stress-strain curves of HA-2PVA∥, 5PVA∥, 10PVA∥, and 20PVA∥ hydrogels after 24 hours of salting-out in 1.5M sodium citrate. **b**, Cyclic loading of HA-5PVA∥ hydrogel to 500% strain. **c**, Plot of crack propagation per loading cycle under increasing energy release rate. The energy release rate was controlled by corresponding maximum strain. **d-f**, Ashby diagrams of **d**, ultimate tensile strength vs. ultimate tensile strain, **e**, toughness vs. ultimate tensile strength, and **f**, toughness vs. ultimate tensile strain of HA-PVA hydrogels and other reported tough hydrogels and other tough materials. **g**, Photo of HA-2Gelatin hydrogel prepared by the same method as for HA-PVA and the stress-strain curve of HA-2Gelatin compared with regular 2% gelatin hydrogel. Scale

bar 5 mm. **h**, PPy-infiltrated HA-5PVA ‖ hydrogel being stretched. Scale bar 5mm.

2PVA   5PVA   10PVA   20PVA
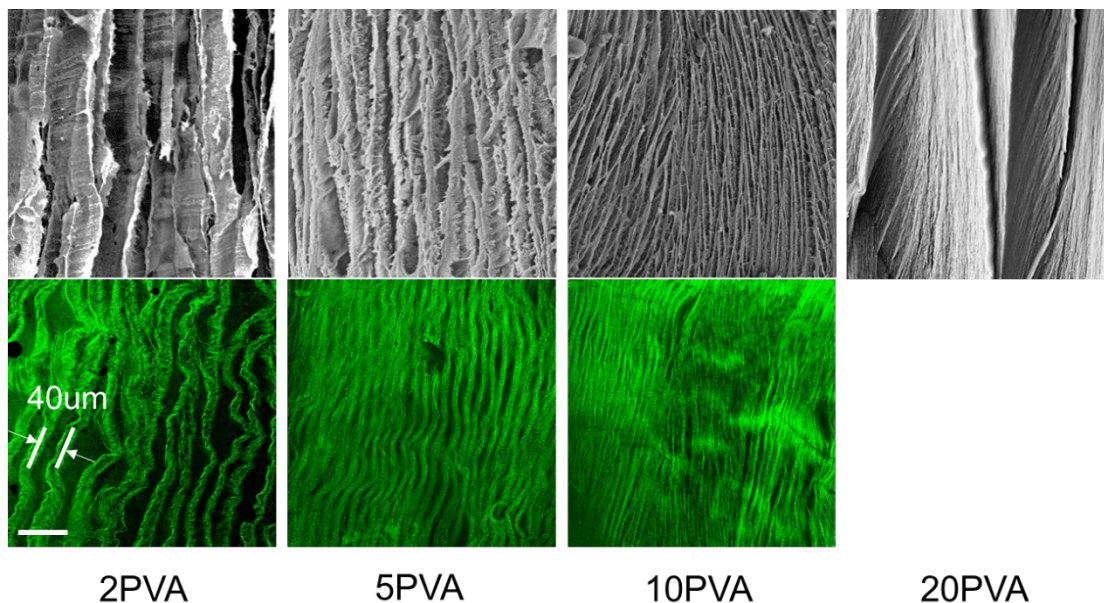
Figure 3.12 Images of HA-PVA hydrogels with various PVA concentration. SEM micrographs (top row) and corresponding confocal images (bottom row) of HA-2PVA (1st Column), HA-5PVA (2nd column), HA-10PVA (3rd column), and HA-20PVA (4th column). The confocal image for HA-20PVA was not present because the strong scattering cause by dense structures prevented us from obtaining a clear confocal image. Scale bar = 50 μm.

Fatigue resistance is another important criterion for structural hydrogels, whose limit is usually much lower than the fracture energy. To provide an accurate measurement, we used the relatively rigid HA-20PVA, in which crack redirection was less likely to occur. The HA-20PVA hydrogels showed excellent fatigue resistance with fatigue threshold of 10.5 ± 1.3 kJ/m^2 (**Figure 3.11**c, **Figure 3.13**), which is 8 times higher than the highest reported value for existing tough hydrogels[10,18]. No crack propagation or redirection was observed for over 30,000 cycles with such

a high energy release rate on a HA-20PVA hydrogel (**Figure 3.13**b). The highly fatigue-resistant HA-PVA hydrogels well utilize the high-energy crystalline domains and networks of fibers as mighty barriers that tendon and other robust natural materials employ.
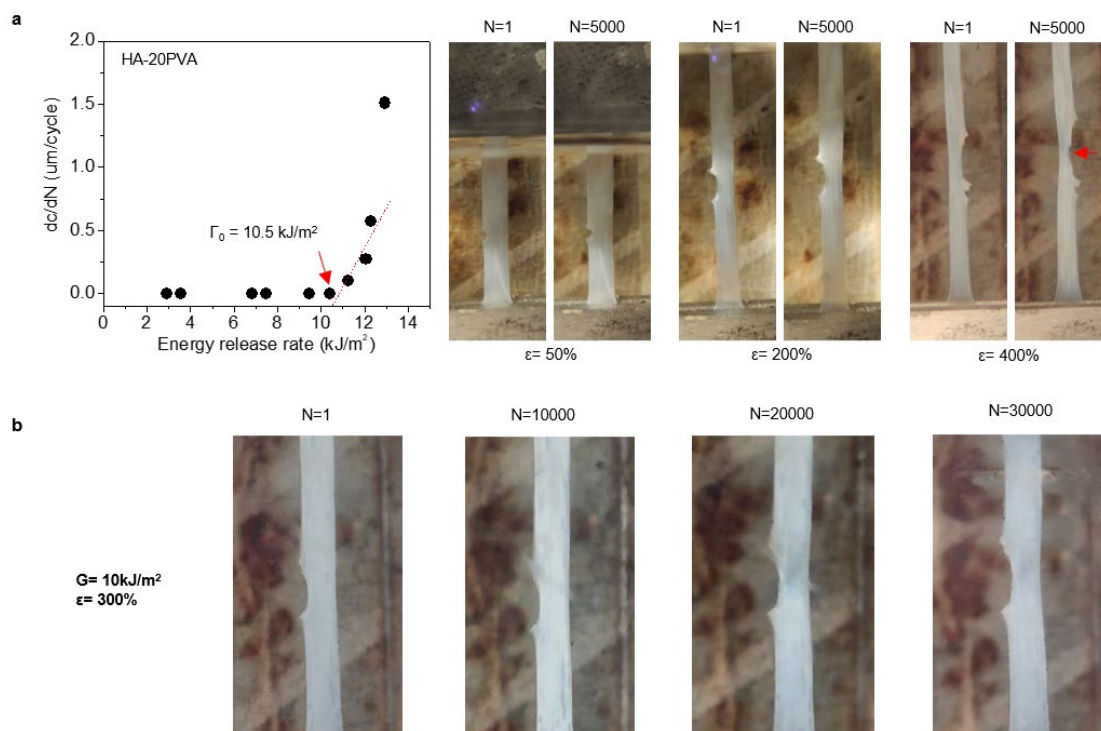
Figure 3.13 a, Fatigue threshold of HA-20PVA. When loading above the threshold energy release rate (ε= 400%), the crack slowly propagates. **b**, Validation of fatigue threshold with an energy release rate slightly lower than the fatigue threshold. No crack propagation or failure was observed for 30,000 loading cycles.

Overall, the HA-PVA hydrogels showed high ultimate stress and strain that well surpassed the values seen in many reported tough hydrogels (**Figure 3.11**d), and the overall toughness was increased by 4 to10^3 fold (**Figure 3.11**e). The HA-PVA hydrogels demonstrated excellent

toughness of 175 ± 9 to 210 ± 13 MJ/m^3 when there was no flaw, as the direct result of their combination of high strength and high ductility (**Figure 3.11**e). At over 70% water contents in these hydrogels (**Figure 3.14a**), the toughness values are well above water-free polymers like PDMS[39], Kevlar and synthetic rubber[40], even surpassing the toughness of natural tendon[41] and spider silk[42] (**Figure 3.11**f).
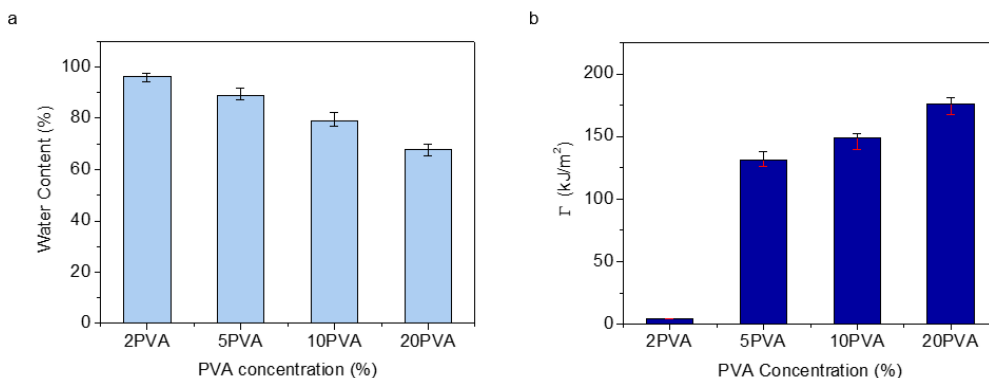
Figure 3.14 Water content and fracture energy of the HA-PVA hydrogels. **a,** Water content of HA-*x*PVA hydrogel, *x*=2, 5, 10, and 20. The error bar was obtained from 5 measured samples. **b,** Fracture energy of HA-*x*PVA hydrogel, *x*=2, 5, 10, and 20, measured by pure shear tests. The error bar was obtained from 5 measured samples.

3.4.5 Generality and customizability

Employing the freezing-assisted salting-out strategy, we also fabricated gelatin and alginate hydrogels with enhanced mechanical properties. Regular 2% gelatin hydrogels are weak and fragile, while the HA-2Gelatin hydrogel could be stretched to 4MPa and 550% strain, which led to an over 1000-time increase in toughness (from 0.0075 ± 0.0006 MJ/m^3 to 11.9 ± 1.7 MJ/m^3)

(**Figure 3.11**g). Likewise, the HA-5Alginate, which was a pure alginate hydrogel without calcium crosslinking, showed 1.1 ± 0.2 MPa ultimate strength and an over 20-time increase in toughness compared to calcium crosslinked alginate hydrogel (**Figure 3.15**). Building upon the combination of unprecedentedly high strength, stretchability and fatigue resistance of the HA-PVA hydrogels, we demonstrated their facile material customizability for additional properties (*e.g.*, electrical conductivity) to benefit the application of other fields. Here, by infiltrating the HA-PVA hydrogel with conducting polymer (*e.g.*, poly-pyrrole (PPy)), the hydrogel was functionalized with electrical conductivity without retarding its strength nor toughness (Figure 3.11h, Supplementary Fig. S13).
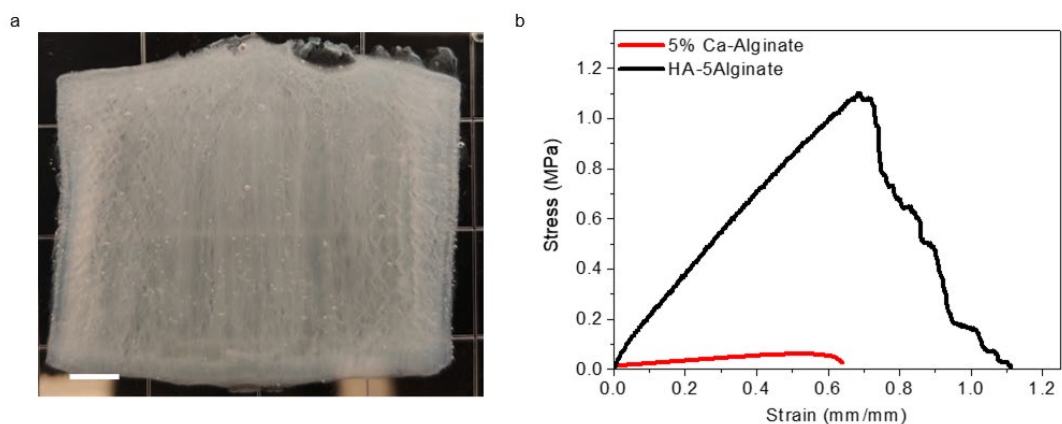
Figure 3.15 a, Picture of HA-5Alginate hydrogel. **b**, The tensile stress-strain curve of HA-5Alginate hydrogel compared to regular calcium-alginate hydrogel. Scale bar 5mm.

3.5 Conclusion

In this study, we have developed hierarchically structured hydrogels that combined high strength, toughness, stretchability and fatigue resistance, using a freezing‑assisted salting-out treatment.

Considering that the Hoffmeister effect exist for various polymers and solvent systems, we are convinced that the presented strategy is not restricted to the several presented systems. We foresee that originally weak hydrogels, with the help of the presented strategy, would gain expanded applicability in medical, robotics, energy, and additive manufacturing fields.

3.6 References

[1]   U. G. K. Wegst, H. Bai, E. Saiz, A. P. Tomsia, R. O. Ritchie, *Nat. Mater.* **2015**, *14*, 23.

[2]   G. Qu, Y. Li, Y. Yu, Y. Huang, W. Zhang, H. Zhang, Z. Liu, T. Kong, *Angew. Chemie - Int. Ed.* **2019**, *58*, 10951.

[3]   J.-Y. Sun, X. Zhao, W. R. K. Illeperuma, O. Chaudhuri, K. H. Oh, D. J. Mooney, J. J. Vlassak, Z. Suo, *Nature* **2012**, *489*, 133.

[4]   J. P. Gong, Y. Katsuyama, T. Kurokawa, Y. Osada, *Adv. Mater.* **2003**, *15*, 1155.

[5]   Q. Chen, L. Zhu, H. Chen, H. Yan, L. Huang, J. Yang, J. Zheng, *Adv. Funct. Mater.* **2015**, *25*, 1598.

[6]   X. Hu, M. Vatankhah-Varnoosfaderani, J. Zhou, Q. Li, S. S. Sheiko, *Adv. Mater.* **2015**, *27*, 6899.

[7]   P. Lin, S. Ma, X. Wang, F. Zhou, *Adv. Mater.* **2015**, *27*, 2054.

[8]   H. Qin, T. Zhang, N. Li, H. P. Cong, S. H. Yu, *Nat. Commun.* **2019**, *10*, 1.

[9]   Q. He, Y. Huang, S. Wang, *Adv. Funct. Mater.* **2018**, *28*, 1.

[10]   S. Lin, X. Liu, J. Liu, H. Yuk, H.-C. Loh, G. A. Parada, C. Settens, J. Song, A. Masic, G.

H. McKinley, X. Zhao, *Sci. Adv.* **2019**, *5*, eaau8528.

[11] R. Bai, J. Yang, X. P. Morelle, Z. Suo, *Macromol. Rapid Commun.* **2019**, *40*, 1.

[12] H. Zhang, I. Hussain, M. Brust, M. F. Butler, S. P. Rannard, A. I. Cooper, *Nat. Mater.* **2005**, *4*, 787.

[13] H. Zhang, *Ice Templating and Freeze-Drying for Porous Materials and Their Applications*; Wiley-VCH Verlag GmbH & Co. KGaA: Weinheim, Germany, 2018.

[14] K. Voges, C. Hübner, M. Vadalá, D. C. Lupascu, *Macromol. Mater. Eng.* **2018**, *303*, 1.

[15] C. Zhao, P. Zhang, J. Zhou, S. Qi, Y. Yamauchi, R. Shi, R. Fang, Y. Ishida, S. Wang, A. P. Tomsia, L. Jiang, M. Liu, *Nature* **2020**, *580*, 210.

[16] M. T. I. Mredha, H. H. Le, V. T. Tran, P. Trtik, J. Cui, I. Jeon, *Mater. Horizons* **2019**, *6*, 1504.

[17] M. T. I. Mredha, Y. Z. Guo, T. Nonoyama, T. Nakajima, T. Kurokawa, J. P. Gong, *Adv. Mater.* **2018**, *30*, 1.

[18] S. Lin, J. Liu, X. Liu, X. Zhao, *Proc. Natl. Acad. Sci. U. S. A.* **2019**, *116*, 10244.

[19] C. Xiang, Z. Wang, C. Yang, X. Yao, Y. Wang, Z. Suo, *Mater. Today* **2020**, *34*, 7.

[20] Y. Huang, D. R. King, T. L. Sun, T. Nonoyama, T. Kurokawa, T. Nakajima, J. P. Gong, *Adv. Funct. Mater.* **2017**, *27*, 1605350.

[21] W. R. K. Illeperuma, J. Y. Sun, Z. Suo, J. J. Vlassak, *Extrem. Mech. Lett.* **2014**, *1*, 90.

[22] S. Lin, C. Cao, Q. Wang, M. Gonzalez, J. E. Dolbow, X. Zhao, *Soft Matter* **2014**, *10*, 7519.

[23] D. R. King, T. Okumura, R. Takahashi, T. Kurokawa, J. P. Gong, *ACS Appl. Mater. Interfaces* **2019**, *11*, 35343.

[24] H. Fan, J. P. Gong, *Macromolecules* **2020**, acs. macromol.0c00238.

[25] X. Zhao, *Soft Matter* **2014**, *10*, 672.

[26] Z. Wang, C. Xiang, X. Yao, P. Le Floch, J. Mendez, Z. Suo, *Proc. Natl. Acad. Sci. U. S. A.* **2019**, *116*, 5967.

[27] S. Paţachia, C. Florea, C. Friedrich, Y. Thomann, *Express Polym. Lett.* **2009**, *3*, 320.

[28] M. Iwaseya, M. Watanabe, K. Yamaura, L. X. Dai, H. Noguchi, *J. Mater. Sci.* **2005**, *40*, 5695.

[29] Y. Zhang, P. S. Cremer, *Curr. Opin. Chem. Biol.* **2006**, *10*, 658.

[30] R. Long, C. Y. Hui, *Soft Matter* **2016**, *12*, 8069.

[31] Z. Jiang, *J. Appl. Crystallogr.* **2015**, *48*, 917.

[32] N. A. Peppas, E. W. Merrill, *J. Appl. Polym. Sci.* **1976**, *20*, 1457.

[33] S. Yoo, J. H. Kim, M. Shin, H. Park, J. H. Kim, S. Y. Lee, S. Park, *Sci. Adv.* **2015**, *1*, 1.

[34] P. Van De Witte, P. J. Dijkstra, J. W. A. Van Den Berg, J. Feijen, *J. Memb. Sci.* **1996**, *117*, 1.

[35] K. Dalnoki-Veress, J. A. Forrest, J. R. Stevens, J. R. Dutcher, *Phys. A Stat. Mech. its Appl.* **1997**, *239*, 87.

[36] F. Luo, T. L. Sun, T. Nakajima, T. Kurokawa, Y. Zhao, K. Sato, A. Bin Ihsan, X. Li, H. Guo, J. P. Gong, *Adv. Mater.* **2015**, *27*, 2722.

[37] G. J. Lake, A. G. Thomas, *Proc. R. Soc. London. Ser. A. Math. Phys. Sci.* **1967**, *300*, 108.

[38] J. Kirk, *Compos. Struct.* **1984**, *2*, 373.

[39] I. D. Johnston, D. K. McCluskey, C. K. L. Tan, M. C. Tracey, *J. Micromechanics Microengineering* **2014**, *24*, 035017.

[40] L. A. Wood, *Rubber Chem. Technol.* **1978**, *51*, 840.

[41] M. Javidi, C. P. McGowan, N. R. Schiele, D. C. Lin, *Sci. Rep.* **2019**, *9*, 1.

[42] D. Ebrahimi, O. Tokareva, N. G. Rim, J. Y. Wong, D. L. Kaplan, M. J. Buehler, *ACS Biomater. Sci. Eng.* **2015**, *1*, 864.

4. Tough hydrogel reinforcement coating via Freezing Assisted Salting Out

4.1 Introduction

With the understanding of PVA hydrogel formation via freezing assisted salting out method and through evaluation of the structure – mechanical property relationship, it is clear that the PVA hydrogels fabricated by the proposed method can replace the structural function of current hydrogels in various application with significantly reduced dimensionality. Such reduction in size or thickness could significantly benefit mass transport process. Therefore, it is promising to explore the application of PVA hydrogels prepared by freezing assisted salting out method as coatings and binder materials, especially for energy storage purposes, where mechanical robustness and high mass diffusion are both demanded.

Supercapacitors are an important class of energy storage device that are widely used for portable electronics, electric vehicles, and power plants[1,2]. Compared with metal-ion batteries, supercapacitors are advantageous in their high-power density, fast charging and discharging, and fire safety[3]. Traditional supercapacitors use liquid electrolytes, which make them bulky and difficult to seal. In recent years, supercapacitors can be readily fabricated using gel-electrolyte to obtain all-solid-state supercapacitors, adding light weight and simple form-factor to their advantages[4–6].

Wearable and implantable electronics that are complaint and seamlessly function alongside a moving body have been actively developed for applications like artificial skin[7], morphing sensors[8], biomedical robots[9,10], and human-machine interfacing[11]. For a prolonged period of untethered functioning of these compliant electronics, energy storage devices like supercapacitors with high energy density, fast charging speed and similar compliance are desired[12,13]. For this purpose, various polymeric materials have been used for improving the device flexibility and stretchability. For instance, hydrogels and aerogels are common polymeric scaffold materials for fabrication of supercapacitors[5,14]. Electrodes modified from hydrogel scaffolds generally retain the original material flexibility. With   the intrinsic porous micro- and nanostructures of hydrogels, which yield high surface area and excellent permeability to ions, large capacitance and high rate capability is principally achievable[15,16]. The non-conductive elastic hydrogel scaffolds are often functionalized with conducting polymers like poly(pyrrole), poly(aniline), PEDOT: PSS, and graphene for electrical conductivity[17], using methods like infiltration by liquid-/vapor-phase and in-situ polymerization[18–27]. However, the mass loading of conducting polymers by infiltration methods is relatively low (< 10 mg/cm^2), as monomers are barricaded by the semi-continuous pores to diffuse into the hydrogel[18–22]. Therefore, only thin hydrogel electrodes are best compatible with this method to gain sufficient conductivity and electro-active material. The alternative in-situ polymerization method can yield higher mass loadings[23–27]; however in particular cases, the solubility cap limits the maximum content of conducting polymers (*e.g.*, pyrrole in water, PEDOT:PSS in water) in the aqueous solvent to stably co-exist with the hydrogel

monomers and the structure may vary significantly upon slight changes in the composition ratio[23]. "All-conducting-polymer" hydrogel electrode have also been fabricated to show both flexibility and good conductivity[28–32]. However, these polymers may face embrittlement under stretching (strain < 10%) and direct polymerization of the less soluble conducting polymers produces stacked spherical aggregates with poor electrical interconnection[27]. Successful methods involve using 2D conducting fillers[31] that are intrinsically robust and do not aggregate into spheres, synthesizing 1D conducting polymer fibers using special crosslinkers [30] and adding plasticizer agents[33].

On the other hand, while thin electrodes are equally functional, thick electrodes offer the same capacitance with simpler device assembly and less usage of non-active materials. To increase the electrode thickness without reducing device efficiency and power density, low tortuosity electrodes, with aligned porous (anisotropic wood-like microstructure, low tortuosity in one direction) or even open porous structures (isotropic sponge-like microstructure, low tortuosity in all directions), are desired[34–39]. Strong macro-open-porous conducting foam materials have been used for fabricating supercapacitors with high thickness and low tortuosity. These macro-open-porous foams are fabricated by depositing conductive or electro-active materials on commercial metal foams or metallic textiles knitted by metal wires[40–45]. While excellent in mechanical stability, the low surface area will limit the mass loading, and thus the overall capacitance of the macro-open-porous electrodes. Alternatively, many micro-open-porous conductive hydrogels/aerogels showed both high surface area and low tortuosity. However, with microstructures of thin, brittle and sparse

interconnects, they are fragile due to the insufficient linkage between segments, and thus, are prone to mechanical damages during stretching. Therefore, creating robust micro-open-porous conducting foams would be advantageous in improving both the mechanical stability and power density of supercapacitors while maintaining high capacitance.

4.2 Proposed Method

Here we present a straightforward strategy for fabricating robust, low tortuosity electrodes with ultra-high mass loading, by compositing a superficial layer of tough hydrogel as reinforcement binders to the originally fragile micro-open-porous conducting polymer electrodes, termed as tough-gel reinforced open-porous foam (TROF) in the following (**Figure 4.1**). We specifically selected poly(vinyl alcohol) (PVA) to construct the tough hydrogel layer due to its excellent mechanical properties[46–48], ease of physical crosslinking[49] and compositional simplicity. The ultra-tough hydrogel significantly reinforced the electrode even with a small amount of addition (0.1 mL cm^{-2}), which improved electrode flexibility, stretchability and toughness while maintaining the open porous structure for fast diffusion. The presented strategy would greatly benefit the design and fabrication of high-performance supercapacitors for energy storage in flexible and wearable electronics.
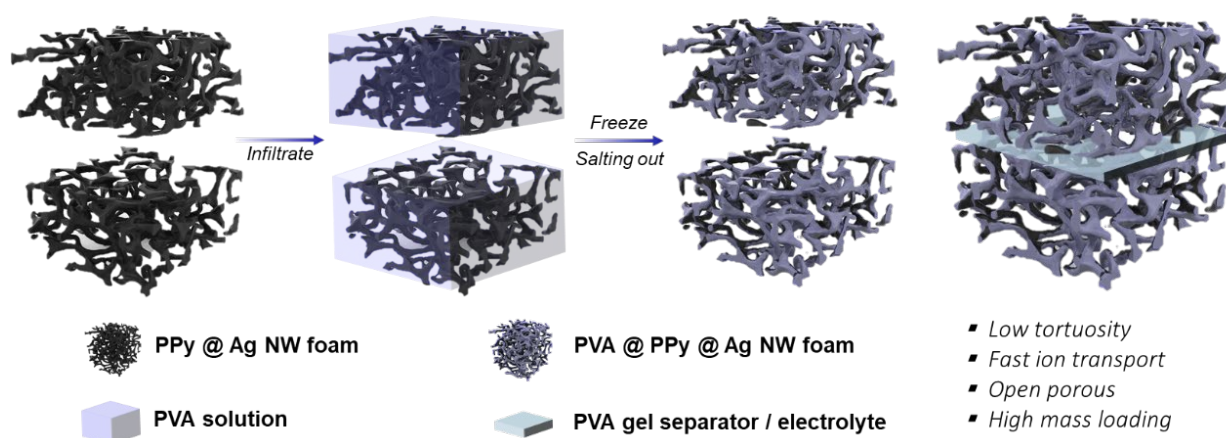
Figure 4.1 Schematic of the tough-hydrogel reinforced open-porous foam (TROF) electrode.

4.3 Experimental and Characterization Section

4.3.1 Materials

Silver nitrate (AgNO$_3$, Fisher Scientific, 99%), ethylene glycol (Fisher Scientific), poly (vinyl pyridine) (PVP, M.W. 360 000, Fisher Scientific), pyrrole (reagent grade, 98%, Sigma Aldrich), aniline (98%, Sigma Aldrich), graphene oxide (4 mg/mL, Sigma Aldrich), hydroiodic acid (HI, 55%, Sigma Aldrich), ammonia persulfate (APS, Sigma Aldrich), poly (vinyl alcohol) (PVA, M.W. = 89,000 – 98,000, 99% hydrolyzed, Sigma Aldrich), iron(III) chloride (FeCl$_3$, Sigma Aldrich) were all used as received.

4.3.2 Fabrication of Silver Nanowires:

A facile polyol synthesis procedure of Ag NWs was used[50]. Briefly, 1 g PVP was added to 100 mL ethylene glycol and completely dissolved by stirring under room temperature. Subsequently,

1 g AgNO$_3$ was added to the solution and completely dissolved. Afterwards, 10 mL of FeCl$_3$ (1 mM in ethylene glycol) solution was added to the mixture and stirred for 1 minute. The mixture was immediately transferred to an oil bath preheated to 110 ˚C and left still to grow Ag NWs for 12 hours. The obtained Ag NWs was then centrifuged and washed by ethanol for 3 times and finally dispersed in ethanol for later use (**Figure 4.2**). The final Ag NWs dispersion has a concentration of ~ 3mg / mL measured by weighing air dried residue of the solution.
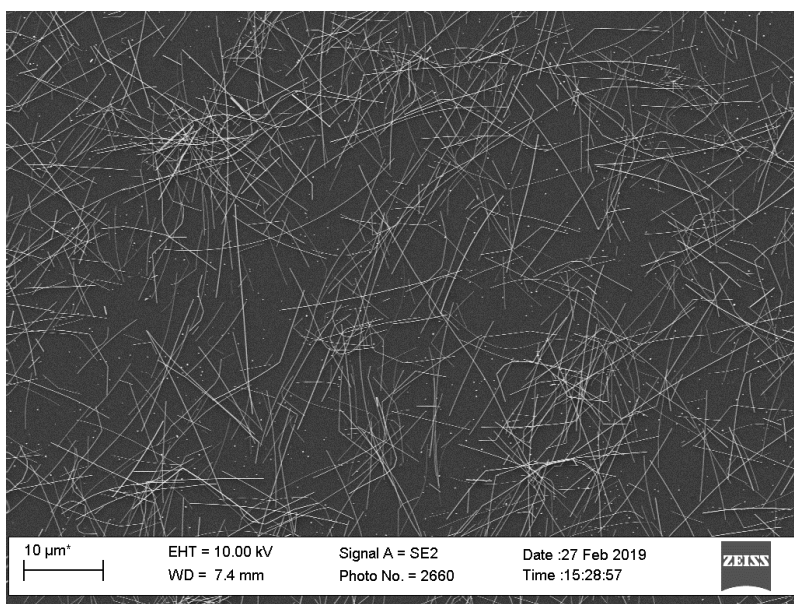
Figure 4.2 SEM image of the synthesiszed silver nanowire (Ag NW). The average length of the Ag NW is 21.73 μm and the diameter of the Ag NW is ~ 60nm.

4.3.3 Fabrication of PPy@AgNWs Foam

The PPy@Ag NWs foam was fabricated by mixing two parts of a precursor together. Precursor part A: 2x v% pyrrole dissolved in 7.5 mL of Ag NWs solution (solvent: ethanol). Precursor part B: 1.17x wt% FeCl$_3$ dissolved in 7.5 mL water (Fe^{3+} and pyrrole molar ratio was adjusted to be

1:4, x = 2.5, 5, 10, 25). The two parts of the precursor was cooled in a -20˚C freezer for 10 minutes before mixing together. After mixing the precursor parts A and B together, the final mixture containing x v% pyrrole and y wt% FeCl$_3$ was vortexed for 10 seconds and poured into a petri-dish and stored in a 4˚C fridge for 12 hours. Finally, the resulting gel-like product was washed with ethanol to removed excess pyrrole monomer and immersed in DI water for 24 hours to remove other non-reacted chemicals. The washed sample was then freeze-dried using a Labconco Freezone freeze-dryer to obtain the micro-open-porous PPy@Ag NWs foam.

4.3.4 Fabrication of PANi@Ag NWs and rGO Foam

For synthesizing micro-open-porous PANi@Ag NWs foam, the fabrication procedure mostly follows the case of PPy @Ag NWs foam described in the previous section with a few modifications. Precursor A was modified to have 2x v% aniline dissolved in 7.5 mL of Ag NWs solution (solvent: water). Precursor B was modified to have 2y wt% APS dissolved in 7.5 mL water (APS and aniline ratio was also 1:4). For synthesizing micro-open-porous rGO foam, aqueous graphene oxide solution (10 mg/mL) was directly freeze-dried and then reduced using a 2 wt% HI solution.

4.3.5 Fabrication of TROF

2-10 wt% PVA solution was prepared by dissolving PVA in DI water under heating and stirring to achieve a homogenous solution. The PVA solution was added dropwise into the micro-open-porous PPy@Ag NWs foam using a pipet. The volume of the added PVA solution was fixed at 0.1 mL/cm^2.

The PVA infiltrated foam was left still for homogenization for 10 minutes and then put in a -20˚C freezer for 1 hour until completely frozen. The frozen sample was then cast into 20 wt% Li_2SO_4 solution for 30 minutes for salting out toughening to obtain the TROF electrode.

4.3.6 Assembly of Supercapacitor

The surface of the TROF in contact with the current collector was sanded slightly to reduce the resistance between the electrode and carbon cloth current collector. Then, a gel separator film was fabricated by freezing 5 wt% PVA solution followed by subsequent sating out in a 20 wt% Li_2SO_4 solution for 30 minutes for physically crosslinking the PVA. The gel separator film was sandwiched between two TROF electrodes and pressed together. The assembled supercapacitor was then frozen and salted out for another cycle in 20 wt% Li_2SO_4 + 5 wt% H_2SO_4 electrolyte solution to adhere the three layers together.

4.3.7 Electrochemical Characterization

The electrochemical properties were characterized by a CHI660E electrochemical workstation using a two-electrode setup. Two pieces of carbon cloth were used as current collectors in contact with the TROF electrodes.

4.3.8 Mechanical Characterization

The mechanical property characterization and stretchable supercapacitor study was carried out

using a Univert mechanical tester with 450 mN loading cell.

4.3.9 Materials Characterization

The SEM images of samples were taken using a Supra 40VP scanning electron microscope.

4.4 Result and Discussion

4.4.1 System Design

Figure 4.1 illustrates the design concept and fabrication procedure of the tough-gel reinforced open-porous foam (TROF) electrode. Briefly, the initial open-porous conductive polymer foam was fabricated by the coaxial growth of conducting polymers on silver nanowires (Ag NWs, **Figure 4.2**) in a mixture solution containing silver nanowires, pyrrole monomers, and oxidants. Similar reactions can be realized for various conducting polymers via a simple red-ox reaction[38,39,51,52]. The silver nanowires served as both a scaffold to guide the growth of poly(pyrrole) (PPy) into an open-porous network (**Figure 4.3**) and a highly conductive pathway to improve electrical transport in the thick electrode.
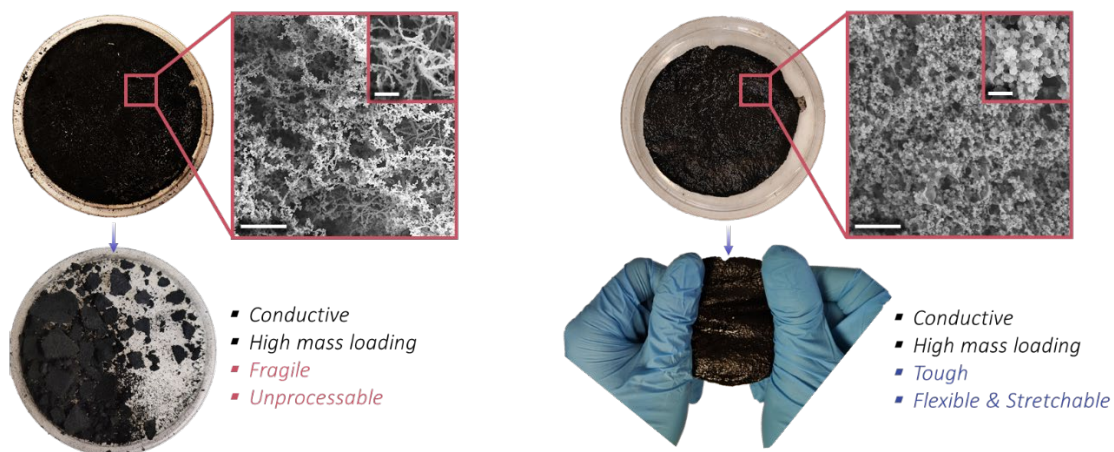
Figure 4.3 Left, PPy@Ag NWs foam without tough hydrogel reinforcement. The macroscopic image shows a black and open porous material that shatters easily under mechanical loading. The scanning electron microscopy (SEM) image shows the microstructure of the foam. Scale bar 50 µm, inset scale bar 5 µm. Right, PPy@Ag NWs foam with tough hydrogel reinforcement. The macroscopic image shows a black tough hydrogel reinforced PPy@Ag NWs foam composite that shows stretchability and mechanical robustness. The SEM image shows the microstructure of TROF. SEM scale bar 50 µm, inset SEM scale bar 5 µm, the diameter of petri dish is around 10cm.

The mass loading of active materials was tunable by adjusting the concentration of monomers (**Figure 4.4**). Typically, the mass of PPy@Ag NWs foam is 32.2 mg cm^{-2} for samples made from precursor containing 10 v% pyrrole. The open-porous conductive foam obtained after freeze drying was mechanically weak and difficult to process as supercapacitor electrodes (**Figure 4.3**). The SEM image showed the foam structure of sparely interconnected coaxial PPy@Ag NWs (**Figure 4.3**). With an increase of pyrrole concentration from 2.5 v% to 25 v% in the precursor

mixture, the shell poly(pyrrole) layer could exhibit morphology from smooth, to sphere decorated, and then to spherical agglomerate microstructures (**Figure 4.4**).
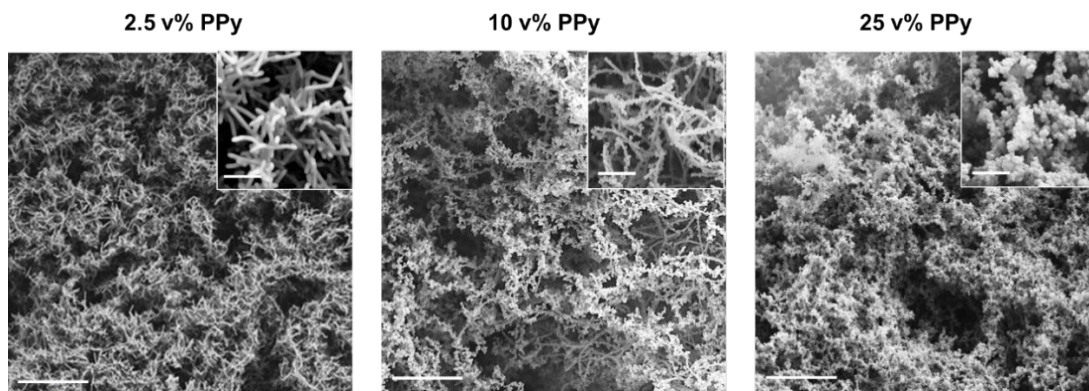
Figure 4.4 SEM images of PPy@Ag NW foam synthesized with different concentration of pyrrole. The content of silver nanowire and FeCl3 remained unchanged. SEM scale bar 50 μm, inset SEM scale bar 5 μm.

The final TROF was obtained by infiltrating a tough PVA hydrogel coating on the periphery of the open-porous conducting networks. Benefiting from the low tortuous nature of the initial conducting polymer foam, the liquid PVA precursor (2-10 wt%) was quickly absorbed and spread inside the foams, which indicated that the penetration depth was much larger than the thickness of the fabricated foam (**Figure 4.5**). After freezing and salting out in a 20 wt% lithium sulfate (Li_2SO_4) solution (**Figure 4.1**), a tough and conducting electrode was obtained (**Figure 4.3**). Li_2SO_4 was specifically chosen due to the high diffusivity of Li^+ ions and the good toughening effect of SO_4^{2-} ions on PVA hydrogels[53]. We have also tested the conductivity of the electrode throughout the fabrication process to ensure that the TROF electrode maintains a good conductivity (**Figure 4.6**).

It was confirmed that the final TROF electrode has a conductivity comparable to the pristine foam.

2.5 v% PPy   **5 v% PPy**

10 v% PPy   **25 v% PPy**
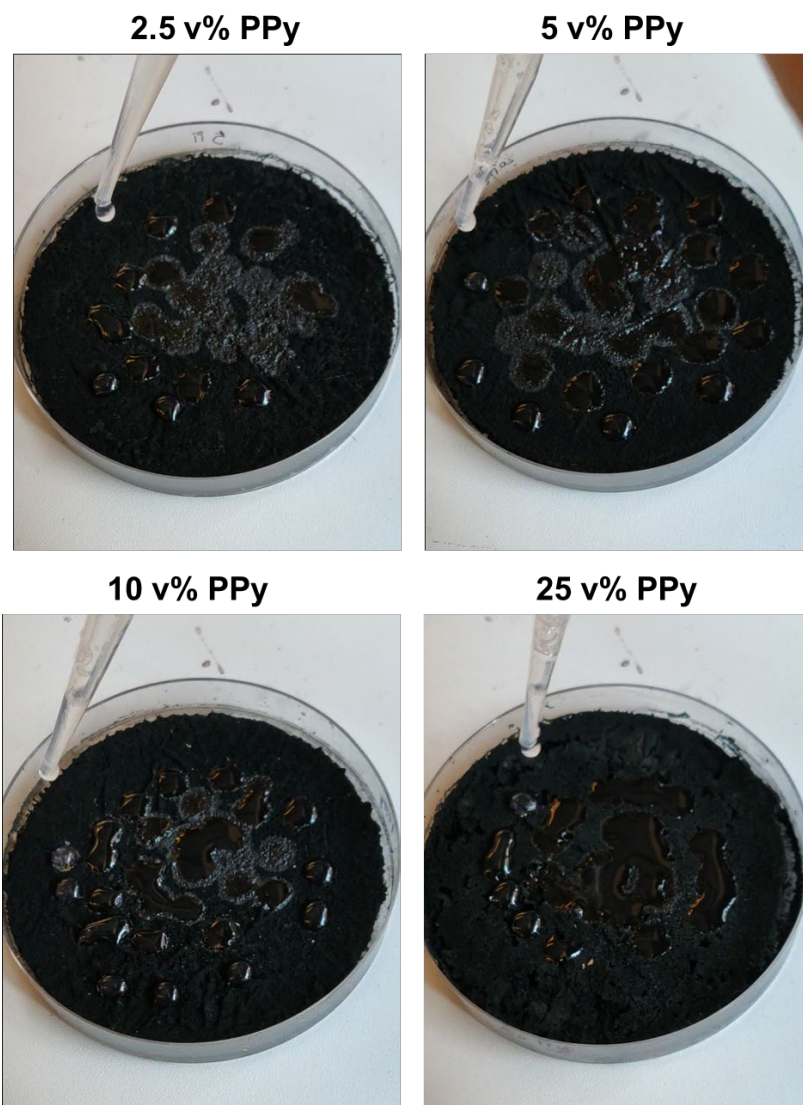
Figure 4.5 Images of PVA precursor infiltration into PPy@Ag NW foam synthesized with different

concentration of pyrrole. The infiltration becomes slower for foams with higher concentration of

pyrrole, indicating the increase in hydrophobicity. Diameter of petri dish is around 10cm.
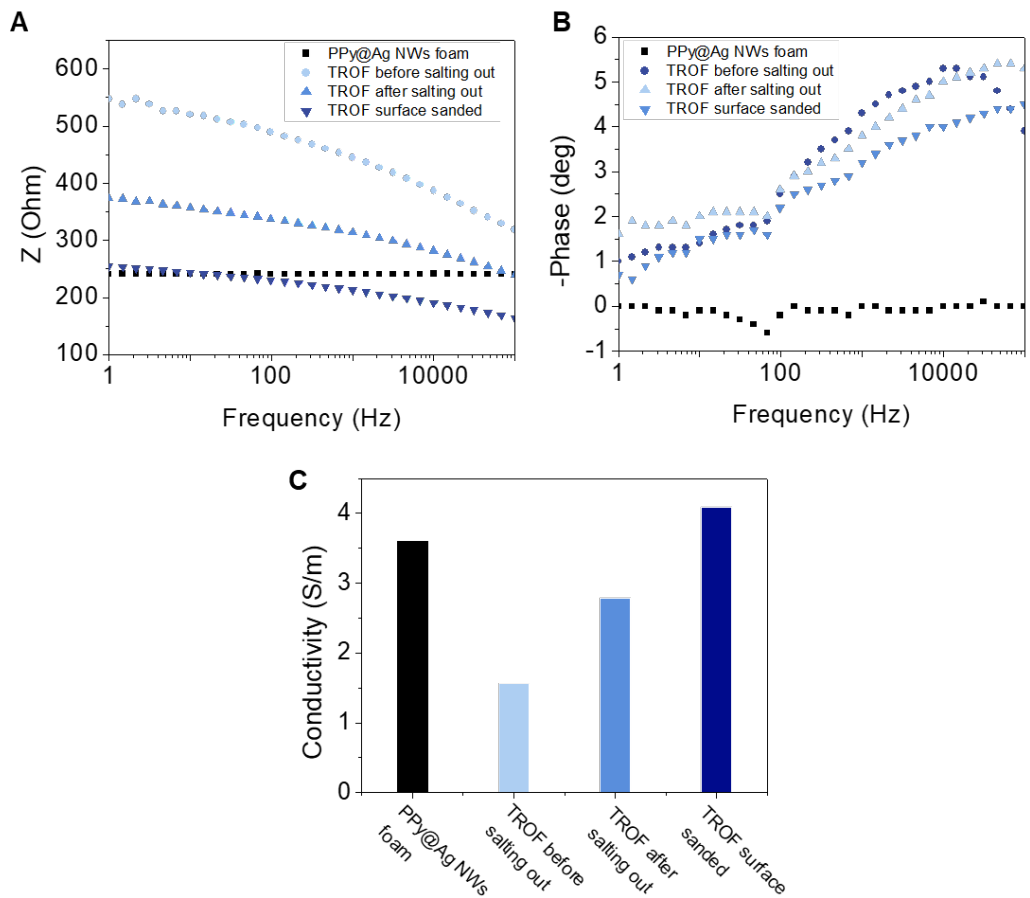
Figure 4.6 Resistance vs. frequency (A) and phase vs. frequency (B) plots of the supercapacitor electrode at different stages in the fabrication process. C shows the conductivity of the electrodes at their respective stages in the fabrication process. The results were measured using a 4-electrode setup on samples made from10 v% PPy@Ag NWs foam.

Mechanistically, the infiltrated PVA solution spread inside the open porous foam following the contour of the conductive network due to surface tension. During freezing, the formation of ice crystals expelled the PVA polymers chains to the ice grain boundaries and induces the aggregation between PVA polymer chains[49,54,55]. Note that usually one-time freezing is insufficient to induce

a strong aggregation between the PVA polymer chains, and only weak H-bond interaction was established during the freezing step[56]. Upon immersion into the high concentration lithium sulfate solution, in which the sulfate ions served as an efficient salting out agent by Hofmeister effect, the PVA polymer chains phase separated from the solution and formed strong crystalline domains by hydrogen bonding[53,55,57–59]. The densely aggregated PVA polymer chains lead to the formation of an ultra-strong and tough hydrogel (**Figure 4.7**)[53,55]. The toughening effect is strongly affected by the concentration of the infiltrated PVA solution. With the increase of PVA concentration from 2 wt% to 10 wt%, the TROF electrode showed both increase in ultimate strain and stress by 200% and 1600% respectively (**Figure 4.8A**).
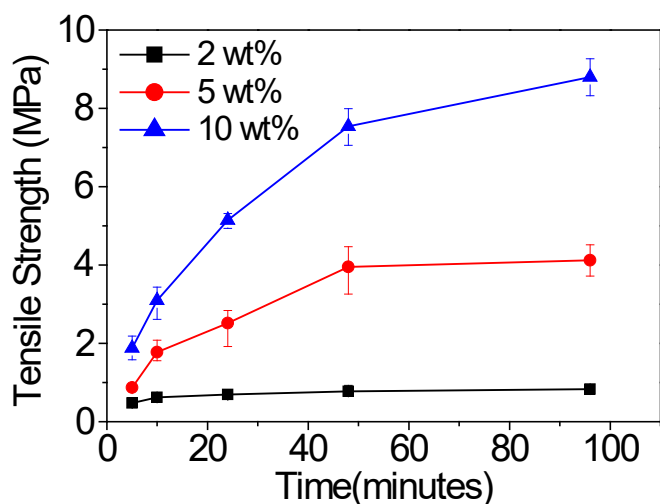
Figure 4.7 Ultimate tensile strength of PVA hydrogels films (made with 2-10 wt% PVA precursor) films prepared by freezing and salting out in 20 wt% Li_2SO_4 solution for various times. The results indicated that SO_4^{2-} has a salting out ability and produced an ultra-strong and tough PVA hydrogel.
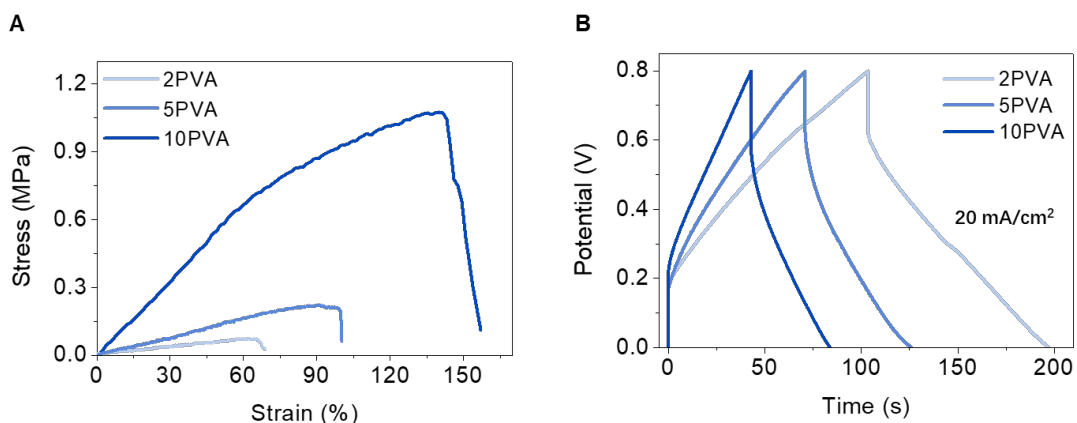
Figure 4.8 A) Stress-strain curves of TROF electrodes fabricated with different concentrations of PVA solutions. B) GCD curves of supercapacitors fabricated using TROF electrodes with different concentrations of PVA solution. The 10 v% PPy@Ag NWs foam was used, and a 10 mL PVA solution was infiltrated into each dish of foam.

The ultra-tough PVA hydrogel reinforcement prepared by the freezing and salting out method allowed for significant reinforcement of the originally weak conducting polymer with only a thin coating of the tough hydrogel. The coating helped reduce diffusion barrier of ions to and from the encapsulated conductive network underneath and also maintain the desired open-porous microstructure (**Figure 4.3**). Finally, an all-solid-state supercapacitor was fabricated by sandwiching a PVA hydrogel membrane between two pieces of 1.5 mm thick TROF electrode, the three layers were joint together by another cycle of freezing and salting out in a 20 wt% Li_2SO_4 + 5 wt% H_2SO_4 electrolyte solution.

4.4.2 Electrochemical Properties of TROF supercapacitor

We first evaluated the electrochemical performance of the TROF electrodes in a two-electrode system using the fabricated all-solid-state supercapacitor device. Variation in the pyrrole concentration from 2.5 v% to 25 v% did not lead to significant change in the capacitance, as the ultimate surface area is mostly determined by the amount of Ag NWs; however, higher concentration of pyrrole yielded a lower internal resistance drop (**Figure 4.8**) but higher hydrophobicity (**Figure 4.5**). To ensure a balance between good conductivity, infiltration ability and toughness, we used 10 v% pyrrole precursors and 10 wt% PVA infiltration solutions for the majority of the experiments. **Figure 4.9**B shows the typical CV curves of the TROF supercapacitor at various scan rates of 5-50 mV s^{-1}, the curves are all symmetric and has a near rectangular shapes at a scan rate below 10 mV s^{-1}, indicating a good capacitive behavior of the electrode. The Nyquist plots of the TROF supercapacitor showed a low equivalent series resistance (ESR) of 7.3 Ω cm^2 and charge transfer resistance (R$_{CT}$) of 1.2 Ω cm^2, which benefited from the interconnected coaxial poly(pyrrole) @ Ag NWs conductive network and the open-porous microstructure that facilitated the ion transportation (**Figure 4.9**C). The galvanostatic charge-discharge (GCD) curves measured with current density of 1-30 mA cm^{-2} within an operation window of 0-0.8 V all showed nearly triangular shapes, indicating the formation of efficient electrochemical double layer inside the TROF electrode and high coulomb efficiency (**Figure 4.9**D). It should be noted that while a small amount of pseudo-capacitance (< 1%) may be contributed by the redox reaction of Ag NWs, it is negligible compared to that of the TROF electrode (**Figure 4.10**).   Remarkably, the TROF device exhibited an ultra-high areal capacitance of 5.25 F cm^{-2} (34.96 F/g, normalized against the device's

total weight) at 1 mA cm^{-2} charging and discharging rate (**Figure 4.9**E). Even at a high current

density of 20 mA cm^{-2}, the areal capacitance was maintained at a high value of 1.8 F cm^{-2}, which

indicated an excellent rate capability compared to most reported all-solid-state

supercapacitors[20,27,29,32,37].
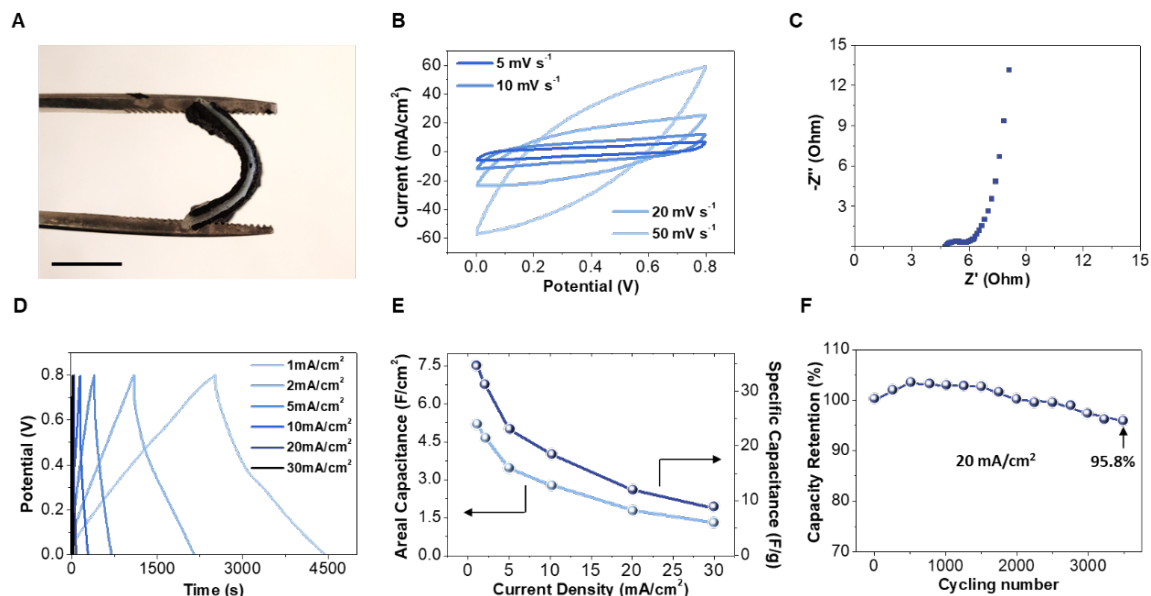
Figure 4.9 A) Image of the TROF supercapacitor fabricated by sandwiching two TROF electrode

and one PVA hydrogel separator. Scale bar 5mm. B) CV curves of TROF supercapacitor with

scanning rate of 10-100 mV S^{-1}, device area 1 cm^2. C) Nyquist plot of TROF supercapacitor at

frequencies from 0.1M to 0.01 Hz. D) GCD curves of TROF supercapacitor at current density of

1-30 mA cm^{-2}. E) Areal and specific capacitance of TROF supercapacitor at current density of 1-

20 mA cm^{-2}. F) Capacitance retention during 3500 GCD cycles.

Surprisingly, with partial sacrifice of the mechanical robustness by infiltrating more dilute PVA

solutions (2 wt% PVA), the areal capacitance of the device measured at the same high current density of 20 mA cm^{-2} increased for > 2 times to 3.9 F cm^{-2} (**Figure 4.8**B). The capacitance values of the TROF are especially high, owing to the high mass loading of the electrodes (~ 77 mg cm^{-2}). Such a high capacitance was maintained at 95.8% after 3500 GCD cycles even when operating under a high current density of 20 mA cm^{-2} (**Figure 4.9**F). The excellent cycling performance and stability were attributed to the open-porous structure that allowed fast ion-diffusion and the tough hydrogel reinforcement binder that maintained the structure integrity throughout the long-term GCD cycles. The capacitance reduction occurred at a much faster rate without the tough hydrogel reinforcement layer (**Figure 4.11**), which indicated that the tough shell effectively helped maintain electrochemical stability of the electrode.
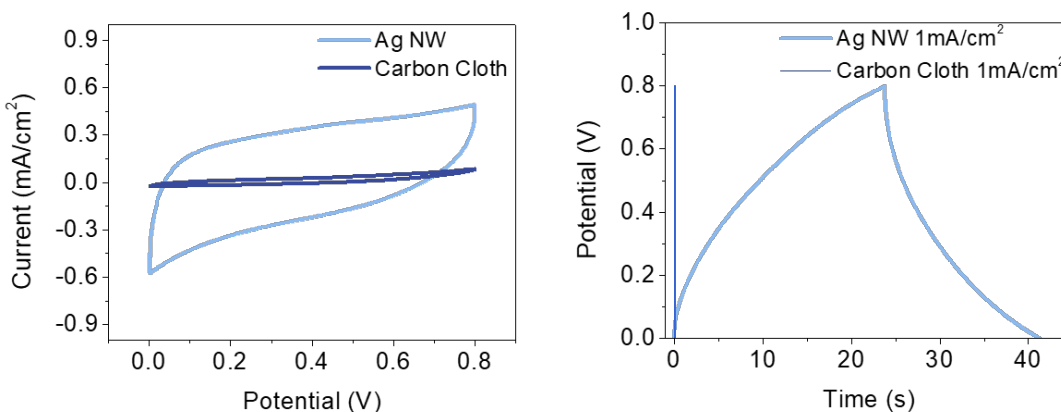
Figure 4.10 CV and GCD curves of supercapacitor made with carbon cloth as electrode and an Ag NWs foam as the electrode. The result indicates that the Ag NWs may contribute a negligible amount of pseudo capacitance to the over-all TROF supercapacitor capacitance.
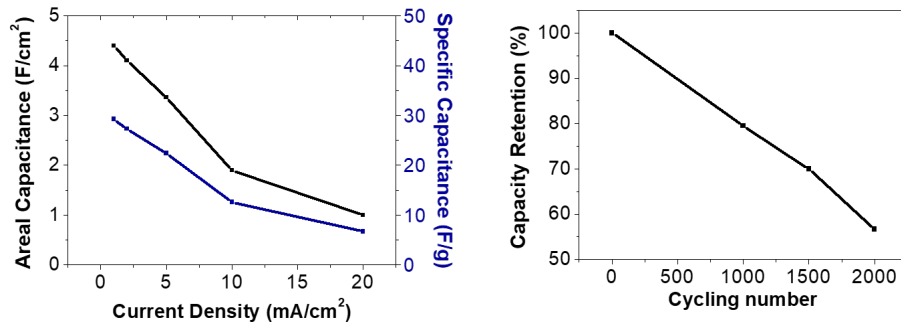
Figure 4.11. The left image shows the areal and specific capacitance of 10 v% PPy@Ag NW foam without tough PVA hydrogel reinforcement. The right image shows the capacitance retention during 2000 GCD cycles of the same supercapacitor.

4.4.3 Mechanical Robustness of TROF device

Benefiting from the ultra-tough hydrogel reinforcement binder, the TROF electrode infiltrated with 10 wt% PVA and after salting out exhibited a high ultimate strength of ~ 1MPa and ultimate strain of ~ 140%, which yields a toughness of 800 kJ m^{-3} and a fracture energy of ~ 1000 J m^{-2} (**Figure 4.12A**).
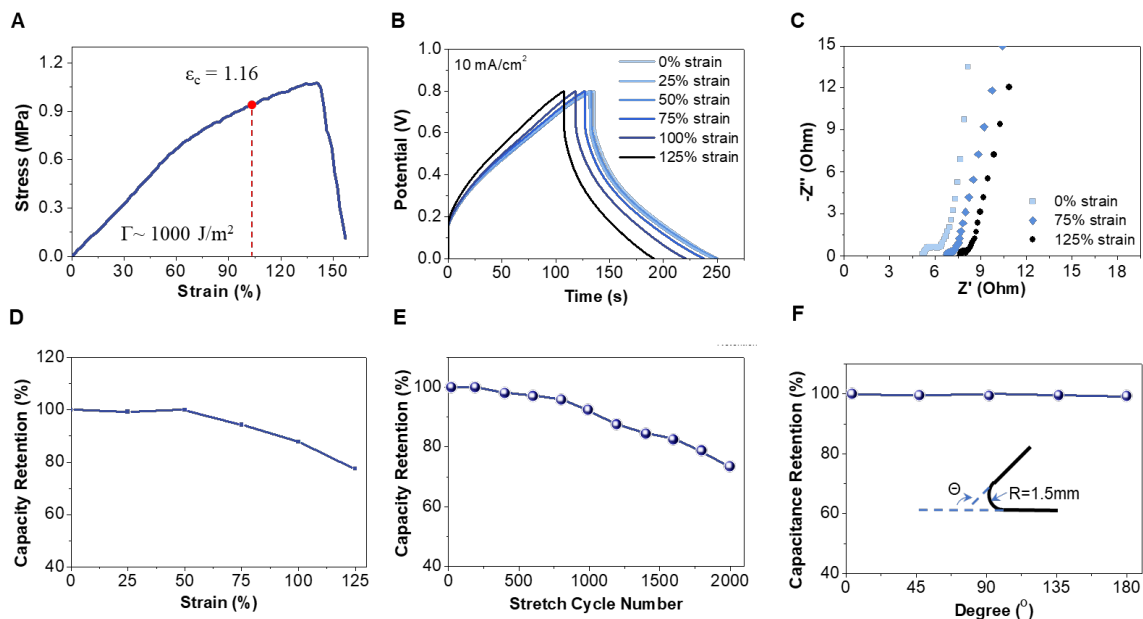
Figure 4.12 A) Stress-strain curve of TROF electrode. The red line mars the critical strain (ε_c) for

unset of propagation of crack in the material, the corresponding fracture energy is $\sim$ 1000 J m^{-2}. B)

GCD curves of TROF supercapacitor at current density of 20 mA cm^{-2} when stretched to $0 - 125\%$

strain. C) Nyquist plot of TROF supercapacitor at frequencies from 0.1M to 0.01 Hz when

stretched to 0-125% strain. D) Capacitance retention of TROF supercapacitor during stretching

from $0 - 125\%$ strain. E) Capacitance retention of TROF supercapacitor during 2000 stretching

cycles. F) Capacitance retention of TROF supercapacitor when bend from 0 -180 degrees.

In contrast, the un-reinforced foam showed only ~1 kPa strength and ~15% strain, and the PVA

infiltrate TROF electrode before salting out only slightly improved to ~4kPa strength and ~40%

strain (**Figure 4.13**).
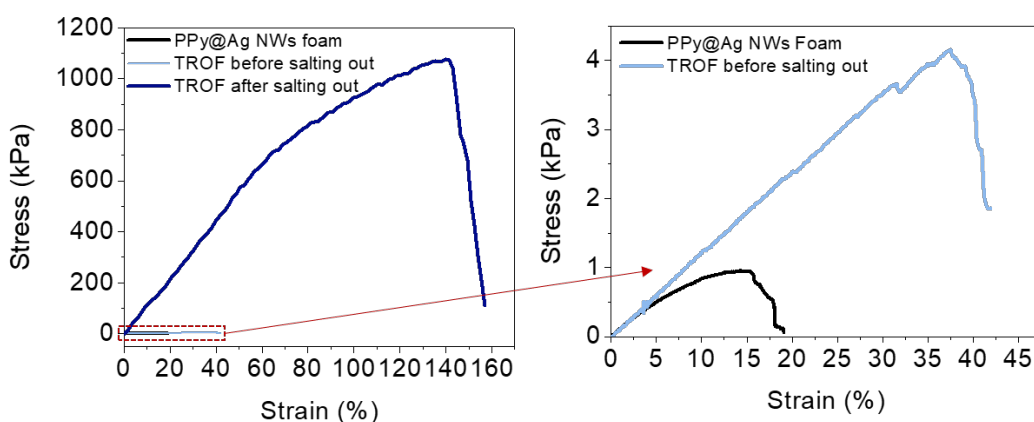
Figure 4.13 Stress-strain curve of 10 v% PPy@Ag NWs foam, without hydrogel reinforcement

and TROF electrode before and after salting out in Li_2SO_4. This tensile measurement was carried

out using a DMA TA850 mechanical tester.

Its resistance to fracture is comparable to cartilage[60] and many double-network tough hydrogels. We further evaluated the mechanical robustness of the supercapacitor device by recording the GCD curves under stretching (**Figure 4.12**B, **Figure S11**). With a strain range of 0-125%, the internal resistance (IR) at 10 mA cm^{-2} of the stretched devices increased 1.5 times as tensile strain increased from 0% to 125% (**Figure 4.12**C). As a result, the GCD curves showed an increased IR drop with the increasing strain (Figure 4.12B). Normalized to weight, the specific capacitance of the stretched device showed no reduction at up to 50% strain, which indicated an intrinsic stretchability of the device (**Figure 4.12**D). With a strain higher than 50%, the device capacitance started to gradually reduce, ultimately to 76% of the original capacitance at 125% strain. However, the capacitance could be recovered upon releasing the strain, which indicated that the tough hydrogel layer protected the integrity of the microstructure during stretching (**Figure S12**). The device showed good mechanical stability and maintained 73% of the original capacitance after 2000 mechanical cycles, each cycle was stretched to 125% strain (**Figure 4.12**E). A bending test was also carried out, where no significant capacitance change was observed for bending angle from 0 to 180 degrees (**Figure 4.12**F).

4.5 Conclusion

In this study, we presented a facile strategy to composite tough hydrogel and open-porous conducting polymer electrode through infiltration of tough hydrogel precursor and subsequent gelation by freezing-assisted salting out. The resulting composite electrodes presented an open-

porous microstructure covered by a superficial tough hydrogel layer, which harnessed simultaneous mechanical robustness, high surface area and low tortuosity. With the combined properties, the assembled all-solid-state supercapacitor based on the TROF electrode showed simultaneous high capacitance (5.25 F cm^{-2}), energy density (0.46 mWh cm^{-2}), power density (41.28 mW cm^{-2}), stretchability (140%) and fracture toughness (1000 J cm^{-2}). Benefitting from the tough hydrogel reinforcement, the supercapacitor showed good electrical stability (95.8% after 3500 GCD cycles) and mechanical stability (73% after 2000 mechanical cycles) with a moderate reduction in performance. With the presented facile method for coating tough hydrogel reinforcement layer and various conducting foam materials available, the presented strategy could be expanded to other electrode systems for bringing improvements in stretchability and toughness of electrode. We foresee that many fine structures used in energy storage, sensing and robotic fields could be strengthened using the presented strategy and we are convinced that compositing tough hydrogel and these fine structures opens up new opportunities for the application of structural hydrogel in the fields of energy storage, sensing, soft robotics and stretchable electronic devices.

4.6 References

[1]   F. Wang, X. Wu, X. Yuan, Z. Liu, Y. Zhang, L. Fu, Y. Zhu, Q. Zhou, Y. Wu, W. Huang, *Chem. Soc. Rev.* **2017**, *46*, 6816.

[2]   J. R. Miller, P. Simon, *Science (80-.).* **2008**, *321*, 651.

[3]   P. Simon, Y. Gogotsi, B. Dunn, *Science (80-.).* **2014**, *343*, 1210.

[4]   X. Lu, M. Yu, G. Wang, Y. Tong, Y. Li, *Energy Environ. Sci.* **2014**, *7*, 2160.

[5]   D. P. Dubal, N. R. Chodankar, D. H. Kim, P. Gomez-Romero, *Chem. Soc. Rev.* **2018**, *47*, 2065.

[6]   T. Lv, M. Liu, D. Zhu, L. Gan, T. Chen, *Adv. Mater.* **2018**, *30*, 1.

[7]   J. C. Yang, J. Mun, S. Y. Kwon, S. Park, Z. Bao, S. Park, *Adv. Mater.* **2019**, *31*, 1904765.

[8]   Y. Liu, J. Li, S. Song, J. Kang, Y. Tsao, S. Chen, V. Mottini, K. McConnell, W. Xu, Y. Q. Zheng, J. B. H. Tok, P. M. George, Z. Bao, *Nat. Biotechnol.* **2020**, *38*, 1031.

[9]   Y. Kim, G. A. Parada, S. Liu, X. Zhao, *Sci. Robot.* **2019**, *4*, eaax7329.

[10]   Y. Zhao, C.-Y. Lo, L. Ruan, C.-H. Pi, C. Kim, Y. Alsaid, I. Frenkel, R. Rico, T.-C. Tsao, X. He, *Sci. Robot.* **2021**, *in press*.

[11]   Y. Kim, A. Chortos, W. Xu, Y. Liu, J. Y. Oh, D. Son, J. Kang, A. M. Foudeh, C. Zhu, Y. Lee, S. Niu, J. Liu, R. Pfattner, Z. Bao, T. W. Lee, *Science (80-.).* **2018**, *360*, 998.

[12]   D. G. Mackanic, M. Kao, Z. Bao, *Adv. Energy Mater.* **2020**, *10*, 1.

[13]   D. G. Mackanic, T. H. Chang, Z. Huang, Y. Cui, Z. Bao, *Chem. Soc. Rev.* **2020**, *49*, 4466.

[14]   L. Li, Z. Lou, D. Chen, K. Jiang, W. Han, G. Shen, *Small* **2018**, *14*, 1.

[15]   S. Ghosh, O. Inganäs, *Adv. Mater.* **1999**, *11*, 1214.

[16]   M. Salanne, B. Rotenberg, K. Naoi, K. Kaneko, P. L. Taberna, C. P. Grey, B. Dunn, P. Simon, *Nat. Energy* **2016**, *1*.

[17]   F. Zhao, J. Bae, X. Zhou, Y. Guo, G. Yu, *Adv. Mater.* **2018**, *30*, 1.

[18]   Y. Guo, K. Zheng, P. Wan, *Small* **2018**, *14*, 1.

[19] K. Wang, X. Zhang, C. Li, X. Sun, Q. Meng, Y. Ma, Z. Wei, *Adv. Mater.* **2015**, *27*, 7451.

[20] L. Zang, Q. Liu, J. Qiu, C. Yang, C. Wei, C. Liu, L. Lao, *ACS Appl. Mater. Interfaces* **2017**, *9*, 33941.

[21] Y. Zhao, Y. Alsaid, B. Yao, Y. Zhang, B. Zhang, N. Bhuskute, S. Wu, X. He, *Adv. Funct. Mater.* **2020**, *1909133*, 1.

[22] G. P. Hao, F. Hippauf, M. Oschatz, F. M. Wisser, A. Leifert, W. Nickel, N. Mohamed-Noriega, Z. Zheng, S. Kaskel, *ACS Nano* **2014**, *8*, 7138.

[23] P. Li, Z. Jin, L. Peng, F. Zhao, D. Xiao, Y. Jin, G. Yu, *Adv. Mater.* **2018**, *30*, 1800124.

[24] W. Li, F. Gao, X. Wang, N. Zhang, M. Ma, *Angew. Chemie Int. Ed.* **2016**, *55*, 9196.

[25] Q. Chen, H. Lu, F. Chen, L. Chen, N. Zhang, M. Ma, *ACS Appl. Energy Mater.* **2018**, *1*, 4261.

[26] B. S. Yin, S. W. Zhang, Q. Q. Ren, C. Liu, K. Ke, Z. B. Wang, *J. Mater. Chem. A* **2017**, *5*, 24942.

[27] Y. Zhao, B. Zhang, B. Yao, Y. Qiu, Z. Peng, Y. Zhang, Y. Alsaid, I. Frenkel, K. Youssef, Q. Pei, X. He, *Matter* **2020**, *3*, 1196.

[28] E. P. Gilshteyn, D. Amanbayev, A. S. Anisimov, T. Kallio, A. G. Nasibulin, *Sci. Rep.* **2017**, *7*, 1.

[29] C. Chen, Y. Zhang, Y. Li, J. Dai, J. Song, Y. Yao, Y. Gong, I. Kierzewski, J. Xie, L. Hu, *Energy Environ. Sci.* **2017**, *10*, 538.

[30] Y. Wang, Y. Shi, L. Pan, Y. Ding, Y. Zhao, Y. Li, Y. Shi, G. Yu, *Nano Lett.* **2015**, *15*,

7736.

[31]   Y. Xu, Z. Lin, X. Huang, Y. Wang, Y. Huang, X. Duan, *Adv. Mater.* **2013**, *25*, 5779.

[32]   Y. Shi, L. Pan, B. Liu, Y. Wang, Y. Cui, Z. Bao, G. Yu, *J. Mater. Chem. A* **2014**, *2*, 6086.

[33]   Y. Wang, C. Zhu, R. Pfattner, H. Yan, L. Jin, S. Chen, F. Molina-Lopez, F. Lissel, J. Liu,
       N. I. Rabiah, Z. Chen, J. W. Chung, C. Linder, M. F. Toney, B. Murmann, Z. Bao, *Sci.
       Adv.* **2017**, *3*, 1.

[34]   Y. Wang, X. Lin, T. Liu, H. Chen, S. Chen, Z. Jiang, J. Liu, J. Huang, M. Liu, *Adv. Funct.
       Mater.* **2018**, *28*, 1.

[35]   C. Chen, Y. Zhang, Y. Li, Y. Kuang, J. Song, W. Luo, Y. Wang, Y. Yao, G. Pastel, J. Xie,
       L. Hu, *Adv. Energy Mater.* **2017**, *7*, 3.

[36]   X. L. Wu, T. Wen, H. L. Guo, S. Yang, X. Wang, A. W. Xu, *ACS Nano* **2013**, *7*, 3589.

[37]   W. Chen, R. B. Rakhi, L. Hu, X. Xie, Y. Cui, H. N. Alshareef, *Nano Lett.* **2011**, *11*, 5165.

[38]   W. He, G. Li, S. Zhang, Y. Wei, J. Wang, Q. Li, X. Zhang, *ACS Nano* **2015**, *9*, 4244.

[39]   J. Zhou, L. Yu, W. Liu, X. Zhang, W. Mu, X. Du, Z. Zhang, Y. Deng, *Sci. Rep.* **2015**, *5*, 1.

[40]   H. Park, J. W. Kim, S. Y. Hong, G. Lee, D. S. Kim, J. hyun Oh, S. W. Jin, Y. R. Jeong, S.
       Y. Oh, J. Y. Yun, J. S. Ha, *Adv. Funct. Mater.* **2018**, *28*, 1.

[41]   T. Purkait, G. Singh, D. Kumar, M. Singh, R. S. Dey, *Sci. Rep.* **2018**, *8*, 1.

[42]   G. Shao, R. Yu, X. Zhang, X. Chen, F. He, X. Zhao, N. Chen, M. Ye, X. Y. Liu, *Adv.
       Funct. Mater.* **2020**, *2003153*, 1.

[43]   W. Li, M. C. Tekell, C. Liu, J. A. Hethcock, D. Fan, *Adv. Funct. Mater.* **2018**, *28*, 1.

[44] Z. Ren, Y. Li, J. Yu, *iScience* **2018**, *9*, 138.

[45] X. Zhang, J. Zhao, T. Xia, Q. Li, C. Ao, Q. Wang, W. Zhang, C. Lu, Y. Deng, *Energy Storage Mater.* **2020**, *31*, 135.

[46] S. Lin, J. Liu, X. Liu, X. Zhao, *Proc. Natl. Acad. Sci. U. S. A.* **2019**, *116*, 10244.

[47] S. Lin, X. Liu, J. Liu, H. Yuk, H.-C. Loh, G. A. Parada, C. Settens, J. Song, A. Masic, G. H. McKinley, X. Zhao, *Sci. Adv.* **2019**, *5*, eaau8528.

[48] R. Bai, J. Yang, X. P. Morelle, Z. Suo, *Macromol. Rapid Commun.* **2019**, *40*, 1.

[49] H. Zhang, *Ice Templating and Freeze-Drying for Porous Materials and Their Applications*; Wiley-VCH Verlag GmbH & Co. KGaA: Weinheim, Germany, 2018.

[50] J. Jiu, T. Araki, J. Wang, M. Nogi, T. Sugahara, S. Nagao, H. Koga, K. Suganuma, E. Nakazawa, M. Hara, H. Uchida, K. Shinozaki, *J. Mater. Chem. A* **2014**, *2*, 6326.

[51] R. Liu, B. L. Sang, *J. Am. Chem. Soc.* **2008**, *130*, 2942.

[52] M. Gao, S. Huang, L. Dai, G. Wallace, R. Gao, Z. Wang, *Angew. Chemie - Int. Ed.* **2000**, *39*, 3664.

[53] S. Wu, M. Hua, Y. Alsaid, Y. Du, Y. Ma, Y. Zhao, C.-Y. Lo, C. Wang, D. Wu, B. Yao, J. Strzalka, H. Zhou, X. Zhu, X. He, *Adv. Mater.* **2021**, *33*, 2007829.

[54] H. Zhang, I. Hussain, M. Brust, M. F. Butler, S. P. Rannard, A. I. Cooper, *Nat. Mater.* **2005**, *4*, 787.

[55] M. Hua, S. Wu, Y. Ma, Y. Zhao, Z. Chen, I. Frenkel, J. Strzalka, H. Zhou, X. Zhu, X. He, *Nature* **2021**, *590*, 594.

[56]   S. Gupta, S. Goswami, A. Sinha, *Biomed. Mater.* **2012**, *7*.

[57]   P. Van De Witte, P. J. Dijkstra, J. W. A. Van Den Berg, J. Feijen, *J. Memb. Sci.* **1996**, *117*, 1.

[58]   M. Iwaseya, M. Watanabe, K. Yamaura, L. X. Dai, H. Noguchi, *J. Mater. Sci.* **2005**, *40*, 5695.

[59]   S. Paţachia, C. Florea, C. Friedrich, Y. Thomann, *Express Polym. Lett.* **2009**, *3*, 320.

[60]   N. K. Simha, C. S. Carlson, J. L. Lewis, *J. Mater. Sci. Mater. Med.* **2004**, *15*, 631.

5. 3D Printing of Tough Hydrogels prepared by Freezing Assisted Salting Out

5.1 Introduction

Stimuli-responsive hydrogels are widely used for soft actuators and soft robots due to their facile fabrication, diverse actuation modes, high degree of freedom during actuation.[1] Hydrogel actuators are seeing growing interests as under-water robots and biomedical tools in light of their excellent compatibility with aqueous and biological environment.[2–6] Among various stimuli-responsive polymeric actuators, thermo-responsive ones have attracted particular interest due to the easy induction of thermal energy in the material without compositional change to the system.[7,8] Poly(N-isopropylacrylamide) (PNIPAM) hydrogels are a representative example that exhibits distinct behaviors at temperatures above or below its lower critical solution temperature (LCST).[9] PNIPAM hydrogels absorb water and swell at a temperature below LCST and conversely expel water and shrink at temperature above LCST. PNIPAM based actuators have shown significant advantages over many other types of hydrogels due to remote powering and control capabilities when conjugated with photothermal / magnetothermal materials.[4,6,10]

Conventional hydrogels, especially PNIAPM hydrogels, are mechanically weak due to their low solid contents (70-98% water contents) and lack of energy dissipating mechanisms.[11–15] Their intrinsic softness and fragileness lead to low deliverable force[16,17] and large passive deformation

upon contact when applied as actuators, which hinders their use in   practical applications that involves high loads, abrupt impacts, and long-term services. Various methods such as forming double networks (DN),[12,18] having dual crosslinking[19] and compositing[20–25] were introduced for toughening hydrogels. However, many tough hydrogels are incapable of actuation by ambient stimuli while maintaining high toughness, due to the consumption of stimuli responsive sites or immobilization by the secondary networks or stiff fillers during the toughening process. For PNIPAM hydrogels, some viable approaches utilized solvent exchanges that induced strong aggregation or collapse of polymer chains for combined strengthening and actuation.[26–33] These methods require replenishing the entire body of solvent for reverse actuation and therefore limit the working environment of actuators to finite-sized containers. Alternatively, electro-actuation and pneumatic / hydraulic actuation have been employed to actuate tough hydrogels,[5,34,35] which requires external powering and pumping systems to supply sufficient voltage or pressure.

Achieving high mechanical robustness and stimuli responsiveness simultaneously has been difficult for hydrogels. Many toughening methods that involve addition of secondary networks,[18] crosslinkers[12] or reinforcements[23,24] are incompatible for building tough and stimuli-responsive actuators, as the stimuli-responsive network is internally restrained by the non-responsive toughening components. Some water-free polymer systems are easily made to be tough and stimuli responsive, like liquid crystal elastomers (LCEs)[36,37] and poly(pyrrole).[38] These materials consist of tough polymer backbones and stimuli responsive functional groups in a single network.

Therefore, it would be advantageous to synthesize hydrogels with an intrinsically tough and stimuli responsive network to realize simultaneous high toughness and stimuli-responsiveness.

5.2 Proposed Method

We studied a tough and responsive hydrogel synthesized by grafting stimuli-responsive monomers to polymers with high toughness. Poly(vinyl alcohol) (PVA) is a high molecular-weight polymer with excellent mechanical properties due to its high fracture toughness compared to the short chain counterparts.[39] PVA also has a good ability to form nano-crystalline domains for further strengthening and toughening the network via post treatments.[40,41] Therefore, we used PVA and its methacrylate derivatives (PVA-MA) as the tough polymer backbone. The modification from PVA to PVA-MA enabled the photo polymerization of this tough polymer. In this study, N-isopropylacrylamide (NIPAM) was used as an exemplary responsive monomer for grafting onto the PVA-MA backbone to give PVA thermo-responsiveness and PVA/(PVA-MA)-g-PNIPAM hydrogel was fabricated via digital light processing (DLP) based 4D printing.[42] A facile salting out treatment was used subsequently to induce the formation of PVA nano-crystalline domains to further strengthen the hydrogel network. The printed hydrogels showed exceptionally high strength, high toughness, good thermo-responsiveness, and improved actuation force, and they are highly tunable owing to the ability to spatially program the material properties by 4D printing. The presented tough and responsive hydrogel system, with its simple synthesis and modular design, holds great potential for constructing tough and high-power soft-robots, bio-medical devices, and

hydrogel actuators.

5.3 Experimental and Characterization Section

5.3.1 Materials

Poly(vinyl alcohol) (PVA, 99% hydrolyzed, M.W 89,000 - 98,000), N-isopropylacrylamide (NIPAM, 99%), Methacrylic acid (MA, 99%), N,N'-Methylenebisacrylamide (Bis), 2-Hydroxy-4′-(2-hydroxyethoxy)-2-methylpropiophenone (Irgacure 2959), tartrazine and hydroquinone were purchased from Sigma Aldrich. Lithium phenyl-2,4,6-trimethylbenzoylphosphinate (TPO-Li) was purchased from CPS Polymers. Hexane, hydrochloric acid, acetone and triethyl amine was purchased from Fisher Scientifics. NIPAM was purified by recrystallization in hexane. All other chemicals were used without further treatment.

5.3.2 Synthesis of PVA-MA

The PVA-MA was synthesized by a condensation reaction between PVA and MA (**Figure 5.1**A). Typically, 20 g of PVA was dissolved in 180 mL of DI water conical flask with heating. 40 mg of hydroquinone was added to the solution. After cooling down, 5 mL MA and 10 mL hydrochloric acid was added to the solution. The mixture was stirred at 300 rpm and 60 ℃ for 12 h. After cooling down, 15 mL triethyl amine was added to the solution. The whole solution was then diluted 10 times and precipitated in acetone. The precipitate was finally filtered and dried in vacuum.
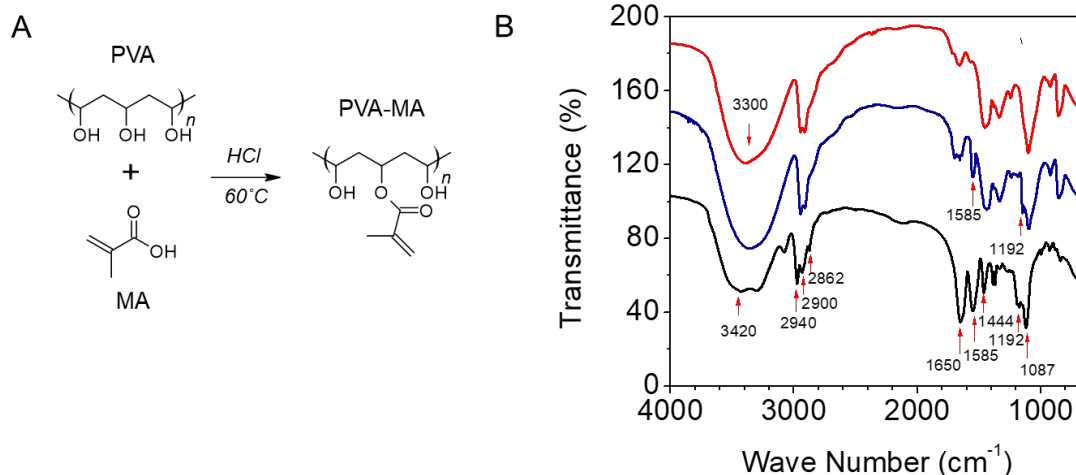
Figure 5.1 A) Synthesis route of PVA-MA from poly(vinyl alcohol) (PVA) and methacrylic acid (MA). B) FTIR spectrum of the pristine PVA (red), PVA-MA (blue) and PVA/(PVA-MA)-g-PNIPAM hydrogel (black). 3420 cm^{-1} (N-H in NIPAM groups), 3300 cm^{-1} (broad peak indicating the O–H in PVA), 2940 cm^{-1} (C–H in PVA), 2900 cm^{-1} (C-CH$_2$ in methacrylate groups), 2862 cm^{-1} (C-CH$_3$ in methacrylate and NIPAM groups), 1650 cm^{-1} (C=O in NIPAM groups), 1585 cm^{-1} (C=C in methacrylate groups), 1444 cm^{-1} (C-H in methacrylate and NIPAM groups), 1192 cm^{-1} (C-O-C between PVA and methacrylate groups), 1087 cm^{-1} (C-O-H in PVA). When comparing PVA (red) and PVA-MA (blue), we could see the peaks at 1192 cm^{-1} and 1585 cm^{-1} which corresponds to the formation of ester bond and the grafted MA containing C=C bond.

5.3.3 Preparation of Printing Precursor

The printing precursor consists of (10-x) wt% PVA, x wt% PVA-MA, 20 wt% NIPAM and 0.1 wt% TPO-Li dissolved in water. The hydrogels were denoted as "xP-MA_(10-x)P" for x wt% of PVA-MA added in the total precursor. For controlling light penetration depth, 0.2 wt% tartrazine as

109

photo-absorber was added to the precursor. The ratio of PVA and PVA-MA was adjusted between 0:10 to 7:3 for achieving different properties.

5.3.4 Printer Setup

The home-made printer consists of an DLP-based PRO4500 UV light (385 nm) projector from Wintech Digital System Technology Corporation, a motorized translation stage mounted to a motor controller, and other optical accessories from Thorlabs, Inc. The power density of the projected UV light on the focal plane is measured to be 2.34 mW/cm^2 using an ultraviolet light meter, Traceable Products. A customized program was used to coordinate the projection of image and the movement of the stage. The resolution of the printer was 30 μm in the x–y plane and 10 μm in the z-axis direction.

5.3.5 Printing Process

All the printing proceeded in air under ambient conditions. A 3D computer aided design (CAD) models was first designed and sliced into series of 2D patterns. The patterns were sequentially projected onto the substrate, which was immersed in the precursor solution. The thickness of each layer was set to be 0.1 mm. Each layer was cured for 30 s. For printing the bilayer structures, a bottom layer was printed, rinsed with DI water to remove the unreacted precursor and dried. Then the printed layer was immersed in a second precursor and a layer with different material was printed on the top. All the samples tested for following measurements of mechanical properties,

contraction force, and swelling ratio were all printed by this process.

5.3.6 Salting-out Treatment

The printed hydrogels were first immersed in DI water for 24 hours to remove the excess monomers and then immersed in 0.1-1 M Na_2SO_4 solution for 5 hours to induce aggregation and crystallization of the PVA and PVA-MA chains.

5.3.7 Mechanical Properties Measurement

A Cellscale Univert mechanical tester was used for measuring passive mechanical properties and active contraction of the hydrogel. For passive tensile tests, dog bone specimens with 2 mm gauge width, 4mm gauge length and 2 mm thickness was 3D printed and measured using a 4.5 N loading cell under stretch rate of 0.1 /s.   For passive compression tests, cylindrical specimen with 5mm diameter and 2mm height was 3D printed and measured using a 10 N loading cell under compression rate of 0.01/s.

5.3.8 Contraction Force Measurement

For active contraction force measurement, the dog bone specimen was clamped at fixed distance of 4mm using the tensile testing setup with water bath compartment installed, hot water was poured into the bath container and the contraction force was recorded using a 0.5 N loading cell.

5.3.9 Swelling Ratio Measurement

The cylindrical specimen for compression test was equilibrated in water and heated to 40 °C using a hot plate. The area change of the specimen was recorded using a camera from top. It is assumed that the specimen showed uniform volume change in all directions. The volumetric swelling ratio was calculated using the following:

$$Contraction\ ratio = (\frac{Area_{40°C}}{Area_{25°C}})^{3/2}$$

5.3.10 Microstructure Characterization

All hydrogel samples were immersed in DI water for 24 hours before freeze-drying using a Labconco FreeZone freeze dryer. The freeze-dried hydrogels were cut to expose the inside and sputtered with gold before carrying out imaging using a ZEISS Supra 40VP SEM.

5.3.11 XRD Characterization

The hydrogel sample was cut into a rectangular shape with dimensions of 2 cm x 1 cm x 4 mm and placed in rectangular sample holders for examination, and the resulting spectrum were analyzed by built-in database on Panalytical X'Pert Pro Powder X-ray Diffractometer.

5.3.12 DSC characterization

Before freeze-drying the hydrogels for DSC measurements, we first used excess chemical cross-links induced by glutaraldehyde to fix the amorphous PVA polymer chains to minimize the further formation of crystalline domains during the air-drying process following reference[40] . The water

content of the hydrogel f_{water} could be obtained by comparing the weight before and after freeze-drying. In a typical DSC measurement, we first weighed the total mass of the freeze-dried sample m. The sample was thereafter placed in a Tzero pan and heated up from 50 °C to 250 °C at the rate of 20 °C/min under a nitrogen atmosphere with flow rate of 30 mL/min. The curve of heat flow shows another narrow peak ranging from 200 °C to 250 °C, which correspond to the melting of the crystalline domains. The integration of the endothermic transition ranging from 200 °C to 250 °C gives the enthalpy for melting the crystalline domains per unit mass of the dry. Therefore, the mass of the crystalline domains $m_{crystalline}$ can be calculated as $m_{crystalline} = m * H_{crystalline}/H^0_{crystalline}$, where $H^0_{crystalline} = 138.6$ J/g is the enthalpy of fusion of 100 wt.% crystalline PVA measured at the equilibrium melting point T^0_m [43]. Therefore, the crystallinity in the dry sample X_{dry} can be calculated as $X_{dry} = m_{crystalline}/m$. With measured water content from freeze drying, the crystallinity in the swollen state can be calculated as $X_{swollen} = X_{dry} * (1 - f_{water})$.

5.3.13 FT-IR Characterization

The Fourier-transform infrared spectroscopy (FT-IR) analysis was conducted using JASCO Model 420 FT-IR using a potassium bromide (KBr) pellet. FT-IR spectra were recorded in the spectral range of 4000–400 cm-1 with a 2 cm-1 resolution and 32 scans.

5.4 Result and Discussion

5.4.1 Material Design

Figure 5.2A & B showed the one-pot synthesis of the PVA/(PVA-MA)-g-PNIPAM hydrogel. PVA and PVA-MA were used as the tough polymer backbone for two reasons. First, due to the high molecular weight of PVA, the fracture energy of PVA chains is much higher than the relatively short polymer chains formed via radical polymerization from monomers. The energy required to fracture a polymer chain (Γ) scales proportionally with the polymer chains length (n repeating units) according to Lake-Thomas theory ($\Gamma \propto \sqrt{n}$).[39] Second, PVA is easy to crystallize via thermal annealing or phase separation processes.[40,41,44] The crystalline domains can toughen hydrogels by inhibiting crack propagation, crosslinking multiple chains and increase the fracture energy of polymer chains, as the energy required to fracture crystalized chains are much higher than that of its amorphous counterpart. For subsequent grafting of thermally responsive monomers onto the PVA chains, the PVA polymers went through a simple condensation reaction with methacrylic acid (MA) in an acidic environment and produced a UV crosslink-able derivative PVA polymer (**Figure 5.3**) with the hydroxyl (-OH) side groups partially modified with the methacrylate (-MA) side groups, termed as PVA-MA (**Figure 5.1**A). However, note that PVA-MA has reduced ability to crystalize due to the steric hindrance by the modified side group. Therefore, non-modified pristine PVA was blended with PVA-MA in the precursor for retaining good crystallization ability for toughening the hydrogel. Additionally, PVA-MA is crucial for the grating of NIPAM molecules onto the PVA network, which in turn gave rise to the thermal responsiveness of the hydrogel. Therefore, a balanced concentration of PVA and PVA-MA should be used for optimum combined mechanical properties and thermal responsiveness. The hydrogels were denoted as "*x*P-MA_(10-

x)P" for *x* wt% of PVA-MA added in the total precursor, and we mainly used 5P-MA_5P hydrogel in our study due to its combined high strength, high stretchability and good thermal responsiveness. Additionally, water was used as the solvent instead of organic solvents for green synthesis, and TPO-Li was used as the photo-initiator in the aqueous precursor, due to its ability to induce radical polymerization under both visible and UV spectra to fit different printing systems. PVA, PVA-MA, NIPAM and TPO-Li were dissolved in water (**Figure 5.2**A) and exposed to UV light for gelation (**Figure 5.2**B). No crosslinker was added to ensure that all retained NIPAM molecules were attached to the PVA-MA backbone after rinsing. The fabricated hydrogel was transparent and colored with the photo absorber dye added to the precursor (**Figure 5.2**B, bottom image). The chemical composition of the obtained hydrogel was verified with FT-IR analysis (**Figure 5.1**B).
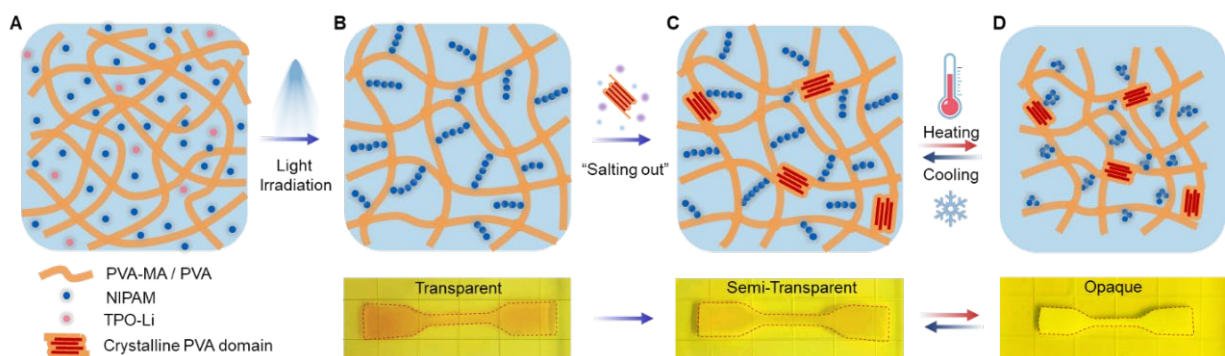
Figure 5.2 Illustration of the synthesis of PVA/(PVA-MA)-g-PNIPAM hydrogel. A) Aqueous precursor containing PVA, PVA-MA, NIPAM and TPO-Li. B) The one-pot synthesis of PVA/(PVA-MA)-g-PNIPAM hydrogel by light irradiation from a DLP 3D printer. The as-printed hydrogel was transparent. C) Toughening of hydrogel by immersion in Na_2SO_4 salt solution to induce PVA aggregation and crystallization. The hydrogel turned semi-transparent after the salting-

out process. D) Actuation of the hydrogel by heating, and the recovery of hydrogel by cooling. The

hydrogel turned completely opaque after heating and reverted to semi-transparent after cooling.
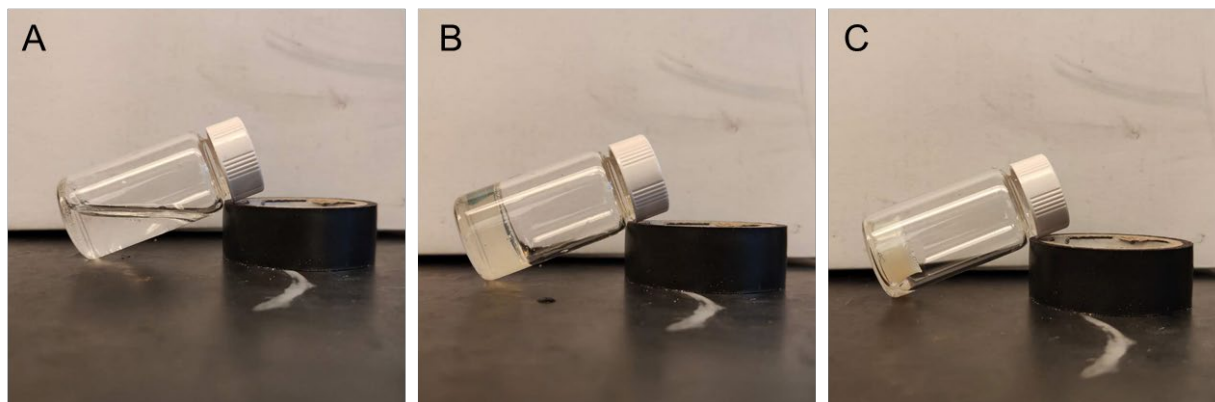
Figure 5.3 A) 10% PVA-MA, 0.5% TPO-Li dissolved in water. B) PVA-MA hydrogel obtained

after UV irradiating the precursor in A. C) Toughened PVA-MA hydrogel after salting out in 1M

Na_2SO_4 solution for 5 hours.

To further toughen the PVA/(PVA-MA)-g-PNIPAM hydrogel, the 3D printed sample was then

immersed into Na_2SO_4 salt solutions of various concentrations to induce aggregation and

crystallization of the PVA chains. The treatment is known as salting out and is based on the

classical Hofmeister effect, in which different ions has distinguishable ability to induced phase

separation of solutes and precipitate the dissolved polymers.[45] The sulfate ions have strong ability

to induce aggregation and crystallization of the PVA and were used as the salting out agent in this

study.[20,44,46] The sample transitioned from transparent to semi-transparent after the salting out

treatment, and remained semi-transparent even when immersed back into water, indicating the

formation of nano-crystalline domains that strongly scattered light (**Figure 5.2**C, **Figure 5.4**).
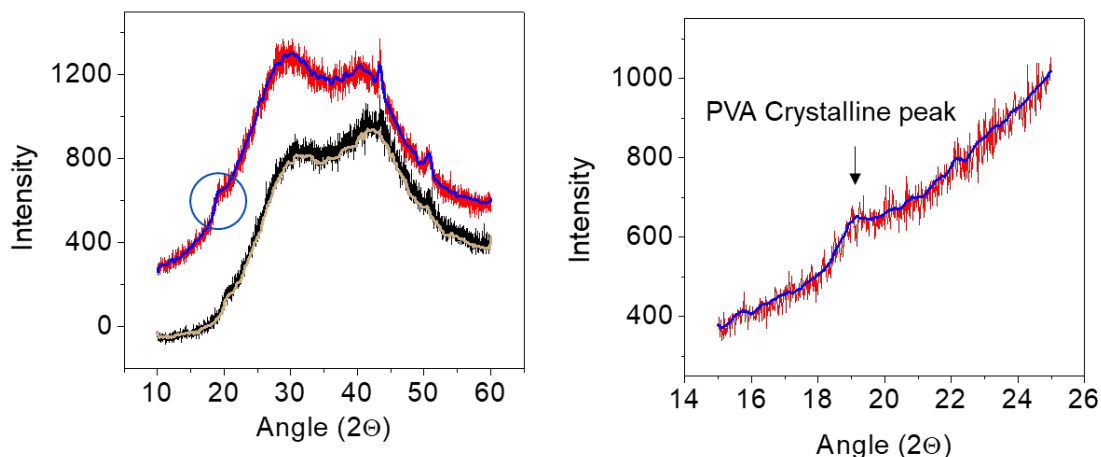
Figure 5.4 XRD pattern of PVA/(PVA-MA)-g-PNIPAM hydrogel before (black) and after (red) toughening by salting out treatment.

The toughened PVA/(PVA-MA)-g-PNIPAM hydrogel by salting out maintained the reversible thermal responsiveness in water (**Figure 5.2**D), benefiting from the single network design. The thermal responsive side groups / side chains were combined with the tough hydrogel network, which reduced the internal constraint between the thermal responsive and non-thermal responsive domains in the hydrogel network. When heated above the LCST of PNIPAM, the hydrogel quickly turned opaque as the grafted NIPAM chains phase separated from water and formed globules that additionally scattered light. The volume change was slower than the color change due to the hydrogel's bulk size, and the hydrogel gradually shrunk in size overtime. This could be caused by the relatively small pore size (0.2 – 2 μm) and bulk sample size of the hydrogel, which hindered the diffusion of water in / out of the hydrogel network (**Figure 5.5**). When lowering the bath

temperature to below LCST, the hydrogel could recover to the original size and color. Owing to the 3D printability of the hydrogel, large voids serving as efficient water channels could be printed in the hydrogel structure for bypassing the size dependent volume change of the hydrogel and increase actuation speed.
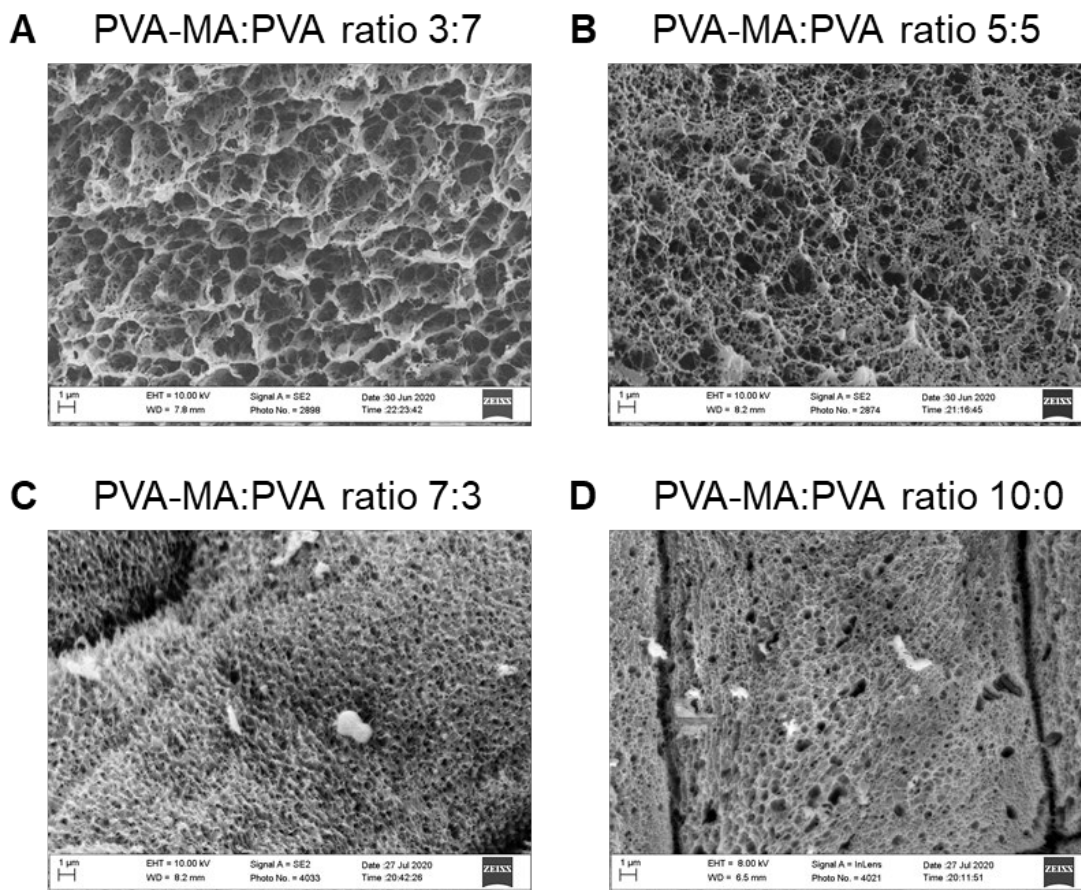
Figure 5.5 Microstructure of the PVA/(PVA-MA)-g-PNIPAM hydrogels with different PVA to PVA-MA ratios. The hydrogels were toughened in 0.5 M Na_2SO_4 solution, washed and then freeze -dried. The pore size decreased with increasing PVA-MA content.

5.4.2 Passive Mechanical Properties

The typical tensile and compressive stress-strain curves of the printed PVA/(PVA-MA)-g-PNIPAM hydrogel with respect to concentration of Na_2SO_4 solution are shown in **Figure 5.6**A & B. All hydrogels were rinsed in DI water to remove the salt prior to mechanical testing. The maximum stress and strain of the hydrogel increased with the concentration of Na_2SO_4 used for salting out, mainly due to the increasing aggregation and crystallinity of the hydrogel with increasing concentration of salting out agent (**Figure 5.6**A & B). The typical 5P-MA_5P hydrogel reached ~15% crystallinity against the total solid content corresponding to ~1.5% crystallinity in the wet state after salting out for 5 hours. The PVA crystalline domains significantly strengthened the hydrogel by their ability to pin down cracks,[41] they also improved hydrogel's elasticity by acting as rigid high functionality crosslinkers.[13]

Figure 5.6 Mechanical properties of PVA/(PVA-MA)-g-PNIPAM hydrogels. A & B) The tensile and compressive stress-strain curves of 5P-MA_5P hydrogel toughened in different concentra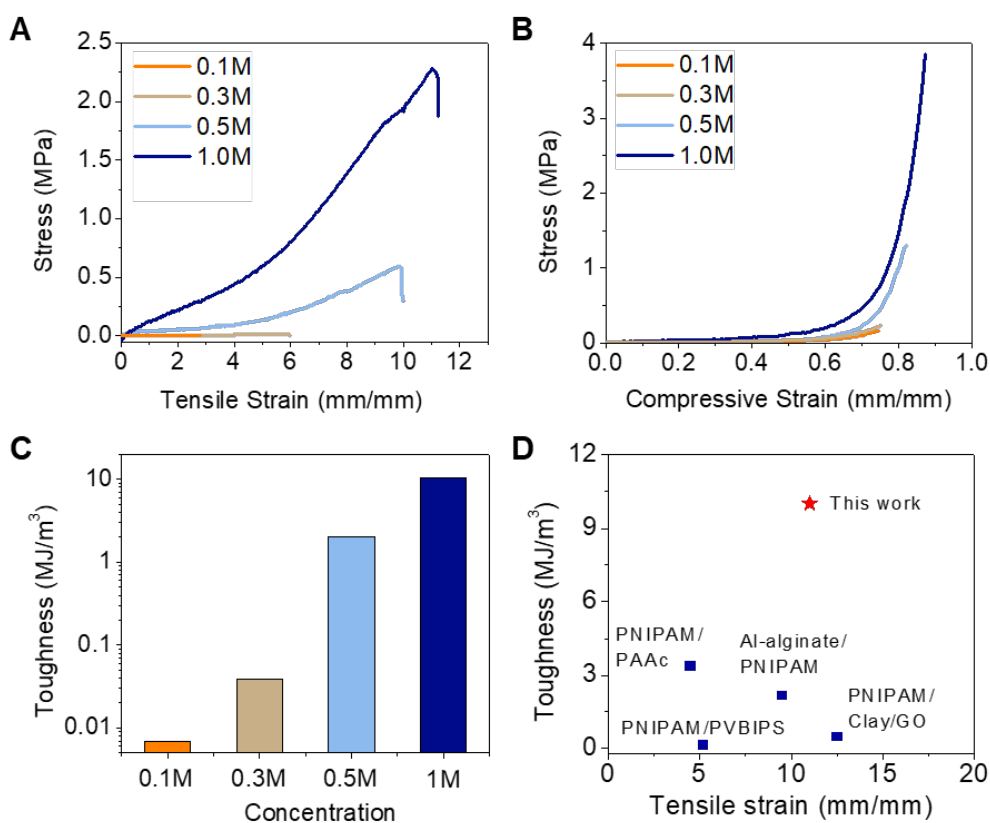tions of Na_2SO_4 salt solution. C) The tensile toughness of 5P-MA_5P hydrogels that were toughened in different concentrations of Na_2SO_4 salt solutions. D) Ashby diagram showing the toughness vs. strain properties of 5P-MA_5P hydrogel compared with other tough NIPAM hydrogel systems.

For a typical 5P-MA_5P hydrogel, the tensile strength increased from 0.015 MPa to 2.2 MPa (**Figure 5.6**A), and the compressive strength increased from 0.16 MPa to 3.8 MPa (**Figure 5.6**B) after the salting-out treatment in 1M Na_2SO_4 solution. The corresponding toughness of the 5P-MA_5P hydrogel reached 10 MJ/m^3 (**Figure 5.6**C), comparable to that of natural tendons. Compared with other double-network tough NIPAM hydrogels,[30,47–49] the PVA/(PVA-MA)-g-PNIPAM hydrogel showed high stretchability, strength and toughness (**Figure 5.6**D).

5.4.3 Active Actuation Properties

The PVA/(PVA-MA)-g-PNIPAM hydrogel maintained thermal responsiveness after the toughening process by salting out (**Figure 5.7**A-C), benefiting from the combination of thermal responsive side groups and tough polymer main chains in a single network. For a typical 5P-MA_5P hydrogel, the volumetric contraction could reach 50% for hydrogels toughened in 0.1M Na_2SO_4, comparable to the pure PNIPAM hydrogel (60% contraction). Although, the volumetric contraction decreased with increasing salt concentration, which was due to the reduced polymer

chain mobility as the PVA and (PVA-MA)-g-PNIPAM polymer chains aggregated and crystalized during the salting out process, the ultra-tough 5P-MA_5P hydrogel toughened in 1M Na_2SO_4 still maintained around 10% volumetric contraction (**Figure 5.7**B). The PVA/PVA-MA ratio also showed effect on the swelling ratio (**Figure 5.7**C). The contraction of the PVA/(PVA-MA)-g-PNIPAM hydrogel increased with the PVA-MA concentration. On one hand, higher PVA content increased the aggregates and crystalline domains formed during salting out for better toughening of the hydrogel (**Figure 5.8**A-C) but provided fewer grafting sites for increasing thermal responsiveness of the hydrogel network. On the other hand, higher PVA-MA increased the amount of NIPAM grafted to the hydrogel network, which in turn improved the thermal responsiveness of the hydrogel, but would lead to higher chemical crosslinking density[50,51] (**Figure 5.9**), which reduced the maximum strain of the hydrogel (**Figure 5.8**A-C).
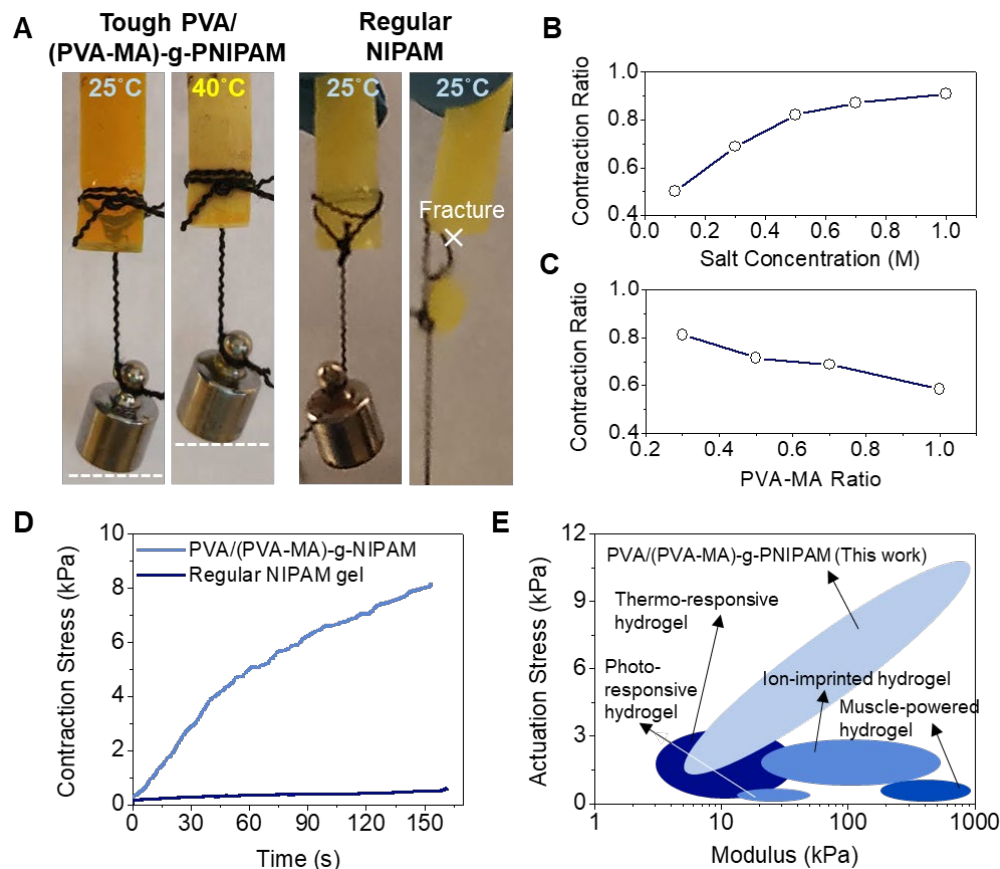
Figure 5.7 Actuation and output stress of PVA/(PVA-MA)-g-PNIPAM hydrogel. A) Application of PVA/(PVA-MA)-g-PNIPAM hydrogel as linear actuator compared with NIPAM hydrogel. The 5P-MA_5P hydrogel toughened in 0.5 M Na$_2$SO$_4$ solution could lift a 20 g weight without fracture while regular NIPAM hydrogel of the same dimension fractured easily. B) Contraction ratio of the 5P-MA_5P hydrogel toughened in different concentrations of Na$_2$SO$_4$ solution. C) Contraction ratio of PVA/(PVA-MA)-g-PNIPAM hydrogel with different PVA to PVA-MA ratio toughened in 0.3 M Na$_2$SO$_4$ solution. D) The stress – time curve of 5P-MA_5P hydrogel toughened in 0.5 M Na$_2$SO$_4$ solution compared with regular PNIPAM hydrogel. E) Ashby diagram showing the actuation stress vs. modulus of the PVA/(PVA-MA)-g-PNIPAM hydrogel compared with other

hydrogel actuators.

With the combined high toughness and thermal responsiveness, a typical 5P-MA_5P hydrogel strip fabricated via 4D printing and subsequently toughened in 0.5 M Na$_2$SO$_4$ could lift heavy weights (20 g) without large passive deformation or fracture (Figure 5.7A, left). In contrast, conventional NIPAM hydrogel (fabricated by polymerizing 30 wt% NIPAM, 1.5 wt% Bis and 1 wt% Irgacure 2959 in DMSO and immersed back into DI water) with the same dimension deformed severely under the same weight, which lead to formation and propagation of cracks in the hydrogel and eventually fracture of the hydrogel (**Figure 5.7**A, right). We quantitatively measured the contraction force delivered by the two hydrogels, and the tough 5P-MA_5P hydrogel showed ~20 times higher contraction force than the conventional NIPAM hydrogel (**Figure 5.7**D). Compared to various state-of-the-art hydrogel actuators,[52–56] the tough PVA/(PVA-MA)-g-PNIPAM hydrogel showed a relatively high actuation force and modulus (**Figure 5.7**E).
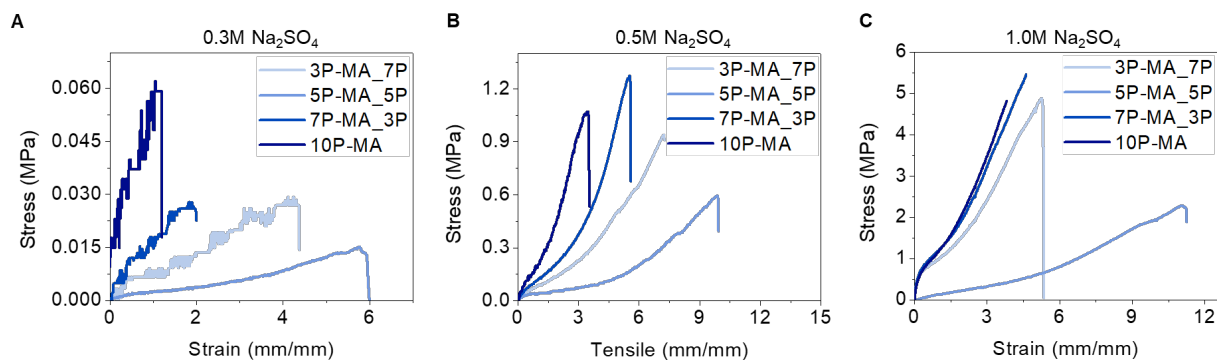
Figure 5.8 Stress-strain curves of PVA/(PVA-MA)-g-PNIPAM hydrogels with different PVA-to-PVA-MA ratios and toughened in different concentrations of Na$_2$SO$_4$ solutions. The 5P-MA_5P

hydrogel toughened in 0.5 M Na$_2$SO$_4$ presented the optimum overall mechanical and responsive performance.
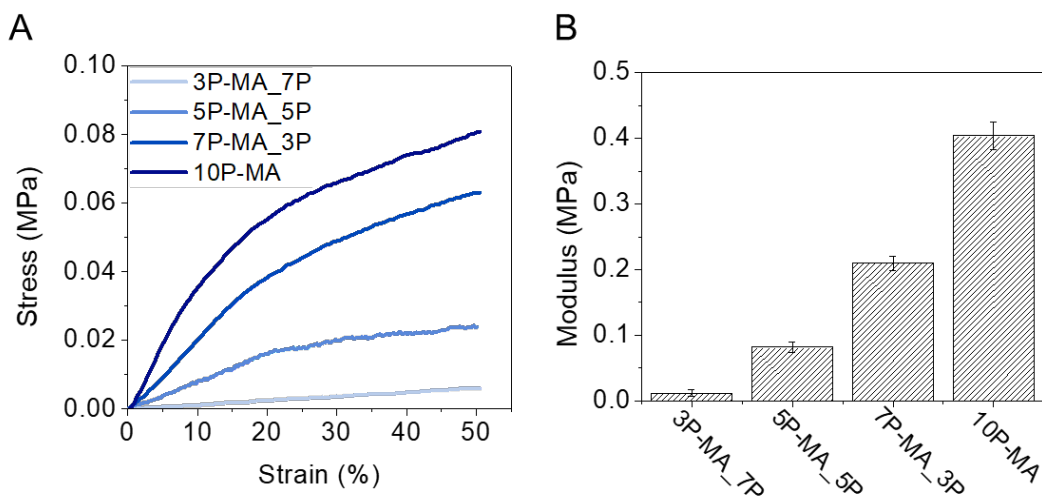
Figure 5.9. A) Stress-strain curves of the as-printed hydrogels with various PVA / PVA-MA ratios in the strain range of 0-50%. B) Corresponding modulus extrapolated from the linear regions of the stress-strain curves in A. According to "Flory rubber elastic theory", during elastic deformation of polymers, the crosslinking density is proportionally correlated with the elastic modulus of the polymer.

The deliverable force of the PVA/(PVA-MA)-g-PNIPAM hydrogel is positively related with the mechanical properties of the hydrogel (**Figure 5.7**E). Without toughening by salting out, the contraction force of the PVA/(PVA-MA)-g-PNIPAM hydrogel is comparable to that of the conventional NIPAM hydrogel. With increasing toughness of the PVA/(PVA-MA)-g-PNIPAM hydrogel by using higher concentration salt solution, the contraction force also increased. The

reason for this relationship is as follows: The non-toughened PVA/(PVA-MA)-g-PNIPAM is intrinsically soft, which would deform severely under low stress. While the hydrogel could contract significantly upon heating when there is no external load, the displacement is reduced when external load exists due to the passive extension of the hydrogel under stress. Thus, the tension between hydrogel and object is relaxed due to this passive deformation which reduced the force being delivered externally (**Figure 5.10**A). Additionally, in the case of high external loading, the hydrogel would immediately fracture due to its low strength and toughness.   On the contrary, the toughened PVA/(PVA-MA)-g-PNIPAM hydrogel has a much higher modulus and would show reduced passive deformation under external loading. The toughened hydrogel could also endure much higher external force. Thus, the tension between toughened hydrogel and external object maintained at a much higher value as the toughened hydrogel contracted without large passive extension under the tension, which led to the increased deliverable force (**Figure 5.10**B).
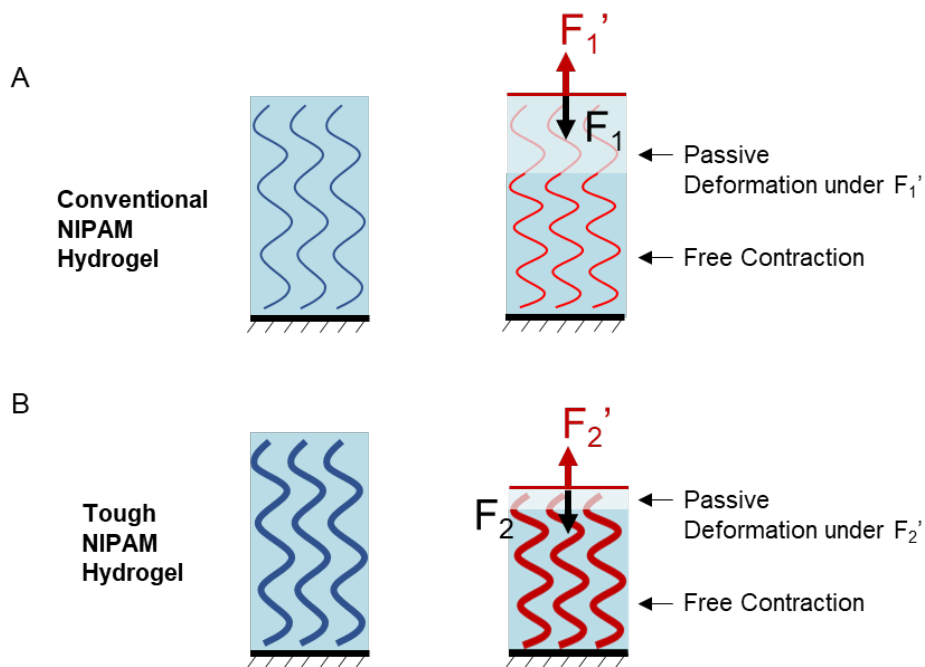
Figure 5.10 Illustration of contraction under constraint of a conventional PNIPAM hydrogel (A) compared with tough PVA/(PVA-MA)-g-PNIPAM hydrogel (B). When the hydrogel contracts to deliver force F to external objects, it also experiences an equivalent counter-force F' from the external object.

5.4.4 Demonstration of actuators with high force and fast actuation

With high toughness and actuation force, the PVA/(PVA-MA)-g-PNIPAM hydrogels could readily be applied to fabricate hydrogel actuators. By 4D printing, bilayer actuators of various geometry could be facilely fabricated. The bilayer actuators consist of a passive layer of PVA/PVA-MA hydrogel and an active layer of PVA/(PVA-MA)-g-PNIPAM hydrogel. The printed bilayer actuators were washed in DI water and immersed in 0.5M Na_2SO_4 salt for toughening. After toughening, the bilayer actuators were immersed back in water for actuation tests.

Figure 5.11A showed the actuation of a bilayer beam by heating. The bilayer beam was initially bent toward the passive layer, due to the higher shrinkage of PVA/PVA-MA hydrogel compared to PVA/(PVA-MA)-g-PNIPAM hydrogel. Upon heating, the bilayer beam quickly bent toward the active layer. Despite the initial reverse bending, the bilayer beam completely bent toward the passive layer within 150 seconds and showed a large bending angle of ~210° at the tip.
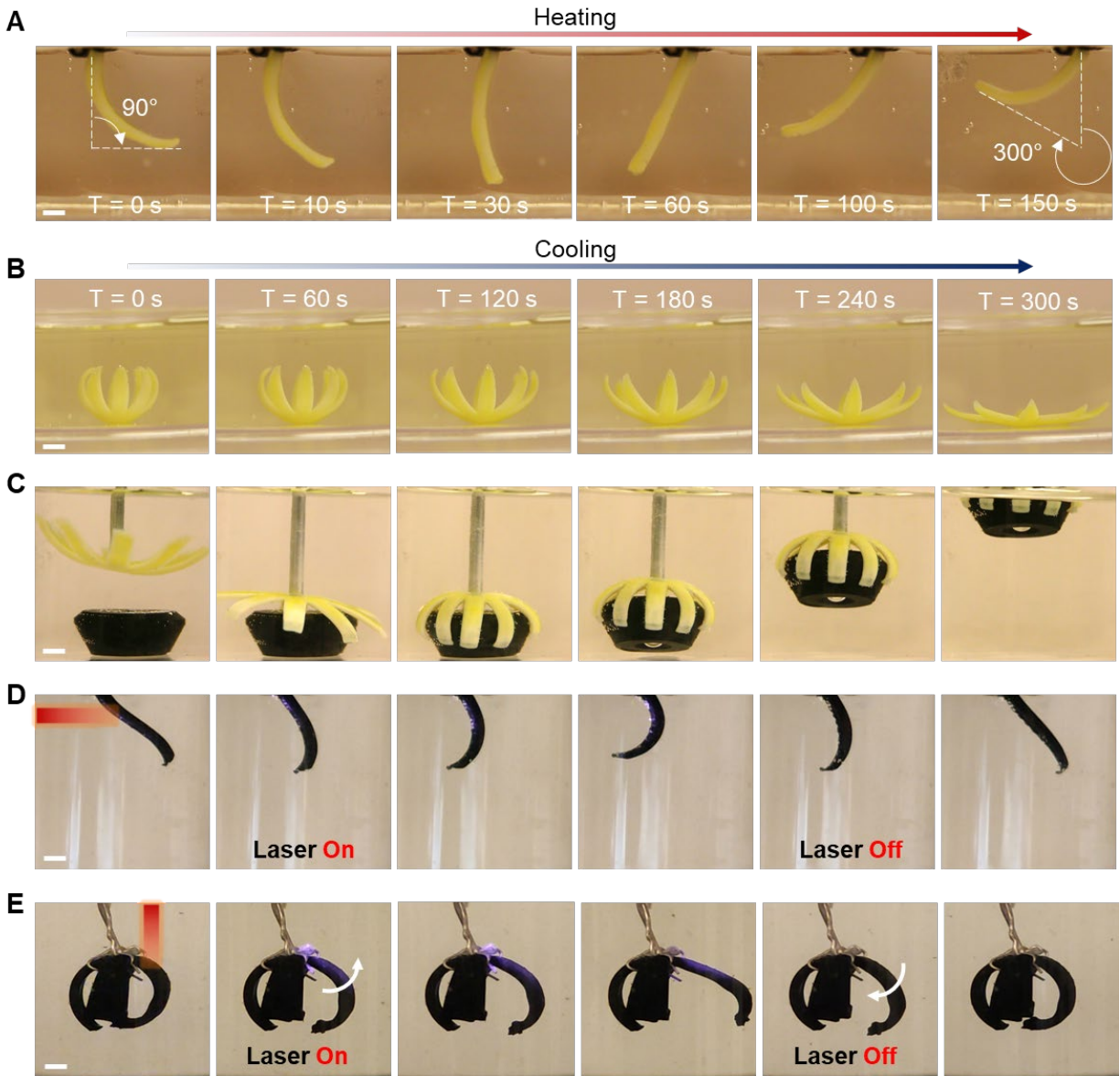
Figure 5.11 Customized actuator geometry and actuation speed. A) A printed bilayer beam actuator showing fast bending and large bending angle under heating. B) A bilayer flower blooms under cooling. C) 3D printed bilayer gripper picking up an object through thermal actuation. The object weighs 1g. D) Remote actuation of bilayer beam actuator coated with a thin layer of poly(pyrrole). E) Remote and selective actuation of bilayer gripper actuator coated with a thin layer of poly(pyrrole). Scale bar: 1 mm.

Figure 5.11B showed the actuation of a bilayer flower by cooling. The flower pedals were initially bent by heating. When immersed in room temperature water bath, the active layer gradually expanded which led to the blooming of the bilayer flower. By spatially programming the area ratio of the passive / active layer, the flower pedals after blooming did not overbend toward the passive layer.

Combining high strength, high toughness, high actuation force and 4D printing aided design, a thermally activated bilayer tough hydrogel gripper was demonstrated (**Figure 5.11**C). Upon heating, the gripper arm bent toward the object and locked onto the object, which enabled the subsequent lifting of the object out of the water bath. In contrast, while a conventional NIPAM hydrogel gripper of the same geometry showed good actuation performance, it deformed severely during the lifting process and failed to lift the same object. Note that the arms of the PVA/(PVA-MA)-g-PNIPAM hydrogel gripper did not show large deformation during the lifting process, owing to the high strength and contraction force of the hydrogel. The weight being lifted weighed 1g, which is approximately 5 times the weight of the solid content of the hydrogel gripper.

Remote activatability is a significant advantage of NIPAM-based hydrogels due to the facile conversion of photons to thermal energy through various photo-absorbers.[4,6] The photo-absorbers are generally black materials with nanometer sizes for maximum photo-thermal

conversion efficiency, here we utilized poly(pyrrole) as the photo-absorber coating. As shown in **Figure 5.11**D & E, the bilayer hydrogel actuator turned black after coating with poly(pyrrole) and gained remote activatability using an IR laser (50 mW). The illuminated part on the hydrogel actuators were locally heated quickly to induce bending, while the unilluminated parts remained cool and static. By controlling the illumination, good spatial control of actuation could be realized in the hydrogel actuator (**Figure 5.11**E).

Actuation speed is another important criterion of hydrogel actuator. Due to the diffusion-mediated swelling and contraction of hydrogels, the actuation speed inversely scales with the actuator size. Utilizing the ability to spatially program the hydrogel, the size-dependent actuation speed of PVA/(PVA-MA)-g-PNIPAM hydrogels could be bypassed by printing large voids into the hydrogel to facilitate the fast diffusion of water in and out of the hydrogel. **Figure 5.12**A showed three types of printed 5P-MA_5P hydrogel lattice, respectively with Kelvin cell, Simple Cubic and Octet truss unit cells. These hydrogel lattices were originally weak and collapsed in air in the as-printed state (**Figure 5.13**A); after toughening in 0.5 M Na_2SO_4, they became capable of self-supporting their own weight and retaining the designed structure in air as a stand-alone architecture (**Figure 5.13**B). When using the lattice design with octet truss cells, the lattice could tolerate high external loading and deformation and still recover (**Figure 5.12**B). Applying the lattice design in printing hydrogel structures, the latticed 5P-MA_5P hydrogel toughened in 0.5 M Na_2SO_4 showed 4 times faster contraction speed compared to a non-structured bulk PVA/(PVA-MA)-g-PNIPAM hydrogel

(**Figure 5.12**C & D). The latticed hydrogel also showed increased contraction ratio compared to its non-structured counterpart. Therefore, with structural design and the aid of 4D printing, fast actuation speed could be achieved in addition to the previously demonstrated high toughness and contraction force.
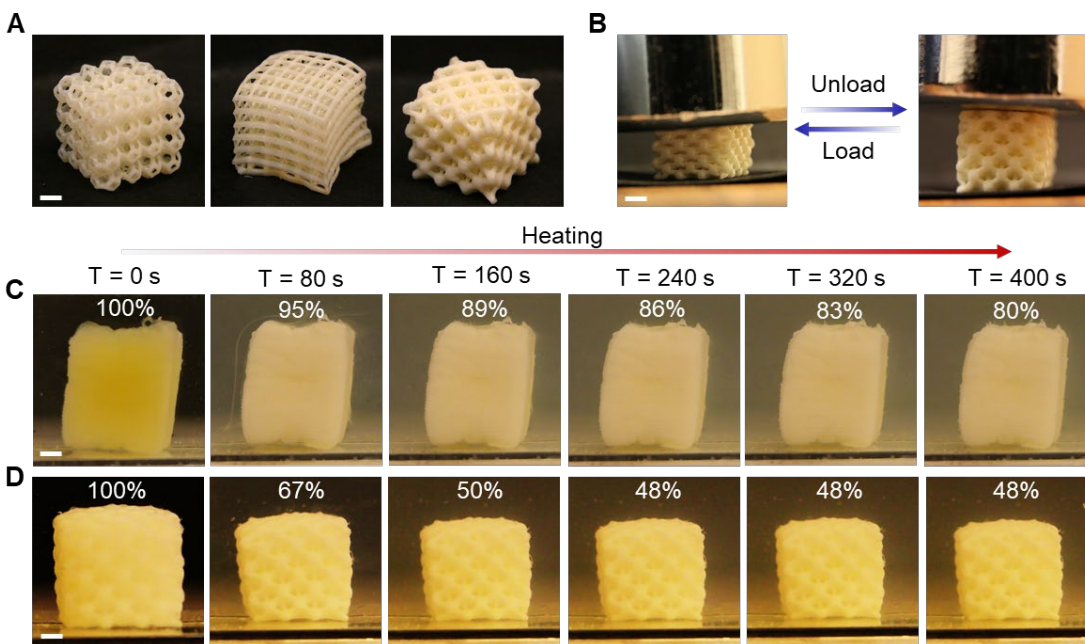

Figure 5.12 A & B) Lattice structured 5P-MA_5P hydrogels toughened in 0.5 M Na_2SO_4 showing self-support in air and recoverability after deformed. C & D) Boosting the actuation speed and contraction ratio by printing lattice structured hydrogel in comparison with a bulk hydrogel of the same bulk volume. Scale bar: 2 mm.
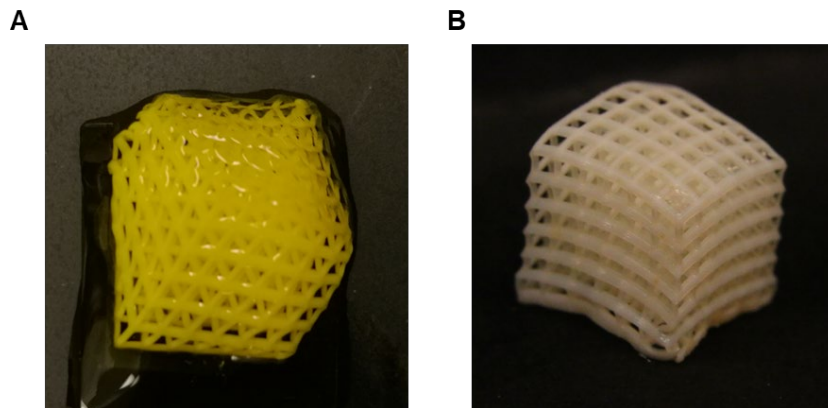
Figure 5.13 Printed simple cubic lattice of PVA/(PVA-MA)-g-PNIPAM hydrogel before (A) and after (B) the toughening treatment by salting-out. These lattices were originally weak and collapsed in air in the as printed state (A) but became capable of self-supporting their own weight and retain the designed structure as a stand-alone architecture in air after toughening in 0.5 M Na_2SO_4 (B).

5.5 Conclusion

In summary, we have demonstrated a material design that consisted of stimuli-responsive monomers and tough polymers in a single hydrogel network for combined high toughness and high actuation performance. Specifically, we showcased this design by grafting thermal responsive NIPAM monomers to tough PVA/PVA-MA hydrogel network in a one pot synthesis. We have evaluated the effect of salt concentration, PVA/PVA-MA ratio and structural design on the mechanical and actuation performance of the PVA/(PVA-MA)-g-PNIPAM hydrogel. Utilizing the combined high toughness and improved actuation force of the PVA/(PVA-MA)-g-PNIPAM hydrogels, bilayer actuators were fabricated via 4D printing for demonstration. Remote actuation using light was also demonstrated using a photo-thermal energy conversion route. Overall, the

presented material design significantly improved material toughness while maintaining high swelling/contraction of the hydrogel. We are convinced that the presented design would benefit the fabrication of hydrogel actuators and robotics for practical applications, and would lay the path for new pH responsive, magneto responsive, humidity responsive hydrogel systems with both high toughness and high actuation performances.

5.6 References

[1]   L. Ionov, *Mater. Today* **2014**, *17*, 494.

[2]   H. Yuk, C. E. Varela, C. S. Nabzdyk, X. Mao, R. F. Padera, E. T. Roche, X. Zhao, *Nature* **2019**, *575*, 169.

[3]   X. Liu, J. Liu, S. Lin, X. Zhao, *Mater. Today* **2020**, *36*, 102.

[4]   Y. Zhao, C. Xuan, X. Qian, Y. Alsaid, M. Hua, L. Jin, X. He, *Sci. Robot.* **2019**, *4*, eaax7112.

[5]   H. Yuk, S. Lin, C. Ma, M. Takaffoli, N. X. Fang, X. Zhao, *Nat. Commun.* **2017**, *8*, 14230.

[6]   X. Qian, Y. Zhao, Y. Alsaid, X. Wang, M. Hua, T. Galy, H. Gopalakrishna, Y. Yang, J. Cui, N. Liu, M. Marszewski, L. Pilon, H. Jiang, X. He, *Nat. Nanotechnol.* **2019**, *14*, 1048.

[7]   X. Xu, Y. Liu, W. Fu, M. Yao, Z. Ding, J. Xuan, D. Li, S. Wang, Y. Xia, M. Cao, *Polymers (Basel).* **2020**, *12*, 1.

[8]   L. D'Eramo, B. Chollet, M. Leman, E. Martwong, M. Li, H. Geisler, J. Dupire, M. Kerdraon, C. Vergne, F. Monti, Y. Tran, P. Tabeling, *Microsystems Nanoeng.* **2018**, *4*,

17069.

[9]   L. Tang, L. Wang, X. Yang, Y. Feng, Y. Li, W. Feng, *Prog. Mater. Sci.* **2021**, *115*, 100702.

[10]   J. Guo, W. Yang, Y. Deng, C. Wang, S. Fu, *Small* **2005**, *1*, 737.

[11]   X. Hu, M. Vatankhah-Varnoosfaderani, J. Zhou, Q. Li, S. S. Sheiko, *Adv. Mater.* **2015**, *27*, 6899.

[12]   J.-Y. Sun, X. Zhao, W. R. K. Illeperuma, O. Chaudhuri, K. H. Oh, D. J. Mooney, J. J. Vlassak, Z. Suo, *Nature* **2012**, *489*, 133.

[13]   X. Zhao, *Soft Matter* **2014**, *10*, 672.

[14]   M. Shibayama, *Soft Matter* **2012**, *8*, 8030.

[15]   M. A. Haq, Y. Su, D. Wang, *Mater. Sci. Eng. C* **2017**, *70*, 842.

[16]   W. R. K. Illeperuma, J. Y. Sun, Z. Suo, J. J. Vlassak, *Soft Matter* **2013**, *9*, 8504.

[17]   K. Depa, A. Strachota, M. Šlouf, J. Hromádková, *Eur. Polym. J.* **2012**, *48*, 1997.

[18]   J. P. Gong, Y. Katsuyama, T. Kurokawa, Y. Osada, *Adv. Mater.* **2003**, *15*, 1155.

[19]   P. Lin, S. Ma, X. Wang, F. Zhou, *Adv. Mater.* **2015**, *27*, 2054.

[20]   Y. Yang, X. Wang, F. Yang, H. Shen, D. Wu, *Adv. Mater.* **2016**, *28*, 7178.

[21]   R. Takahashi, T. L. Sun, Y. Saruwatari, T. Kurokawa, D. R. King, J. P. Gong, *Adv. Mater.* **2018**, *30*, 1.

[22]   S. Lin, C. Cao, Q. Wang, M. Gonzalez, J. E. Dolbow, X. Zhao, *Soft Matter* **2014**, *10*, 7519.

[23]   Y. Huang, D. R. King, T. L. Sun, T. Nonoyama, T. Kurokawa, T. Nakajima, J. P. Gong, *Adv. Funct. Mater.* **2017**, *27*, 1605350.

[24]   C. Xiang, Z. Wang, C. Yang, X. Yao, Y. Wang, Z. Suo, *Mater. Today* **2020**, *34*, 7.

[25]   W. R. K. Illeperuma, J. Y. Sun, Z. Suo, J. J. Vlassak, *Extrem. Mech. Lett.* **2014**, *1*, 90.

[26]   Y. Tian, X. Wei, Z. J. Wang, P. Pan, F. Li, D. Ling, Z. L. Wu, Q. Zheng, *ACS Appl. Mater. Interfaces* **2017**, *9*, 34349.

[27]   S. Y. Zheng, Y. Shen, F. Zhu, J. Yin, J. Qian, J. Fu, Z. L. Wu, Q. Zheng, *Adv. Funct. Mater.* **2018**, *28*, 1.

[28]   X. Peng, Y. Li, Q. Zhang, C. Shang, Q. W. Bai, H. Wang, *Adv. Funct. Mater.* **2016**, *26*, 4491.

[29]   X. Liu, B. He, Z. Wang, H. Tang, T. Su, Q. Wang, *Sci. Rep.* **2014**, *4*, 1.

[30]   S. Xiao, M. Zhang, X. He, L. Huang, Y. Zhang, B. Ren, M. Zhong, Y. Chang, J. Yang, J. Zheng, *ACS Appl. Mater. Interfaces* **2018**, *10*, 21642.

[31]   A. B. Baker, D. F. Wass, R. S. Trask, *Sensors Actuators, B Chem.* **2018**, *254*, 519.

[32]   C. Scherzinger, A. Schwarz, A. Bardow, K. Leonhard, W. Richtering, *Curr. Opin. Colloid Interface Sci.* **2014**, *19*, 84.

[33]   Y. Zhang, S. Furyk, D. E. Bergbreiter, P. S. Cremer, *J. Am. Chem. Soc.* **2005**, *127*, 14505.

[34]   C. Yang, Z. Liu, C. Chen, K. Shi, L. Zhang, X. J. Ju, W. Wang, R. Xie, L. Y. Chu, *ACS Appl. Mater. Interfaces* **2017**, *9*, 15758.

[35]   Y. Li, Y. Sun, Y. Xiao, G. Gao, S. Liu, J. Zhang, J. Fu, *ACS Appl. Mater. Interfaces* **2016**,

8, 26326.

[36] A. H. Gelebart, G. Vantomme, E. W. Meijer, D. J. Broer, *Adv. Mater.* **2017**, *29*, 1606712.

[37] D. Jan Mulder, R. L. B. Selinger, A. Konya, A. H. Gelebart, M. Varga, G. Vantomme, E. W. Meijer, D. J. Broer, *Nature* **2017**, *546*, 632.

[38] M. Ma, L. Guo, D. G. Anderson, R. Langer, *Science (80-.).* **2013**, *339*, 186.

[39] G. J. Lake, A. G. Thomas, *Proc. R. Soc. London. Ser. A. Math. Phys. Sci.* **1967**, *300*, 108.

[40] S. Lin, J. Liu, X. Liu, X. Zhao, *Proc. Natl. Acad. Sci. U. S. A.* **2019**, *116*, 10244.

[41] S. Lin, X. Liu, J. Liu, H. Yuk, H.-C. Loh, G. A. Parada, C. Settens, J. Song, A. Masic, G. H. McKinley, X. Zhao, *Sci. Adv.* **2019**, *5*, eaau8528.

[42] D. Wu, J. Song, Z. Zhai, M. Hua, C. Kim, I. Frenkel, H. Jiang, X. He, *ACS Appl. Mater. Interfaces* **2019**, *11*, 47468.

[43] N. A. Peppas, E. W. Merrill, *J. Appl. Polym. Sci.* **1976**, *20*, 1457.

[44] R. Bai, J. Yang, X. P. Morelle, Z. Suo, *Macromol. Rapid Commun.* **2019**, *40*, 1.

[45] W. Kunz, J. Henle, B. W. Ninham, *Curr. Opin. Colloid Interface Sci.* **2004**, *9*, 19.

[46] Q. He, Y. Huang, S. Wang, *Adv. Funct. Mater.* **2018**, *28*, 1.

[47] T. Wang, J. Huang, Y. Yang, E. Zhang, W. Sun, Z. Tong, *ACS Appl. Mater. Interfaces* **2015**, *7*, 23423.

[48] W. J. Zheng, N. An, J. H. Yang, J. Zhou, Y. M. Chen, *ACS Appl. Mater. Interfaces* **2015**, *7*, 1758.

[49] Y. J. Wang, C. Y. Li, Z. J. Wang, Y. Zhao, L. Chen, Z. L. Wu, Q. Zheng, *J. Polym. Sci.*

Part B Polym. Phys. **2018**, *56*, 1281.

[50] H. Jiang, W. Su, P. T. Mather, T. J. Bunning, *Polymer (Guildf).* **1999**, *40*, 4593.

[51] P. J. Flory, *Polym. J.* **1985**, *17*, 1.

[52] C. Cvetkovic, R. Raman, V. Chan, B. J. Williams, M. Tolish, P. Bajaj, M. S. Sakar, H. H. Asada, M. T. A. Saif, R. Bashir, *Proc. Natl. Acad. Sci. U. S. A.* **2014**, *111*, 10125.

[53] L. W. Xia, R. Xie, X. J. Ju, W. Wang, Q. Chen, L. Y. Chu, *Nat. Commun.* **2013**, *4*, 1.

[54] Y. S. Kim, M. Liu, Y. Ishida, Y. Ebina, M. Osada, T. Sasaki, T. Hikima, M. Takata, T. Aida, *Nat. Mater.* **2015**, *14*, 1002.

[55] Y. Takashima, S. Hatanaka, M. Otsubo, M. Nakahata, T. Kakuta, A. Hashidzume, H. Yamaguchi, A. Harada, *Nat. Commun.* **2012**, *3*, 1270.

[56] E. Palleau, D. Morales, M. D. Dickey, O. D. Velev, *Nat. Commun.* **2013**, *4*, 1.

Chapter 6 Conclusion and Outlook

6.1 Conclusion

Hydrogels are promising materials for a myriad of applications due to their desirable physical and chemical properties such as high diffusivity, low friction, high water content and good biocompatibility. These application of hydrogel materials are often hindered due to the weak mechanical properties of hydrogels due to their low solid content. Therefore, exploring effective methods for boosting the robustness of hydrogels while maintaining or even promoting their desirable attributes will bring impactful advances for the development of hydrogel materials.

In Chapter 2, we introduced an effective method for tuning aggregation state of polymers, known as the "salting out" method. Based on the understanding of the fracture mechanics, hydrogels with aggregated network can sustain much higher loading compared with its disseminated counterparts. Combined with freezing which help to fixate the shape of the polymer precursor, hydrogels with tunable mechanical properties and pore structures were achieved. The study elucidated the interaction between polymer, water, and ions, which laid foundation for developing hydrogels with high strength, toughness, and fatigue resistance.

In Chapter 3, adopting the design inspirations from natural loading bearing materials, we aimed to create anisotropic hydrogels based on the freezing assisted salting out method. We replaced

uniform freezing with directional freezing and obtained hierarchically aligned hydrogels that show micro alignments due to the directional ice templating, and nano alignment due to the salting out on pre-aligned microstructures. The fabricated hydrogel showed record breaking strength, toughness and fatigue threshold compared to reported tough hydrogels.

In Chapter 4, we explored the application of the freezing assisted salting out method for fabricating polymer coatings with high toughness on fragile material networks. Open porous structured materials have significant benefit for energy storage applications but are often fragile. By applying a thin coating of the development PVA tough hydrogels using a modified freezing assisted salting out method, the original open-porous material was reinforced while maintaining its original electrochemical properties. With the reinforcement coating, the electrochemical and mechanical stability was significantly improved.

In Chapter 5, we explored the 3D printing adaptation of the freezing assisted salting out method. 3D printing brings significant advantage for fabricating hydrogels with arbitrary and complex geometries. To enable the photopolymerization of the developed PVA hydrogel, chemical modification was carried out. Blending the modified PVA macromonomer and stimuli responsive monomers, thermal actuation of tough hydrogel was realized, and showed improved actuation performance.

6.2 Outlook

The presented method in this dissertation for constructing tough hydrogels hold further applications in advanced fields like soft robot and biomedical fields, which require combination of high mechanical toughness, tunability and complex shapes.

For underwater hydrogel robots' applications, unlike real creatures, today's mainstream robots are rigid and fails to conform to the object they interact with, whereas soft robots could perform the same task with minimal invasion and damage to the object. Hydrogel soft robots are especially advantageous for underwater operations to do their water rich composition which endows them with infrared and acoustic camouflage abilities. Hydrogel robots are often actuated hydraulically with designs of hollow interiors and thin walls, which has presented challenges for fabrication techniques and mechanical robustness. My current studies provide a solid basis for simultaneously resolving the issues, with improvements to be made on further increasing the fatigue resistance of the printed hydrogel. I plan to further improve the fatigue resistance by printing aligned structure in each layer of the hydrogel via grayscale patterning techniques or compositing.

For biomimetic hydrogel organoids applications, hydrogels are widely used as scaffolds for cell culturing and tissue engineering. However, they are often used as temporary scaffolds and are incapable of being used alongside the grown cells and tissues due to the lack of high mechanical robustness. While in the studies of organs with naturally complex structures, like pulmonary

disease modeling, current hydrogels lacked biomimetic structures with high complexity and high resolution.

My current studies provide a solid basis for separately resolving the issues, with improvements to be made on further increasing the resolution of the printed hydrogel. While the materials that I have currently developed are biocompatible, the biocompatibility and cell adherence could be further improved by grafting dopamine or gelatin molecules to the hydrogel via chemical modification. I plan to further improve the resolution by applying a shrink printing technique or upgrading the resolution of the 3D printer.

In summary, harnessing the design-structure-property developmental pathway, the presented strategies in this dissertation could realize the fabrication of high resolution, highly complex, highly robust, and multifunctional hydrogels.